Differential Cross Section for Neutron-Proton Radiative Capture at $E_n = 63.4$ MeV

by

Muhammad Saalih Allie

Thesis presented for the degree of
Doctor of Philosophy
in the Department of Physics
Faculty of Science
University of Cape Town

October 1996

Abstract

The angular distribution of photons from n-p radiative capture of 63.4 MeV neutrons has been measured using a new technique in which both the photon and the deuteron were detected simultaneously and the deuteron identified using pulse shape discrimination. Data taken at eight n–γ angles (45°–150°) were transformed to deuteron photodisintegration cross sections at the equivalent laboratory energy, $E_\gamma = 33.9$ MeV. The data were analysed in combination with independent measurements of the 0° and 180° cross sections. Legendre polynomial coefficients obtained from the analysis are consistent with other measurements in this energy range as well as with values reported from global fits. The measurements deviate marginally from predictions based on potential model calculations using the Bonn r-space and Paris potentials.

Acknowledgements

I take the opportunity to record my appreciation and gratitude to:

Professor Frank Brooks who supervised this work, for his tireless assistance, insights and guidance throughout the duration of the project.

Sincere thanks are expressed to the following collaborators and friends for their contributions to the project and for their encouragement:

Andy Buffler, David Aschman, Krish Bharuth-Ram, Willem Cilliers, Roger Fearick, (the late) Colin Henderson, Roy McMurray, Hank Miller, Rudolph Nchodu, Richard Newman, Marian Oliver, Sandy Perez, Bruce Simpson, Ricky Smit, Douw Steyn, and Ieks van Heerden.

My thanks also go to the following staff for their ever-ready assistance:

The staff of the NAC, the staff of the UCT Physics workshop, Fiona Gibbons and Joan Parsons.

I also wish to thank:

Professor H. Arenhövel for providing results from theoretical calculations; and Dr. A. Zucchiatti for help in using the Monte Carlo code.

Finally, I pay tribute to my late mother, my father and my sister for their encouragement and support of my studies.

Contents

List of Figures

List of Tables

Chapter 1

Introduction

1.1 The deuteron

Since its discovery in 1932 the deuteron [Ur32] has played a central role in attempts to understand the nature of the force that binds nuclear matter together. As the simplest bound nuclear system the deuteron provides a unique laboratory for developing and testing models of the nucleon-nucleon (NN) force. Our current understanding of the NN force is based primarily on models that invoke meson exchange processes, as first suggested by Yukawa in 1934. At the level of the quark description of nucleons, the nuclear force may be considered to arise as a result of an exchange of quark-antiquark ($q\bar{q}$) pairs. Figure 1-1, taken from ref. [Po95], shows Feynman-type diagrams depicting these two equivalent representations of the NN force.

As yet, there is no consistent theory of the nuclear force based on quark and gluon interactions, and the phenomenological meson exchange models still provide the most successful quantitative description of the NN force [Po95][Wo90]. Examples of such models are the Paris [La80] and Bonn [Ma87] potentials. Based on these descriptions, the NN force may be divided into three interaction regions defined by the distance r between the nucleons [Fr89]. Figure 1-2 shows a schematic diagram indicating the three regions viz., the long range part ($r > 2$ fm), the medium range part ($r \sim 1$ fm), and the short range part ($r < 0.6$ fm) which also includes a "hard core". The long range attraction is described by the exchange of single pseudoscalar pions ($J^\pi = 0^-$),

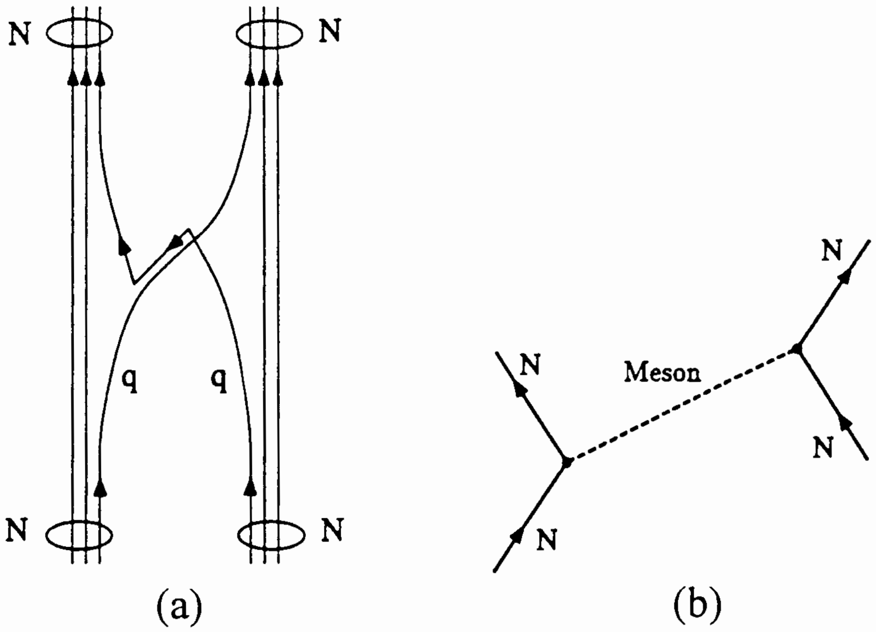

Figure 1-1: *Representation of (a) quark exchange between nucleons of a quark-antiquark pair with the antiquark depicted as a quark moving backwards in time and (b) meson exchange between nucleons. Figure from [Po95].*

while the intermediate range, and most attractive part of the force, is described mainly by two-pion (2π) exchange. The short range part of the force is strongly repulsive and comes about due to three-pion (3π) and other multi-pion exchanges as well as heavy vector mesons ($J^\pi = 1^-$). However, part of this repulsive region comprises a"hard core" attributed to QCD effects which have not been defined explicitly. The hard core is therefore put in "by hand"[Wo90]. A one boson exchange (OBE) approximation is often used in constructing the NN potential, and in this approach the 2π exchange is represented by single $\sigma(0^+)$ and $\rho(1^-)$ exchanges, while the 3π is simulated by $\omega(1^-)$ exchange [Fr89]. The Nijmegen potential [Na78], for example, is a pure OBE potential while the Bonn potential relies partly on this approach [Ma88]. The Paris potential, however, is constructed from dispersion relations in which all the 2π and 3π exchanges are taken into account explicitly [Ma88].

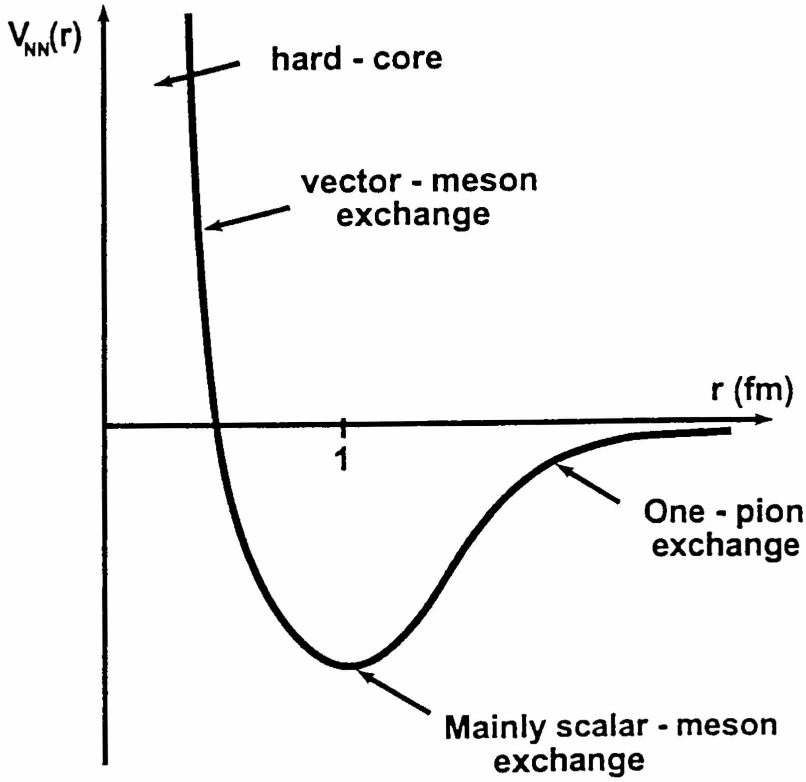

Figure 1-2: *Schematic representation of the nucleon-nucleon potential showing different regions of interaction as a function of distance r between the two nucleons. Figure adapted from refs. [Wo90] and [La90].*

1.2 Photodisintegration and n-p capture

Photodisintegration of the deuteron, and its inverse neutron-proton capture, provide ways of studying the interior part of the two-body wave function [Ar91]. In particular, these processes are highly sensitive to many-body effects [La84]. For example, for photodisintegration of the deuteron at photon energies of 100 MeV, the one-body processes account for only about one-third of the cross section [Ca87]. It is also interesting to note that the first clear signal of the presence of meson exchange currents in nuclei was demonstrated in the capture of thermal neutrons by protons [Ri72]. In general, therefore, photodisintegration of the deuteron and n-p capture provide important tools to complement other sources of information about the NN force such as NN scattering and the static properties of the deuteron. With regard to deuteron photodisintegration, neutron-proton capture and electrodisintegration, ref. [Ar91] expresses it thus, " ...the comparison between theory and experiment is an important and direct test for the underlying theoretical framework and any significant discrepancy will point to shortcomings of the theoretical description...". In the present work the differential cross section for neutron-proton capture is measured, and the results compared with potential model calculations.

Photodisintegration was first described in 1934 by Chadwick and Goldhaber [Ch34]. Their paper entitled "*A nuclear photo-effect: Disintegration of the diplon by gamma-rays*" described experiments in which they used 2.62 MeV gamma rays from thorium to irradiate an ionisation chamber filled with 'heavy hydrogen' in order to achieve the reaction $\gamma + d \rightarrow n + p$. The first theoretical paper, "*Quantum Theory of the Diplon*" appeared in 1935 by Bethe and Peierls [Be35] in which they calculated $\sigma_{ph}(E_\gamma)$ the photodisintegration cross section of the deuteron as a function of E_γ, the photon energy. The cross section, calculated for electric dipole transitions only, and assuming the deuteron to be in a pure $^3S_1$ state, was given thus as

$$\sigma_{ph}(E_\gamma) = \frac{8\pi}{3}\frac{e^2}{\hbar c\alpha^2}\frac{(E_\gamma/E_b - 1)^{\frac{3}{2}}}{(E_\gamma/E_b)^3} \qquad (1.1)$$

where e is the elementary charge, c is the velocity of light, $\hbar$ is Planck's constant h

divided by 2π, ν is the frequency of the radiation, E_b is the deuteron binding energy, and α is given by $\sqrt{ME_b}/\hbar$ where M is the average nucleon mass. Equation 1.1 is also known as the Bethe-Peierls cross section. With regard to the differential cross section, the approach described above, yields an expression for the differential cross section for photodisintegration which varies as $\sin^2\theta$ where θ is the centre-of-mass angle between the incoming photon and the outgoing photoproton [Ar91]. This behavior follows as a consequence of considering only electric dipole transitions together with the assumption that the deuteron is in a pure, spherically symmetric S - state.

In 1936 Amaldi and Fermi [Am36] measured the capture cross section of thermal neutrons by hydrogen and found the cross section to be two orders of magnitude larger than that predicted by the Bethe-Peierls cross section. Fermi [Fe35] was able to account for this by considering the spin dependence of the forces i.e. the reaction can proceed by a magnetic dipole transition which involves the virtual singlet state in the continuum and the real bound state, namely, ${}^1S_{(continuum)} \rightarrow {}^3S_{(bound)}$. The cross section for photodisintegration therefore comprises not only the Bethe-Peierls cross section for E1 transitions but also a part due to M1 magnetic transitions as shown in figure 1-3.

More than sixty years have passed since the initial activity with regard to deuteron photodisintegration and a large amount of experimental and theoretical work has been produced during this period. The level of this activity may be gathered from figure 1-4 which is reproduced from the 1991 review monograph by Arenhövel and Sanzone [Ar91]. The majority of measurements shown in figure 1-4 are based on experiments using radioactive sources (low energies) and continuous bremsstrahlung beams [Ar91]. Over the past twenty years however, a number of new techniques have supplanted bremsstrahlung experiments. These include tagged photons [De92][Kr92], laser backscattering [De85][Be86] and in-flight positron annihilation [De86][Le89]. In comparison with the number of photodisintegration experiments relatively few neutron capture experiments have been reported, as may be seen by comparing tables 1.2 and 1.3, for example.

The early theories of photodisintegration are characterised by the use of simple wavefunctions and forces in which only E1 and M1 transitions are considered [Sq52]. By the end of the 1950's calculations were being made in which potentials based on

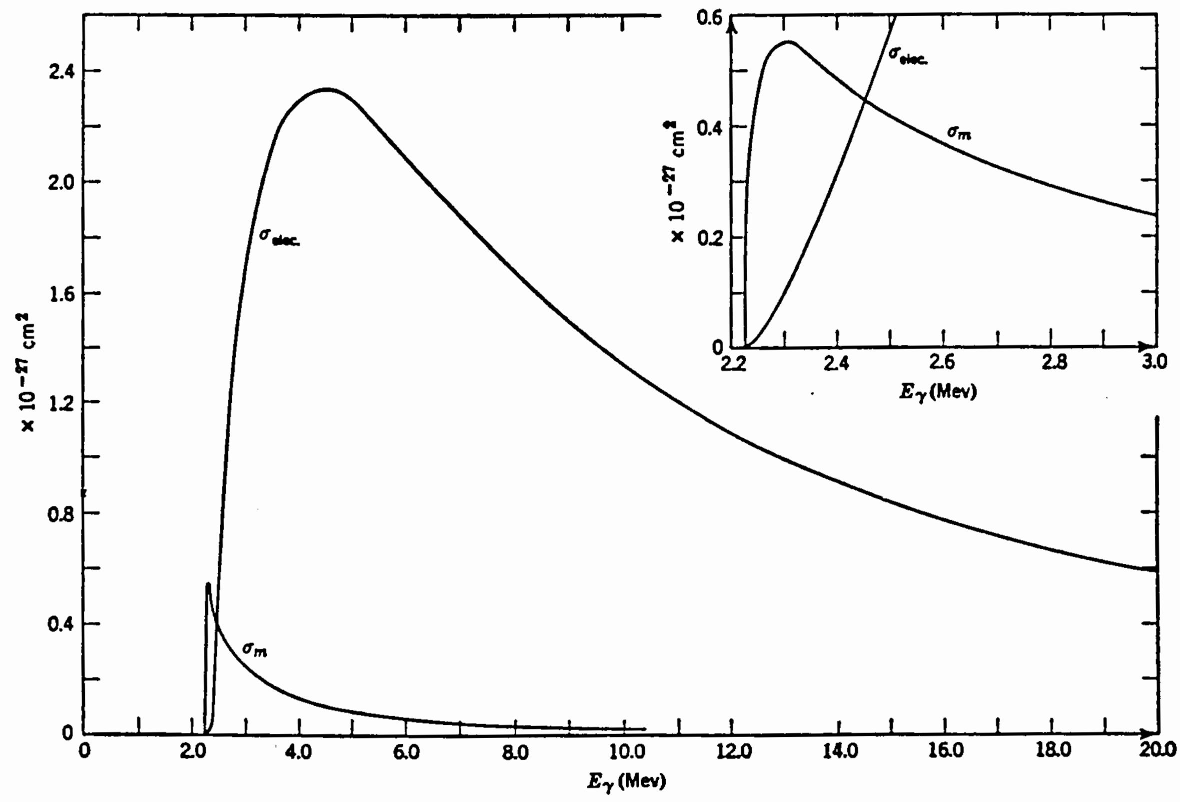

Figure 1-3: *Photoelectric (E1 only) and photomagnetic (M1 only) cross sections as a function of photon energy. The inset shows the region near threshold magnified several times. Figure from [Be56].*

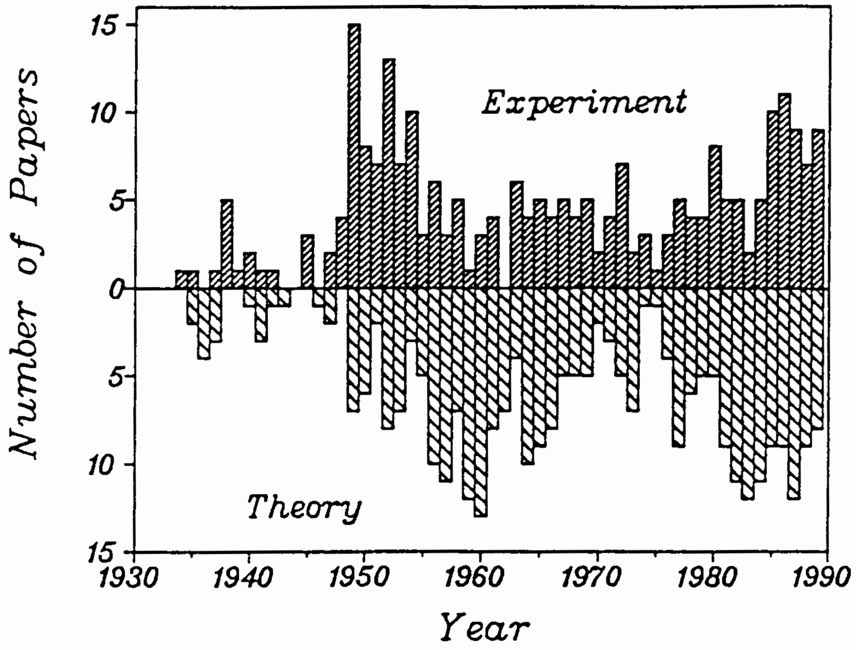

Figure 1-4: *Histogram of experimental and theoretical papers per year on deuteron photodisintegration from 1934 to 1991. Figure from [Ar91].*

meson exchange were being used [De58][De59a][De59b] and higher order multipoles were included [Ru60]. An often cited paper on deuteron photodisintegration below the pion production threshold, is that of Partovi [Pa64], which is based on classical non-relativistic theory. In this paper the Hamada-Johnston potential [Ha62] is used and multipoles up to the octupole are considered. Since then, there have a been a number of developments, particularly with regard to the inclusion of subnuclear degrees of freedom and relativistic effects. In 1972 Riska and Brown [Ri72], using the approach of Villars [Vi47], were able to explain a long standing 10% difference between theoretical predictions and measurements of the thermal neutron capture cross section by invoking meson exchange currents explicitly. This was followed by several attempts at incorporating the subnuclear degrees of freedom in the form of meson exchange currents (MEC) [Ha73] and isobar configurations (IC) [Mi73] in order to describe the results of measurements more accurately. In 1982 Cambi et al. [Ca82a] showed the importance of including relativistic effects in photodisintegration calculations even at low energies. A more detailed account of MEC, IC and RC effects is given in chapter 2.

A range of phenomenological potentials based on the exchange of mesons, in particular the Paris potential [Co73][La80] and the Bonn [Ho81][Ma87] potential, have provided the basis for predictions of the photodisintegration observables. Recently, though, there has been interest in quark-gluon degrees of freedom [De90][Vi91][Bu95] which has lead to a closer scrutiny of the theory which is based on nuclear and meson degrees of freedom only. One area of focus is the low energy regime where it is presumed that these degrees of freedom should be sufficient to describe the electromagnetic breakup of the deuteron. In particular, at energies below 40 MeV uncertainties in the procedures for incorporating relativistic corrections and isobar configurations are felt to be well understood [Sc91], while gauge independence of the non-relativistic calculations is fulfilled to a very high degree. These conditions dictate that the "theoretical results are almost uniquely fixed once the NN potential is given" [Sc91]. However, a number of problems have emerged which could be indicative of a more fundamental deficiency in the theory. A brief comparison of theory and experiment with regard to cross section observables is presented below. Unless otherwise stated, the theoretical calculations referred to are potential model calculations which include meson exchange currents, isobar configurations and relativistic corrections.

1.3 The total photodisintegration cross section

Table 1.1, adapted from ref. [Ja93b], summarises the experimental measurements of σ_T, the total photodisintegration cross section, for photon energies $E_\gamma^{lab} < 75$ MeV. Figure 1-5(a) is a plot of the data in the table while figure 1-5(b) shows the ratio of measurement to the theoretical predictions of Jaus et al. [Ja93b] based on the Bonn r-space potential. From the figure, it can be seen that the results of these calculations are consistent with most of the data over the energy range from threshold to 40 MeV. However, there are suggestions of systematic deviations between experiment and theory, for example between 10 and 30 MeV or between 60 and 70 MeV.

In the energy range up to 40 MeV Schmitt et al. [Sc91] have used a "goodness-of-fit" test as a measure of how well the trend of the data, as a function of photon energy, is modelled by the potential model calculations based on the Paris potential and on the various OBE approximations to the full Bonn potential[1]. Their results indicate that the calculations based on the Paris and the Bonn OBE-T potential are incompatible with the experimentally measured cross sections while the results using the Bonn OBE-Q and r-space potentials are inconclusive.

1.4 The differential cross section

1.4.1 The differential cross section at 0° and 180°

The measurements of the differential cross section at 0° by the Mainz group in 1976 [Hu76] stimulated renewed interest in photodisintegration as a source of information about the NN interaction. The discrepancy between these measurements and the predictions based on potential model calculations lead to intensive activity by both theorists and experimentalists [Gi81][Zi86][Du85][De91a][Me85]. One of the interesting results to emerge was the fact that relativistic corrections, mainly associated with the spin-orbit term, are important even at energies as low as $E_\gamma = 20$ MeV [Ca82a][Fr84]. The incorporation of this effect into the calculations reduced the discrepancy between theory and experiment by between 20 and 30 percent as seen by comparing figures 1-6(a) and 1-6(b) which show the effect of calculations (a) without and (b) with the relativistic spin-orbit dipole operator included in the calculation [Fr84]. The figures are reproduced from ref. [Ar91].

A series of accurate measurements of the differential cross section between 20 and 100 MeV were made by the Gent-Mainz collaboration in 1992 [Zi92a]. These results differed by about 9% from the previous set of Hughes et al. [Hu76], and improved the agreement between the theoretical predictions and experiment. Figure 1-7, shows the experimental data for the differential cross section at 0° as a function of energy. One of the significant features, confirming earlier measurements [Zi86][De91b], is the dip in

---

[1] A number of one boson exchange (OBE) parametrisations of the full momentum space Bonn potential are used when performing the calculations e.g. the relativistic (OBE-Q), the energy dependent (OBE-T) and the non-relativistic coordinate space (OBE-R). The latter is often referred to as the Bonn r-space or Bonn CS potential.

Table 1.1: *Measurements of the total photodisintegration cross section at various photon energies compared with potential model calculations using the Bonn r-space potential [Ja93b]. The Table is adapted from ref. [Ja93b].*

E_γ^{lab} (MeV)	Ref.	σ_T (expt)	σ_T (theory)
2.754	[Mo89]	1456 (45)	1484
5.97	[Bi85]	2162 (99)	2211
7.25	[Bi85]	1882 (11)	1902
7.60	[Bi85]	1803 (16)	1824
7.64	[Bi85]	1810 (28)	1816
8.80	[Bi85]	1586 (11)	1585
9.00	[Bi85]	1570 (36)	1549
11.39	[Bi85]	1257 (36)	1191
14.70	[Be86]	925 (20)	873
14.76	[St85]	970 (55)	868
15.00	[Ah74]	867 (27)	851
15.03	[Mi89]	870 (26)	849
19.3	[Be86]	617 (9)	610
20.0	[Ah74]	585 (14)	581
20.8	[Bo79]	582 (44)	551
21.5	[Wa90]	550.3 (10.5)	526.6
23.4	[Bo79]	511 (35)	469
25.0	[Ah74]	428 (17)	427
25.9	[Ah74]	385 (16)	407
28.5	[Bo79]	367 (19)	356
28.9	[Be86]	361 (6)	349
31.0	[Bo79]	306 (21)	316
32.6	[Wa90]	307.0 (3.7)	294.2
33.5	[Bo79]	264 (20)	283
38.6	[Bo79]	234 (18)	232
40.3	[Wa90]	215.8 (2.6)	218.5
47.5	[Be86]	177 (3)	174
57.5	[Be86]	139 (3)	135
64.0	[De92]	122.3 (1.8)	117.9
65.8	[De92]	117.7 (1.8)	114.0
67.8	[De92]	112.5 (1.3)	110.1
70.0	[De92]	106.2 (1.6)	106.1
74.0	[Be86]	97.6 (5.3)	99.6

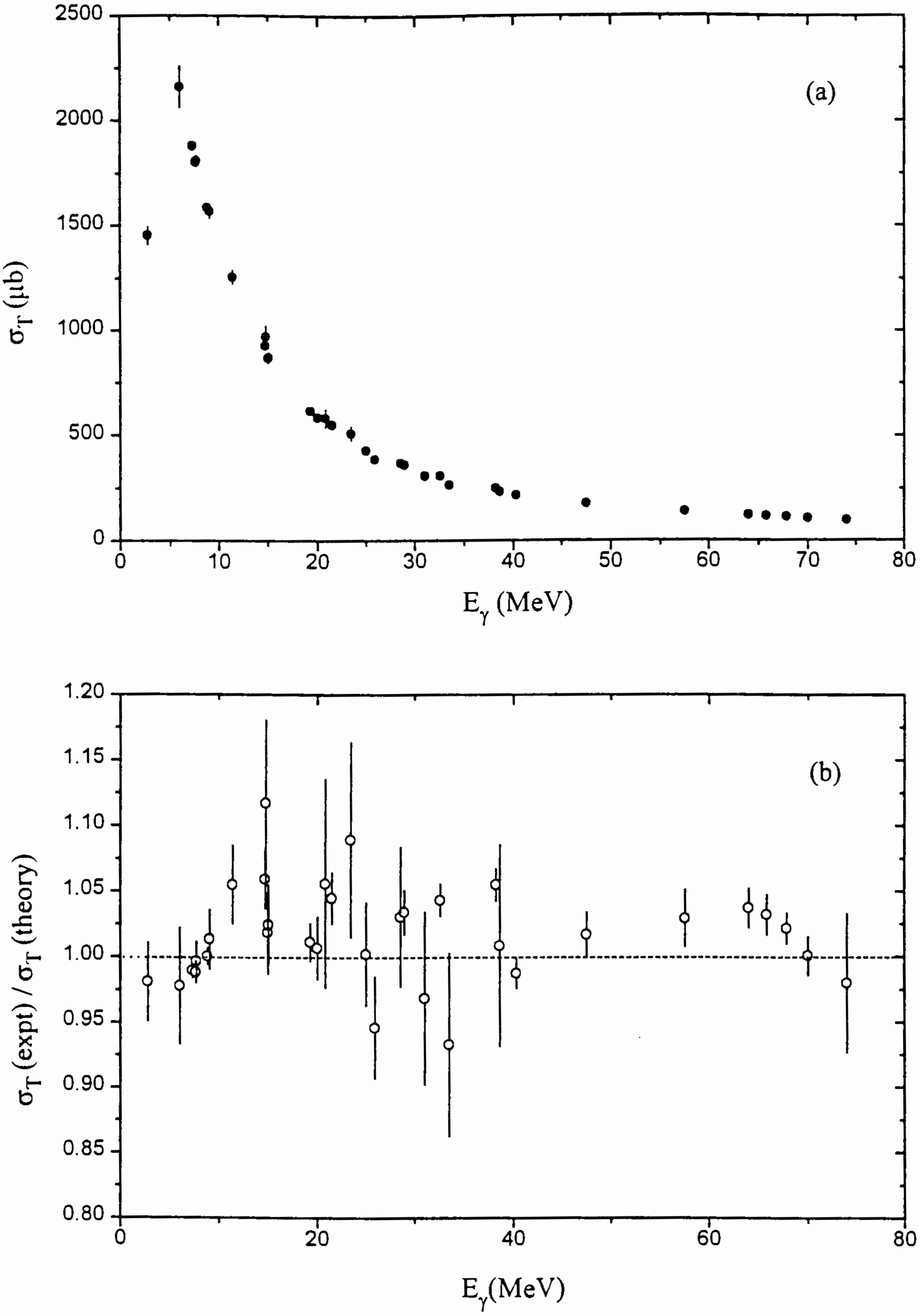

Figure 1-5: *(a) Measurements of the total photodisintegration cross section σ_T (expt) for photon energies up to 75 MeV; and (b) the ratio of σ_T (expt) to σ_T (theory), calculated by Jaus et el. [Ja93b] using the Bonn r-space potential. The data are from Table 1.1, adapted from [Ja93b].*

the cross section around 10 MeV. The figure also shows the results of potential model calculations based on different potentials.

From "goodness-of-fit" tests, Zieger et al. concluded that the calculations of Jaus and Woolcock, in which a modified form of the Paris potential [Ja87a][Ja87b] was used, best fitted the trend of the measurements in figure 1-7. In the approach of Jaus and Woolcock the Paris potential was modified by parametrising $f_{\pi NN}$ the πNN coupling constant and account was taken of the difference between the $\pi^{\pm}$ and π^{0} masses [Ja84]. As pointed out by Zieger et al. [Zi92a], it is interesting to note that there is a systematic difference of about 7% between the experimental results and the calculations based on the *unmodified* Paris potential as calculated by Arenhövel et al. [Ar91]. With regard to the Bonn OBE-Q potential, calculations based on this model [Ar91] do not render the appropriate shape of the excitation function. More recently though, Jaus et al. [Ja93a] have indicated that within their revised "modified current conservation" formalism they are unable to fit the data of Zieger et al. using the modified Paris potential, and that only results with the Bonn r-space potential describe the data [Ja93b] successfully. However, the dip in the cross section at 10 MeV is not correctly predicted by the theory. There are also problems with the use of the Bonn r-space potential at higher energies in that the calculations predict values higher than the experimental results up to 143 MeV and lower values thereafter, and a minimum that occurs at about 150 MeV is also not predicted.

Prior to 1992 few measurements of the differential cross section at 180° were reported. Since then Zieger et al. [Zi92b] have measured this cross section as a function of photon energy, as shown in figure 1-8. The predictions from various theoretical models are also indicated. As with the differential cross section at 0° the calculations with the modified Paris potential used by Jaus and Woolcock [Ja87a][Ja87b] are reported to agree best with experiment [Zi92b]. However, in contrast to the situation at 0°, the calculations using the Bonn-Q potential used by Arenhövel were also found to be in agreement with the experimental trend [Zi92b].

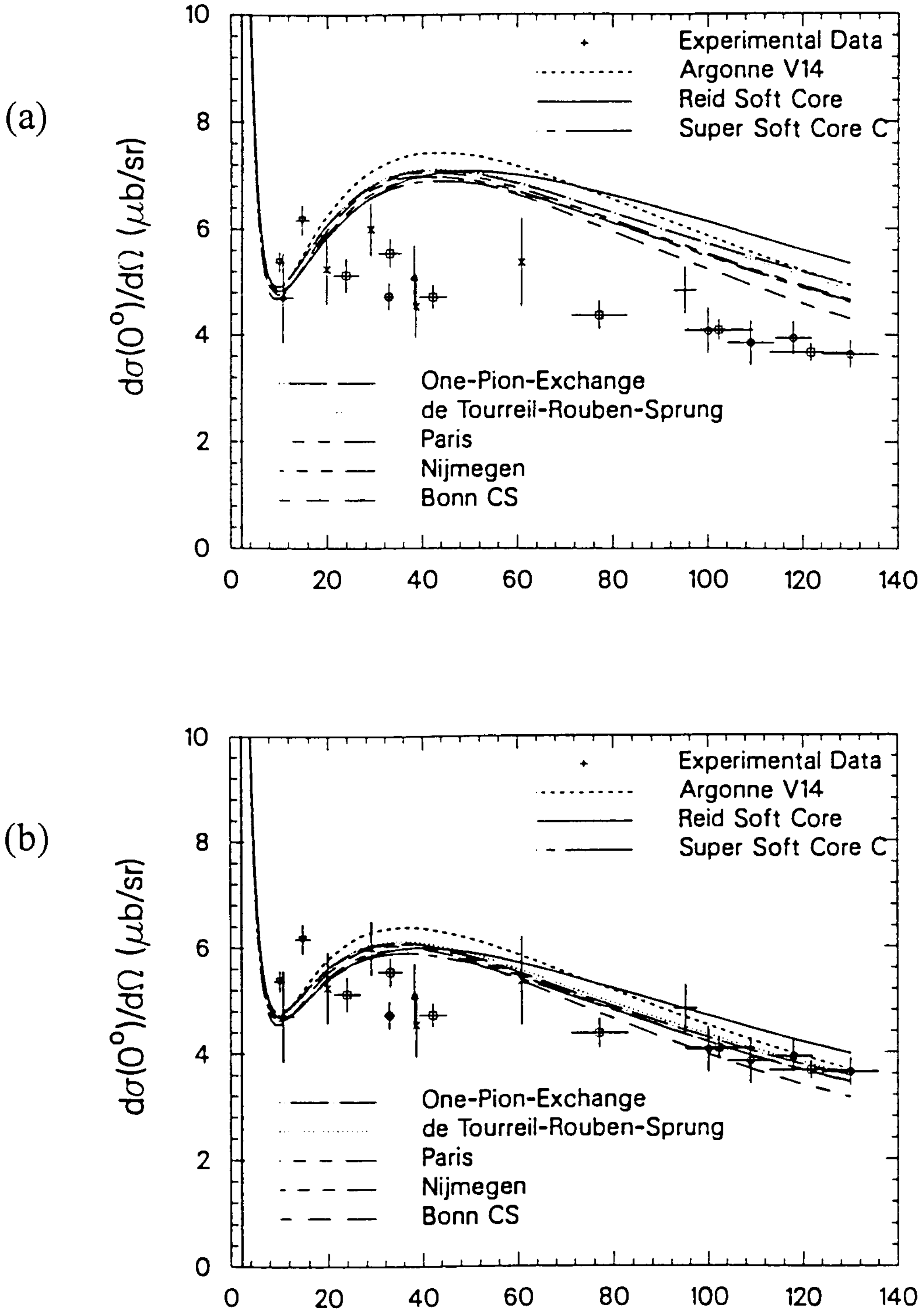

Figure 1-6: *Comparison of experimental measurements of the differential cross section at 0° with potential model calculations based on a range of different potentials when the relativistic correction to the spin-orbit term is (a) omitted and (b) is included in the calculations. Figure from [Sc91].*

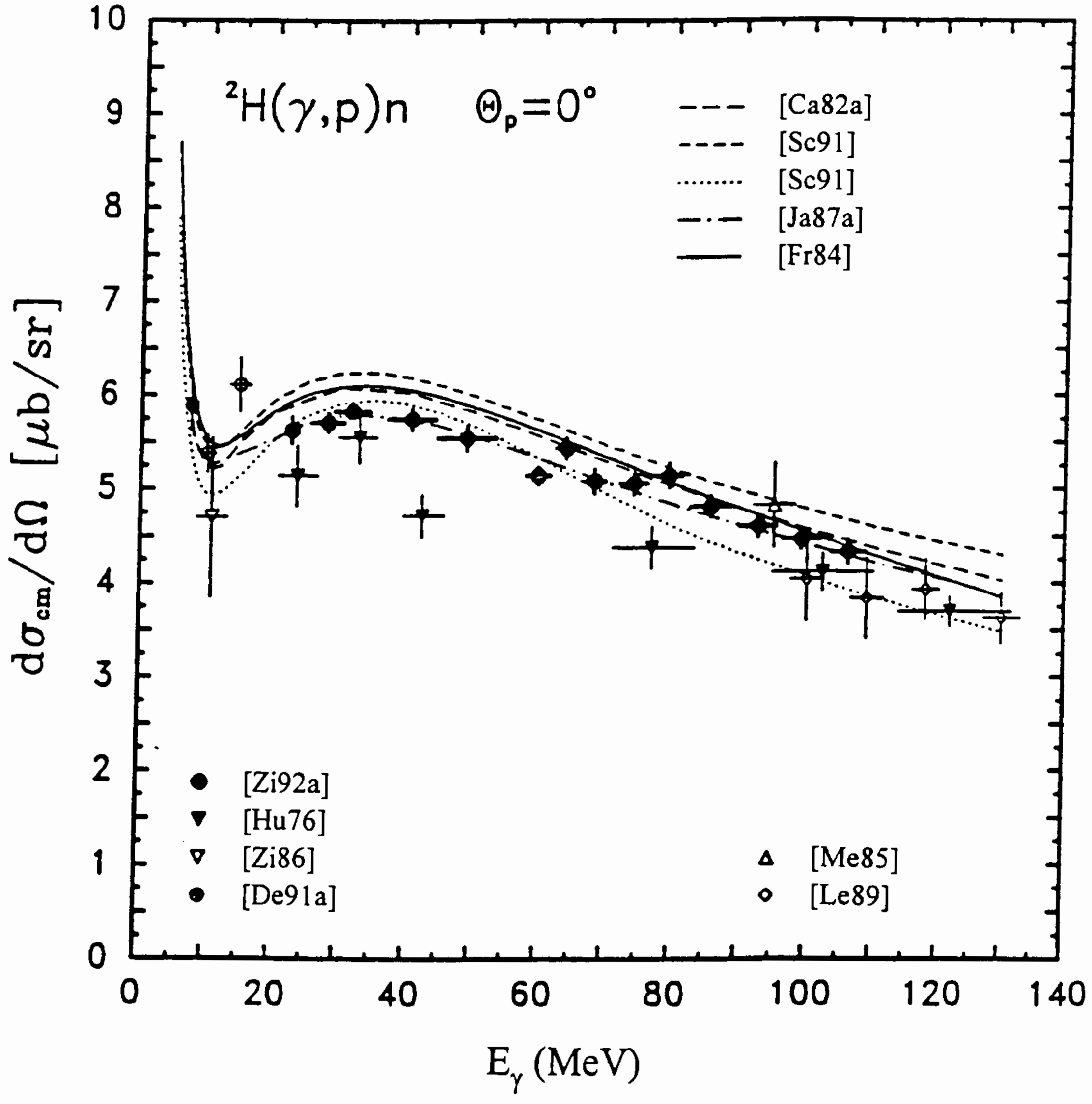

Figure 1-7: *Measurements of the differential cross section at 0° degrees as a function of the photon energy. The full circles are the measurements of Zieger et al. [Zi92a]. The curves indicate various theoretical predictions which are discussed in the text. Figure from [Zi92a].*

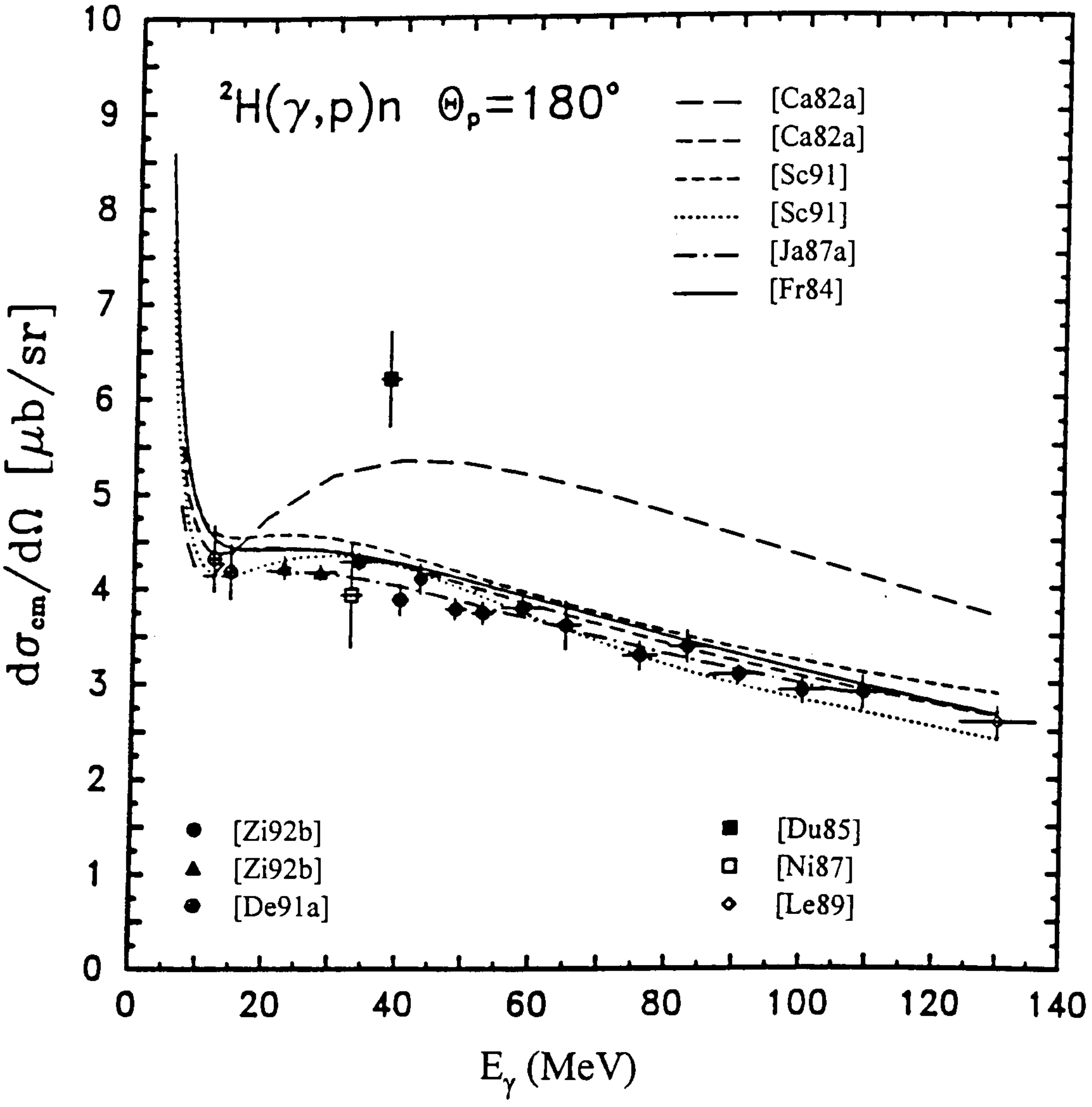

Figure 1-8: *Experimental measurements for the photodisintegration cross section at 180°, together with a number of theoretical predictions. The full circles and full triangles are the recent measurements of Zieger et al. [Zi92b]. Figure from [Zi92b].*

1.4.2 The angular distribution

The majority of measurements of the differential cross section have been made using the bremsstrahlung technique as can be seen from table 1.2 which shows results up to 100 MeV, compared with table 1.3 which shows measurements based on other techniques including n-p capture, tagged photons and positron annihilation. The energies referred to in both tables are photon energies for photodisintegration in the laboratory frame E_γ. The tables are reproduced from ref. [Je94].

Figures 1-9 and 1-10 show comparisons between experiment and theory at three photon energies. Figure 1-9 shows a comparison at 30 MeV, close to the energy of interest to the present work, while figure 1-10(a) shows a similar comparison at 100 MeV, the maximum energy to which the present work can be extended using the current facilities at the National Accelerator Centre at Faure, South Africa. Recently Debevec et al. [De92] used tagged photons to make detailed measurements at a number of photon energies in the range 63 -71 MeV. Figure 1-10(b) shows their results for $E_\gamma =$ 66.9 MeV together with the theoretical predictions of Jaus et al. [Ja93b].

At 30 MeV the data from the different sets of measurements are consistent and the results from potential model calculations appear to be in good agreement with the data [Yi88]. In contrast however, at 100 MeV, the data are not well described by the theory over most of the angular range. The data from different experiments are also not very accurate, particularly at the intermediate angles around 60°. With regard to the measurements of ref. [De92], figure 1-10(b) indicates that there is reasonable agreement between the calculations and the measurements over most of the angular range except at the extreme backward angles.

At energies below 30 MeV, the data of Stephenson et al. [St87], in the energy range 4-18 MeV, are poorly described by potential model calculations. In their experiment, the ratios of the differential cross sections at 45°, 135° and 155° to the cross section at 90° were measured as a function of energy. The results, compared with theoretical calculations, are shown in figure 1-11, from which it is clear that the potential model calculations have failed to predict the measured ratios. It is important to note that the

Table 1.2: *List of angular distribution experiments for photodisintegration at photon energies between 20 and 100 MeV using bremsstrahlung [Je94].*

Energy (MeV)	Data points	Reference
20	5	[Sh70]
20	19	[Sk74]
20	9	[Ha53]
23	6	[Al55]
25	9	[Sh70]
27	7	[We71]
27	7	[Al55]
29	9	[De85]
30	8	[Sh70]
30	7	[We71]
34	7	[Al55]
35	7	[We71]
39	9	[De85]
40	8	[Sh70]
40	7	[We71]
43	7	[We71]
43	7	[Al55]
45	5	[We71]
50	4	[Ga60]
50	4	[We71]
54	6	[Al58]
55	4	[Ga60]
55	4	[We71]
55	5	[Sh70]
60	4	[Ga60]
61	5	[De85]
65	4	[Ga60]
65	5	[Wh56]
70	4	[Ga60]
70	6	[Al58]
70	5	[Sh70]
75	4	[Ga60]
80	4	[Ga60]
80	5	[Wh56]
85	4	[Ga60]
88	7	[Al58]
90	4	[Ga60]
90	5	[Sh70]
100	18	[Ko67]
100	1	[Bu68]

Table 1.3: *List of angular distribution experiments at photon energies between 20 and 100 MeV based on techniques other than bremsstrahlung [Je94].*

Energy (MeV)	Technique	Data points	Ref.
20	n-p capture	3	[Fi91]
22	n-p capture	3	[Fi91]
27	n-p capture	3	[Fi91]
33	n-p capture	2	[Ni87]
38	n-p capture	2	[Du85]
54	tagged photons	7	[Kr92]
60	tagged photons	7	[Kr92]
64	tagged photons	47	[De92]
66	tagged photons	47	[De92]
68	tagged photons	47	[De92]
68	tagged photons	7	[Kr92]
70	tagged photons	47	[De92]
88	tagged photons	6	[Kr92]
92	n-p capture	6	[Ca86]
95	n-p capture	10	[Me85]
100	positron annihilation	2	[Le89]
100	positron annihilation	5	[De86]

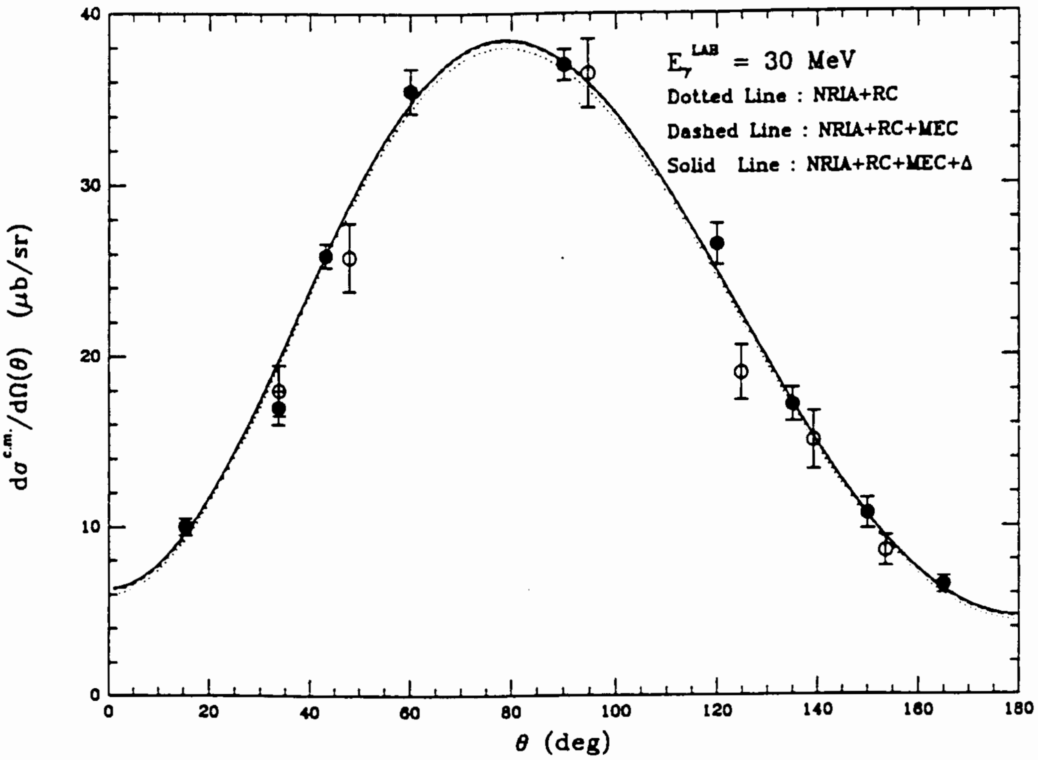

Figure 1-9: *Measurements of the angular distribution from photodisintegration at E_γ = 30 MeV compared with potential model calculations from Ying and Henley [Yi88]. The solid circles are data from De Pascale et al. [De85] and the open circles from Weissman and Schultz [We71]. Figure from [Yi88].*

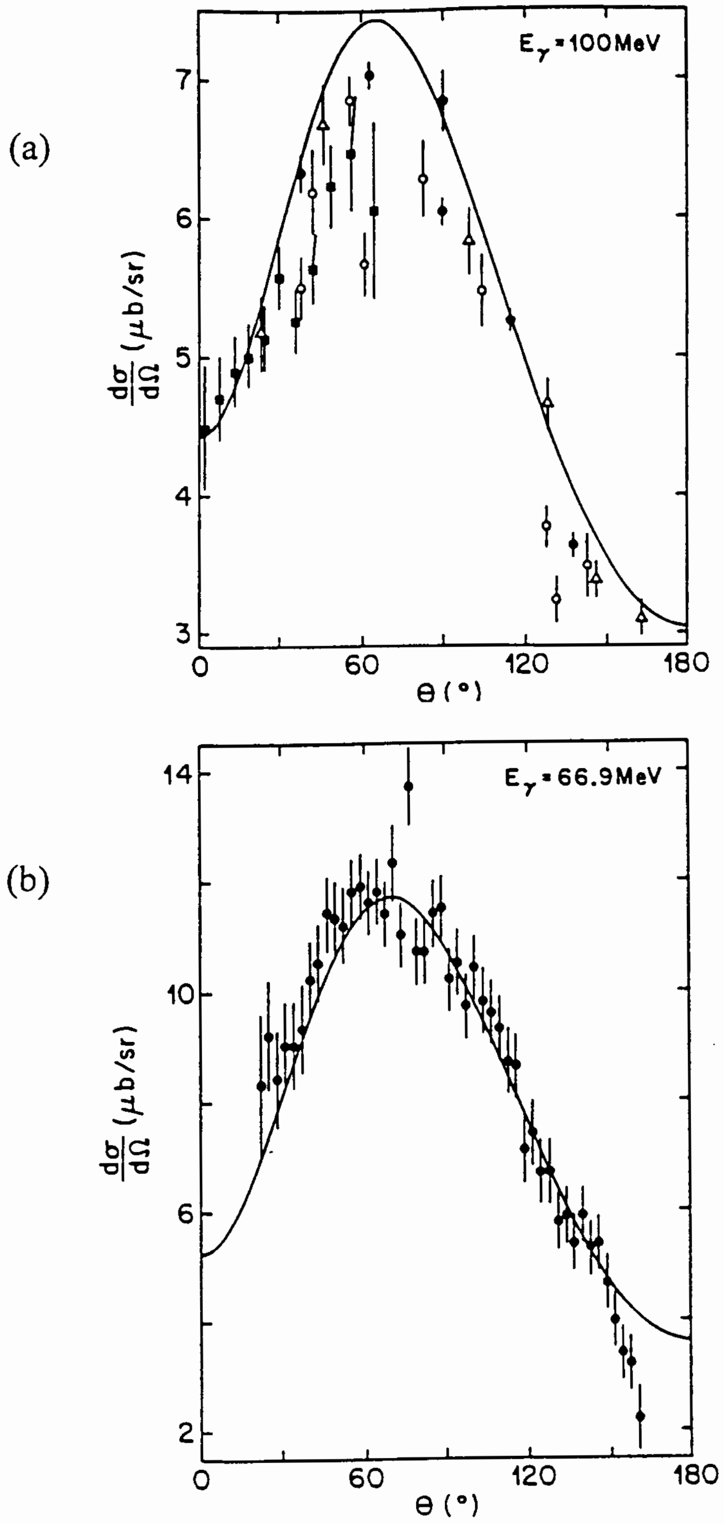

Figure 1-10: *(a) Results from various experiments compared with theory for the differential cross section at a photon energy of 100 MeV; and (b) Measurements by Debevec et al. [De92] of the differential cross section using tagged photons at 66.9 MeV. The solid curves in (a) and (b) are the potential model calculations of Jaus et al. [Ja93b] using the Bonn r-space potential. Figures from ref. [Ja93b].*

measured ratios are almost completely independent of the potential used and are, therefore, expected to be well-described by the calculations of Partovi [Pa64] which do not include any meson-exchange currents apart from the Siegert contributions (see Chapter 2) [Ja93b][Sc91][Ar91]. Although this experiment was later repeated by Birenbaum et al. [Bi88] the error bars were too large to be conclusive.

There has been speculation that the measurements of Stephenson et al. indicate that the standard theory has failed to incorporate the E2 contributions correctly [Ha87]. For example, by making ad-hoc adjustments to the E2 strength of between 25% and 50% it is possible to obtain agreement between theory and experiment [Ha87][Sc91]. However, as yet, there do not appear to be any mechanisms by which such an enhancement may be achieved [Ar91].

1.5 Legendre polynomial coefficients

The differential cross section for photodisintegration $\frac{d\sigma}{d\Omega}$ can be described mathematically by either the Partovi [Pa64] or Legendre polynomial expansions. In each case the terms in these expansions are formally related to the various multipole transitions [Pa64][Ca82b]. The Partovi expansion for the differential cross section for outgoing protons from photodisintegration is given by

$$\frac{d\sigma}{d\Omega} = a + b\sin^2\theta^{cm}_{\gamma,p} + c\cos\theta^{cm}_{\gamma,p} + d\sin^2\theta^{cm}_{\gamma,p}\cos\theta^{cm}_{\gamma,p} + e\sin^4\theta^{cm}_{\gamma,p}$$

where a, b and c are the "Partovi" coefficients of the expansion.

The Legendre polynomial expansion for $\frac{d\sigma}{d\Omega}$ is given by

$$\frac{d\sigma}{d\Omega} = \sum_{l=0}^{\infty} A_l(E_\gamma)P_l(\cos\theta^{cm}_{\gamma,p})$$

where P_l are the Legendre polynomials and A_l are the Legendre polynomial coeffcients. In this expansion the total cross section for photodisintegration is given by $4\pi A_0$.

The relationship between the Legendre polynomial coefficients for a four term ex-

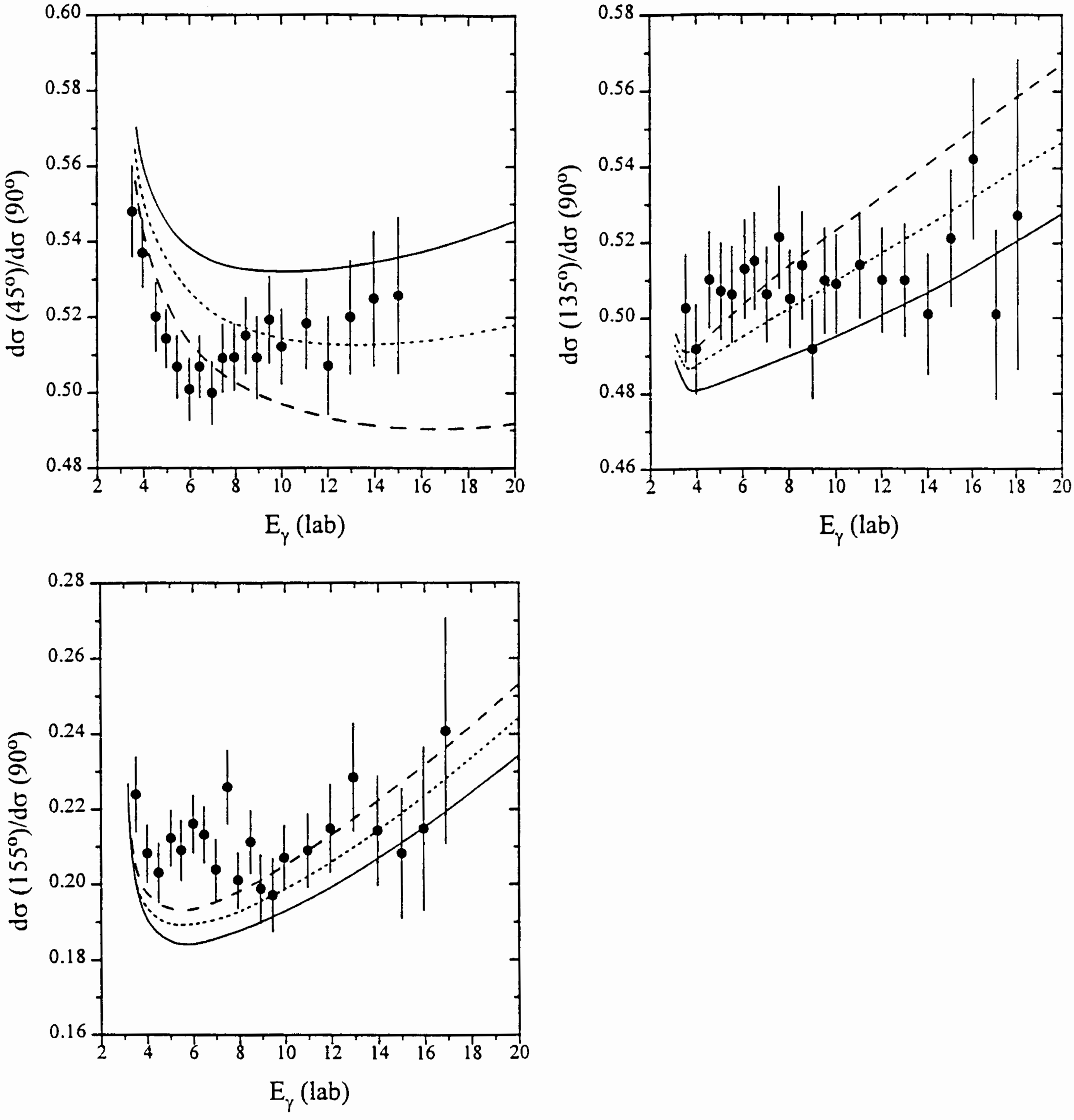

Figure 1-11: *Results of the experiment carried out by Stephenson et al. [St87] compared with calculations based on the Bonn r-space potential. The angles indicated are neutron angles in the laboratory frame. The dotted and dashed lines are calculations with the E2 strength artificially increased by 25 and 50 percent, respectively.*

pansion and the Partovi coefficients are as follows [Sh70]

$$\begin{aligned} a &= A_0 + A_2 \\ b &= -\frac{3}{2}A_2 \\ c &= A_1 + A_3 \\ d &= -\frac{5}{2}A_3 \end{aligned}$$

Although the Partovi expansion is still used, it was shown by Weissman and Schultz [We71] that since the terms in the expansion are not orthogonal, the coefficients cannot be obtained unambiguously from a fit to experimental data. On the other hand, the orthogonality of the Legendre polynomial terms ensures that the coefficients obtained from such a fit are unique, enabling a direct comparison with the values predicted by theory. Cambi et al. [Ca82b] have derived expressions linking the various multipole transition terms to the terms in the Legendre polynomial expansion so that physical conclusions may be inferred from the Legendre polynomial coefficients.

1.5.1 Global fits

A number of global fits to both the total and differential cross section data for photodisintegration have been reported in which the behaviour of the Legendre Polynomial coefficients as a function of energy has been determined. The earliest work was that of De Pascale et al. [De82] in which the available data, up to 120 MeV photon energy, were used to parametrise the energy dependence of the Legendre polynomial coefficients. Later, Thorlacius and Fearing [Th86] used results from experiments in the 10-625 MeV range, while Rossi et al. [Ro89] based their results on data in the range between 20 and 440 MeV. More recently, Jenkins et al. [Je94] have reported fits in the same energy range as Rossi et al. Although Jenkins et al. used the same fitting procedures as Rossi et al. they attempted to distinguish carefully between statistical and systematic errors. In refs. [Th86][Ro89][Je94] the energy dependence of the Legendre polynomial coefficients is described by a phenomenological function of the form

$$A_i(E_\gamma) = C_1 e^{C_2 E_\gamma} + C_3 e^{C_4 E_\gamma} + \frac{C_5 + C_6 E_\gamma}{1 + C_8(E_\gamma - C_7)^2}$$

where C_{1-8} are the parameters in the fit. Calculation of A_0 requires all three terms in the function to be evaluated while the higher order coefficients depend only on the first two terms i.e. on parameters C_{1-8}. Figure 1-12 shows plots of the Legendre polynomial coefficients (A_1, A_2 and A_3) calculated from the global fits of refs. [Ro89] and [Je94] in the energy range 20 to 40 MeV, expressed as ratios to the corresponding values from potential model calculations using the Bonn potential [Sc91].

From figure 1-12 it is clear that there is a discrepancy between theory and experiment for the odd-l coefficients between 20 and 40 MeV, where there is a systematic difference between the trends based on the measurements and theoretical calculations. The fit of Rossi et al. [Ro89], for which the relative uncertainties are about an order of magnitude smaller than those given in references [Th86] and [Je94], also shows a discrepancy with regard to the A_2 coefficient.

1.6 The current work

It is clear from the above discussion that there are a number of puzzles regarding photodisintegration of the deuteron in the energy range below 40 MeV. One particular problem appears to be related to the contribution of the E2 multipole to the cross sections, previously mentioned in relation to the measurements of Stephenson et al. [St87], below 20 MeV. The problems relating to the A_1 and the A_3 Legendre polynomial coefficients between 20 and 40 MeV are possibly also related to the E2 transitions, as both coefficients depend primarily on E2 contributions. However, the observations concerning the Legendre polynomial coefficients for E_γ between 20 and 40 MeV are based on relatively few measurements, as indicated in tables 1.2 and 1.3, with data based on n-p capture ($40 < E_n < 80$ MeV) being particularly scarce. Apart from a number of measurements of the differential cross section corresponding to photoproton angles at 0° and 180° [Gi81][Mi89][Du85][Ni87] angular distribution data at intermediate angles

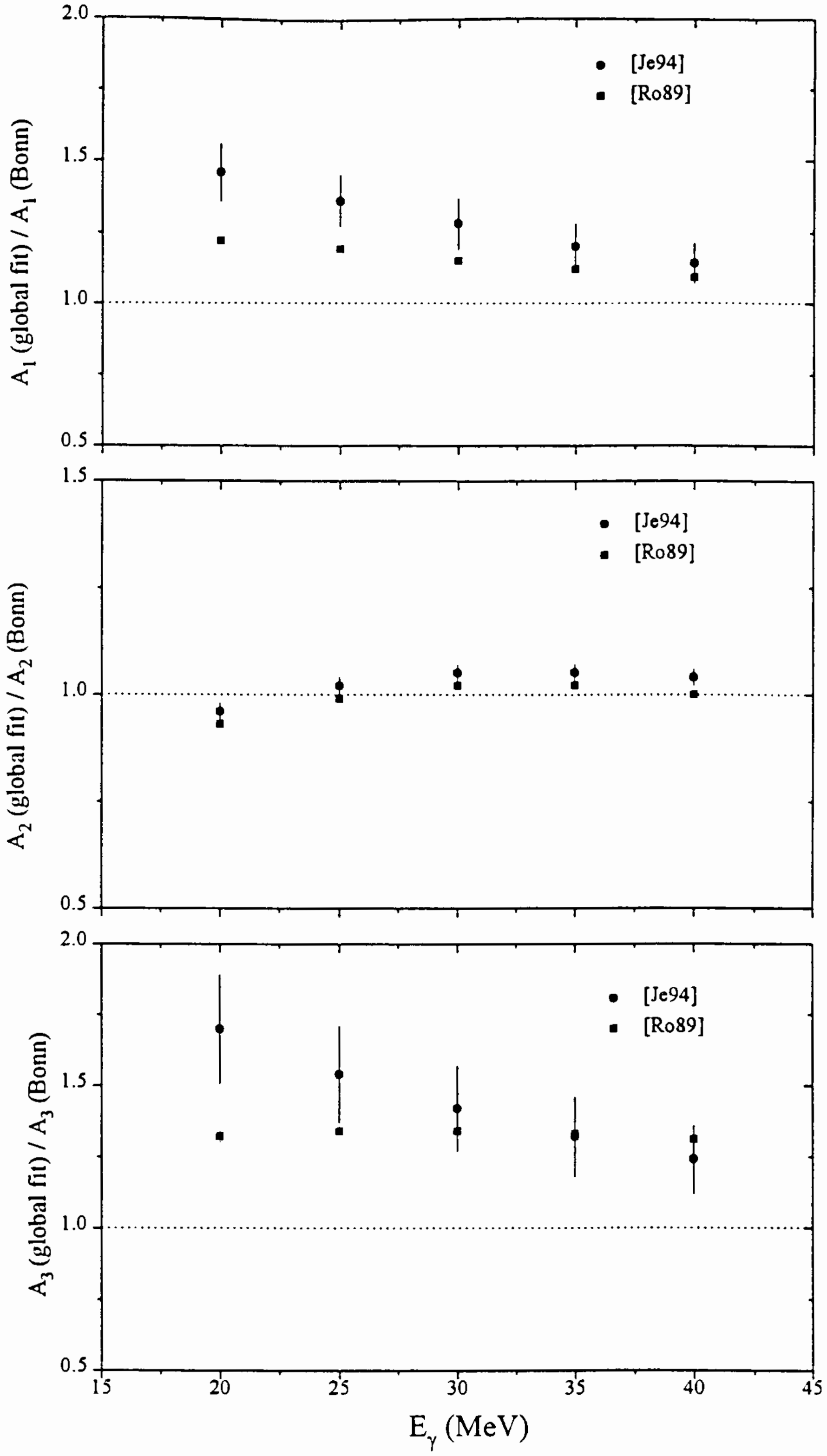

Figure 1-12: *Legendre polynomial coefficients A_1, A_2 and A_3 as a function of photon energy. The results of global fits from Rossi et al. [Ro89] and Jenkins et al. [Je94], evaluated at discrete energies, are compared with potential model calculations based on the Bonn potential.*

are almost non-existent with the exception of the recent measurements of Fink et al. [Fi91]. They have reported measurements for incident neutron energies between 19 and 50 MeV (E_γ=10-27 MeV) at three photon laboratory angles 55°, 90° and 125°. Between 30 and 40 MeV there are no angular distribution measurements based on n-p capture experiments with all the data coming from bremsstrahlung measurements [Al55][Sh70][We71][De85]. Data from n-p capture experiments are especially useful for comparison with those obtained from photodisintegration because the experimental techniques, and hence sources of error, are quite different.

In the work that is presented here, the differential cross section for deuteron photodisintegration $\frac{d\sigma}{d\Omega}$ at the incident photon energy $E_\gamma = 33.9$ MeV has been determined by measuring the angular distribution of photons from n-p radiative capture at $E_n =$ 63.4 MeV. The measurements are based on a new experimental technique in which the deuteron formed in n-p capture is clearly identified using pulse shape discrimination in coincidence with the associated photon [Al93]. The Legendre polynomial coefficients that are derived from a fit to the differential cross section are compared with the coefficients predicted from global fits and from calculations based on potential model theory.

Chapter 2

Theory

2.1 Introduction

This chapter is a brief synopsis of the key elements of potential model theory as applied to photodisintegration of the deuteron and its inverse reaction, neutron-proton capture[1]. The theory that is sketched below describes the photodisintegration reaction $d+\gamma \rightarrow n+p$. The results from n-p capture experiments $(n+p \rightarrow d+\gamma)$ can be transformed to equivalent measurements for photodisintegration by detailed balance (Section 2.8). The discussion, based largely on refs. [Ar91][Pa64][Ca82b][Sc89][Sc90][Yi88][Ma88], describes the key elements of the theory, namely, (i) the initial bound n-p system which interacts via a potential, (ii) the final unbound n-p state of the continuum, (iii) the deuteron currents, (iv) the photon field and (v) the interaction of the photon field with the deuteron currents. The coupling of the radiation field with the currents leads to a number of reaction amplitudes via electric and magnetic transitions which may be characterised in terms of their multipole fields. The link between the observables of interest and the multipole fields is achieved via the transition or T-matrix which may be expressed either in terms of the observables or in terms of the multipole fields. Formally, the T-matrix is related to the scattering S-matrix which arises in scattering theory, as detailed, for example, in Appendix C of ref. [Wo90]. The differential cross

---

[1] Note that both c and $\hbar$ are set equal to 1 in the discussion.

section for photodisintegration $\frac{d\sigma}{d\Omega}$ is given in terms of the T-matrix as [Ar91]

$$\frac{d\sigma}{d\Omega} = \frac{(2\pi)^{10}}{4W}\frac{k}{\omega}|T|^2 \tag{2.1}$$

where W is the total energy in the centre-of-mass, $\vec{\omega}$ is the photon momentum and $\vec{k}$ is the relative neutron momentum. In the density matrix formulation [Ei76][Me61] the differential cross section is expressed in terms of the trace Tr of the product of the matrices

$$\frac{d\sigma}{d\Omega} = Tr(T\rho T^+) \tag{2.2}$$

where ρ is the product of the photon and the deuteron 2×2 density matrices ρ^D and ρ^γ, respectively.

2.2 The initial n-p system

The n-p system which is bound via a potential into the deuteron, is described by the non-relativistic wave function comprising S and D-wave components. The wave function $|m_d\rangle$, where m_d is the deuteron spin projection quantum number, can be expressed in terms of the spin-angle function $\mathcal{Y}_{ls}^{jm}(\vec{r})$ where $\vec{r}$ is the relative coordinate of the nucleons

$$|m_d\rangle = \left[\frac{u_0(r)}{r}\mathcal{Y}_{11}^{1m_d}(\vec{r}) + \frac{u_2(r)}{r}\mathcal{Y}_{11}^{2m_d}(\vec{r})\right] \tag{2.3}$$

The functions $u_0(r)$ and $u_2(r)$ are solutions of the radial part of the Schrödinger equation. The spin-angle functions are defined in terms of the spherical harmonics $Y_m^l(\vec{r})$ and the Pauli spinors $\chi_{m_s}^s$ as

$$\mathcal{Y}_{ls}^{jm}(\vec{r}) = \sum_{m_l m_s} (lm_l, sm_s \mid jm) Y_{lm}(\vec{r})\chi_{m_s}^s \tag{2.4}$$

where the first term is a Clebsch-Gordan coefficient.

2.3 The final n-p state

The final n-p state $|sm_s\rangle$ is an outgoing scattering solution of the p-n continuum, characterised by the relative momentum[2] $\vec{k}$, the spin s and its projection m_s on $\vec{k}$,

$$|sm_s\rangle = \Psi_{sm_s} = \sum_{\mu jl} \sqrt{4\pi(2l+1)}\, \langle l0, sm_j \mid jm_s\rangle\, e^{-i\delta^j_\lambda} U^j_{ls\mu}\, |\mu jm_s\rangle \tag{2.5}$$

where $U^j_{ls\mu}$ is the 4×4 coupling matrix containing a coupling parameter ϵ_j and whose rows are labelled by (ls) and columns by μ = 1,2,3, or 4. The partial waves $|\mu jm_s\rangle$ are solutions of a system of coupled equations given by

$$|\mu jm_s\rangle = \sum_{l's'} i_{l'} U^{j'}_{l's'\mu'} \frac{v^{j}_{l's'\mu'}(kr)}{kr} \mathcal{Y}^{jm_s}_{l's'}(\overrightarrow{r}) \tag{2.6}$$

where $v^{j'}_{l's'\lambda'}(kr)$ are the radial wave functions which satisfy the Schrödinger equation for a given a N-N potential.

2.4 Deuteron currents

The deuteron current density $\vec{J}$ contains parts arising from the internal motion of the nucleons as well as from the motion of the centre-of-mass. Since the latter does not contribute to the transitions in the interaction with the photon field, only the intrinsic nuclear current density $\vec{j}$ needs to be specified. The current density can be separated into a number of constituent parts comprising an orbital or convection current (conv), a spin current (spin) and currents due to meson-exchange (MEC) and isobar configurations (IC)

$$\vec{j} = \vec{j}^{conv} + \vec{j}^{spin} + \vec{j}^{MEC} + \vec{j}^{IC} \tag{2.7}$$

The convection and spin parts are one-body currents i.e. $\vec{j}_{(1)}$ while the remain-

---

[2] The relative momentum of the neutron with respect to the proton $\vec{p}_{n,p} = \vec{p}$ is defined as $\frac{1}{2}(\vec{p}_n - \vec{p}_p)$. Since $\vec{p} = (\hbar)\vec{k}$ it follows that $\vec{k} = \frac{1}{2}(\vec{k}_n - \vec{k}_{p)} = \frac{1}{2}\vec{k}_n$.

ing terms are many-body in nature with the two-body currents $\vec{j}_{(2)}$ being the most important part of the exchange terms.

2.5 The photon field

The photon field is characterised by the vector potential $\vec{A}(\vec{x})$ which can be expanded in terms of plane waves of circular polarisation as follows

$$\vec{A}(\vec{x}) = \sqrt{\Omega_N}\sum_{\omega}\sum_{\lambda=\pm1}\sqrt{(\frac{2\pi}{\omega})}(\hat{a}_{\omega\lambda}\vec{\varepsilon}_{\lambda}e^{i\vec{\omega}\cdot\vec{x}} - \hat{a}^{+}_{\omega\lambda}\vec{\varepsilon}_{(-\lambda)}e^{-i\vec{\omega}\cdot\vec{x}}) \tag{2.8}$$

where $\hat{a}_{\omega\lambda}$ is the annihilation operator for a photon of momentum $\vec{\omega}$ and polarisation λ with the polarisation vector given by $\vec{\varepsilon}_{\lambda}$.

2.6 Interaction of the photon field with the deuteron currents

The interaction of the bound n-p system with the photon field is given by the electromagnetic transition Hamiltonian H'_{em} which couples the photon field with the current density (operator) $\vec{J}(\vec{x})$

$$H'_{em} = \int \vec{J}(\vec{x}) \cdot \vec{A}(\vec{x}) d\vec{x} \tag{2.9}$$

To first order in perturbation theory the transition matrix T is proportional to H'_{em} i.e.

$$\left\langle sm_s \mid H'_{em} \mid \lambda m_d \right\rangle = \langle sm_s \mid T \mid \lambda m_d \rangle \tag{2.10}$$

and evaluating the term on the left hand side of the equation leads directly to the differential cross section as noted in equation 2.1. Thus, the interaction is expressed as

$$\langle sm_s \mid T \mid \lambda m_d \rangle = \sqrt{\frac{kM}{4\pi\omega}} \int d^3x e^{i\vec{\omega}\cdot\vec{x}} \left\langle sm_s \mid \vec{\epsilon}_{\lambda} \cdot \vec{j}(\vec{x}) \mid m_d \right\rangle \tag{2.11}$$

2.7 Evaluation of the T-matrix

Evaluation of the matrix element in equation 2.11, leads to the expansion of the current operator in terms of the electric and magnetic multipole operators $\hat{E}_{LM}$ and $\hat{M}_{LM}$, respectively. Thus,

$$\int d^3x \; \epsilon_\lambda \cdot \hat{j}(\vec{x}) e^{i\vec{\omega}\cdot\vec{x}} = -\sqrt{2\pi} \sum_{LM} \hat{L}(\hat{E}_{LM} + \hat{M}_{LM}) D^{L}_{M\lambda}(0, \theta, \phi) \tag{2.12}$$

where D is the rotation matrix that rotates the photon momentum $\vec{\omega}$ through the polar angles (θ, ϕ) onto the axis along the relative momentum $\vec{k}$. The electric and magnetic multipole operators are defined as

$$\hat{E}_{LM} = \int d^3x \; \hat{j}(\vec{x}) \cdot \vec{A}^{el}_{LM}(\vec{x}) \tag{2.13}$$

$$\hat{M}_{LM} = \int d^3x \; \hat{j}(\vec{x}) \cdot \vec{A}^{mag}_{LM}(\vec{x}) \tag{2.14}$$

with the electric and magnetic vector potentials given by

$$\vec{A}^{mag}_{LM}(\vec{x}) = -\frac{i^{L+1}}{\sqrt{L(L+1)}} \vec{r} \times \vec{\nabla}) j_L(\omega r) Y_{LM}(\hat{x}) \tag{2.15}$$

$$\vec{A}^{el}_{LM}(\vec{x}) = \frac{1}{ik\sqrt{L(L+1)}} \vec{\nabla} \times (\vec{x} \times \vec{\nabla})(j_L(kx) Y_{LM}(\hat{x})) \tag{2.16}$$

The form of the current density operator $\hat{j}$ now needs to be specified. The current density can be separated into one- and two-body operators i.e. $\hat{j} = \hat{j}_{(1)} + \hat{j}_{(2)}$ where the one-body operator $\hat{j}_{(1)}$ comprises the sum of the orbital or convection current and the spin current $\hat{j}^{conv}_{(1)} + \hat{j}^{spin}_{(1)}$. The one-body current operator for non-interacting point nucleons is given by

$$\hat{j}_{(1)}(\vec{x}) = \frac{1}{2M} \sum_{\alpha} (e_\alpha [\vec{p}_\alpha, \delta(\vec{x} - \vec{r}_\alpha)] + i\mu_\alpha \vec{\sigma}_\alpha \times [\vec{p}_\alpha, \delta(\vec{x} - \vec{r}_\alpha)] \tag{2.17}$$

where the subscript α specifies the α^{th} particle, e the charge, μ the magnetic moment, $\vec{r}$ the particle coordinate, $\vec{p}$ the momentum and $\vec{\sigma}$ the spin operator. The two

-body operator, or the exchange operator, $\hat{j}_{(2)}$, arises as a result of the interaction between the particles. The details of this operator follow from considering a model in which the nucleon couples to the meson and isobar degrees of freedom. However, in the photon energy range of interest, it is possible to evaluate the dominant part of the matrix element due to the electric multipole transitions without having to consider the MEC's explicitly. This is achieved by using the so-called Siegert operators, discussed below, which depend only on the one-body charge density operator $\hat{\rho}_{(1)}$. For non-interacting point nucleons $\hat{\rho}_{(1)}$ is given by the expression

$$\hat{\rho}_{(1)}(\vec{x}) = \sum_{\alpha} e_\alpha \delta(\vec{x} - \vec{r}_\alpha) \tag{2.18}$$

2.7.1 Siegert's theorem and Siegert operators

Siegert's theorem [Si37], which has played an important role in photodisintegration calculations, can be stated in the following form [Yi88]

$$\lim_{\omega \to 0} H'_{em} = -\lim_{\omega \to 0} \int d^3x \;\; \vec{A}(\vec{x}) \cdot [\hat{H}, \vec{x}\hat{\rho}_{(1)}(\vec{x})] \tag{2.19}$$

Thus, in the low energy limit, the interaction Hamiltonian for electric transitions is given simply in terms of the one-body charge density operator $\hat{\rho}_{(1)}$, providing that the gauge that is chosen obeys this limit. If this is so, then the charge exchange contributions tend to zero ($\hat{\rho}_{(2)} \to 0$) in the non-relativistic limit. In addition it can be shown [Sc89] that by using the Siegert operators, which follow as a consequence of the theorem, the dominant part of the two-body current exchange contributions $\hat{j}_{(2)}$ is included. In order to construct the Siegert operator, the vector potential is separated out into the sum of the gradient of a scalar field and a vector field

$$\vec{A}^{el}_{LM}(\vec{x}) = \frac{i^{L+1}}{\omega} \vec{\nabla}(\Phi_{LM}(\vec{x}) + \vec{A}'^{(el)}_{LM}(\vec{x}) \tag{2.20}$$

Compliance with the low energy theorem means that only a limited class of gauges are allowed and the scalar function is restricted to the form [Sc89][Sc90][Yi88] indicated in equation 2.21 below. (It is interesting to note that the Coulomb, or transverse, gauge

$(\Phi_{LM} \equiv 0)$ falls outside the restricted class). Thus,

$$\Phi_{LM}(\vec{x},\omega) = \frac{i}{\sqrt{L(L+1)}}\frac{1}{\omega}\left(\frac{L+1}{(2L+1)!!}z^L + \varphi_L(z)\right)Y_{LM}(\vec{x}) \tag{2.21}$$

where $z = \omega x$ and φ_L is an arbitrary function providing that it satisfies the limit

$$\lim_{z\to 0} \varphi_L(z) = \mathbf{O}(z^{L+2}) \tag{2.22}$$

The continuity equation, expressing current conservation, has the form

$$\vec{\nabla}\cdot\hat{\jmath}(\vec{x}) + [\hat{H},\hat{\rho}(\vec{x})] = 0 \tag{2.23}$$

where $\hat{H}$ is the intrinsic Hamiltonian operator and $\hat{\rho}(\vec{x})$ is the charge density operator. Hence, the electric multipole operator may be written as

$$\hat{E}_{LM} = \frac{i^l}{\omega}[H, \int d^3x\ \hat{\rho}(\vec{x})\Phi_L(\omega x)Y_{LM}] + \int d^3x\hat{\jmath}(\vec{x})\cdot\vec{A}'^{(el)}_{LM}(\vec{x}) \tag{2.24}$$

where the commutator with the Hamiltonian is known as the Siegert operator. It can be shown that the contributions due to $\vec{A}'^{(el)}_{LM}$ will be small compared with the contribution from the Siegert operator. The reason for using the Siegert operator is contained in the following argument. The charge density operator can be separated into one- and two-body parts and written as

$$\hat{\rho}(\vec{x}) = \hat{\rho}_{(1)}(\vec{x}) + \hat{\rho}_{(2)}(\vec{x}) \tag{2.25}$$

Since the Hamiltonian operator is the sum of the kinetic energy and the potential operators i.e. $\hat{H} = \hat{T} + \hat{V}$, the continuity equation can be separated into one-body and two-body parts as follows [Ar91],

$$\vec{\nabla}\cdot\hat{\jmath}_{(1)}(\vec{x}) + i[\hat{T},\hat{\rho}_{(1)}(\vec{x})] = 0 \tag{2.26}$$

$$\vec{\nabla}\cdot\hat{\jmath}_{(2)}(\vec{x}) + i[\hat{T},\hat{\rho}_{(2)}(\vec{x})] + i[\hat{V},\hat{\rho}_{(1)}(\vec{x})] = 0 \tag{2.27}$$

Since $\hat{\rho}_{(2)}(\vec{x})$ vanishes in the low energy limit as discussed above, it is clear that the Siegert operator will include part of the exchange currents $\hat{j}_{(2)}$ via the potential part of the commutator. Using various OBE approximations to the full Bonn potential, it has been demonstrated in ref. [Sc89] that this part is in fact the dominant contribution of the exchange currents and includes MEC's beyond π and ρ. However, if the potential does not commute with the one-body charge density operator additional currents have to be included explicitly so as to satisfy current conservation. This is the case with all the phenomenological meson exchange potentials such as Paris, Bonn, Nijmegen etc. since these potentials are both momentum and isospin dependent.

The use of the Siegert operator is limited to electric transitions. Thus, the form of both the one- and two-body current density operators have to specified in dealing with magnetic transitions. In calculations typified by for example, refs. [Ru60][Pa64], only the one-body currents are considered in dealing with the magnetic transitions. In more recent work meson-exchange currents beyond those included in the Siegert operator and isobar configurations are treated explicitly. The approach in which there is no *explicit* inclusion of MEC's, or IC's is often referred to as the impulse approximation (IA). A short summary of MEC's, IC's as well as of relativistic corrections (RC) follows in section 2.7.2

2.7.2 Meson-exchange currents and isobar configurations

The meson-exchange currents can be divided into long range, medium range and short range [Ja93a]. The long range part consists of the exchange of single pions $\pi's$, while the medium range part is considered to involve the exchange of multiple pions and heavier mesons e.g. ρ and ω mesons. The short range part, however, is unknown at this stage [Ja93a]. The leading order part of the pionic exchange current $\vec{j}_\pi$ is the summation of the so-called seagull Feynman diagram, which describes the contact and pair currents, and the pion current diagram as shown below in figure 2-1.

A similar set of diagrams may also be drawn for the exchange of the vector-mesons of which the ρ is the most important [Sc89]. In order to evaluate the contribution to the transition it is necessary to specify the forms of each of the currents, such as

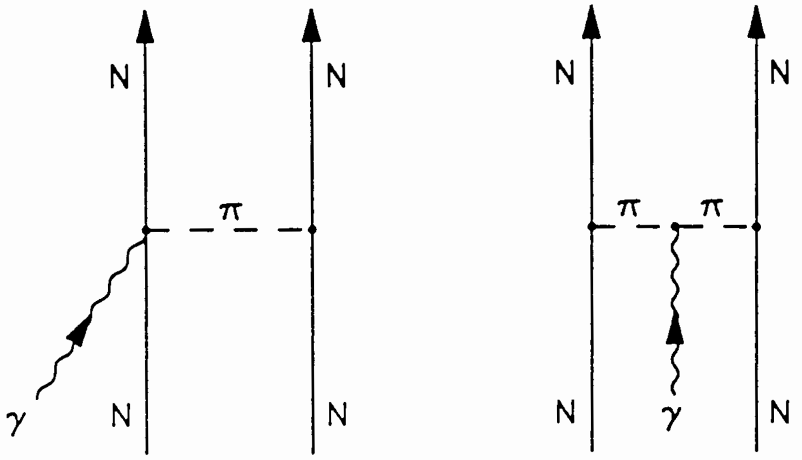

Figure 2-1: *Pion-exchange-current diagrams. The left hand diagram depicts the contact or pair current and the right diagram shows the pion current. Figure from [Ar91].*

the ones mentioned. However, the diagrams have to be evaluated in a way that is consistent with the potential and also satisfies gauge invariance. One of the problems that arises, for example, relates to the isospin-dependence of the potentials (Paris, Bonn, Nijmegen etc.) in that the standard approach of introducing the electromagnetic field via minimal substitution fails to produce the isovector part of the exchange current that is required to satisfy the continuity equation[Sa93]. Similarly, minimal substitution does not ensure gauge invariance for a momentum-dependent potential.

A number of ways have been used in dealing with the problem as mentioned in refs. [Yi88][Sc89][Ja93a][Ma88], based on the fact that the potentials all include aspects of meson-exchange e.g. pion exchange to describe the long range part. One way of deriving the form of the pionic exchange current $\vec{j}_\pi$ is as follows. A one-pion-exchange potential V_π^{OPE} is constructed as detailed in ref. [Sc89], for example, and then using minimal coupling ($\vec{p} \longrightarrow \vec{p} - q\vec{A}$ in the potential) [Sa93] and taking the necessary derivative, the pion-exchange current operator is given by an expression which involves the πNN coupling constant $f_{\pi NN}$, and the nucleon spin and isospin operators. The terms in the expression may be associated with the various diagrams above. In this case it may be shown that the continuity equation is satisfied i.e.

$$\vec{\nabla} \cdot \vec{j}_{\pi} + +i[\hat{V}^{OPE}, \hat{\rho}_{(1)}] = 0 \tag{2.28}$$

The ρ-exchange current may be treated likewise. Similar methods have also been developed for constructing two-body currents for the phenomenological potentials by, for example, Partovi [Pa87] and Sadegi et al. [Sa93]. Although there has been concern about the degree to which gauge invariance is violated in such procedures, it appears to be negligible at the lower energies. For example, Schmitt et al. [Sc90] have shown that at 30 MeV the gauge dependence, for the restricted class of gauges mentioned earlier, is about 1%.

In addition to the MEC's mentioned there are also currents associated with the internal degrees of freedom of the nucleon, i.e. with the virtual excitations of isobars, in particular the $\Delta(1232)$ resonance. Examples of these contributions to $\vec{j}^{\Delta}$, the isobar current, are shown in the Feynman diagrams of figure 2-2 below.

Refs. [Yi88][Sc89][Ja93a][Ma88] contain discussions as to how the contributions are evaluated and added to obtain the final multipole amplitudes. As noted in ref. [Ar91], the operator which corresponds to this current is non-local owing to the intermediate isobar propagation and has to be approximated by a local operator which introduces a measure of uncertainty into the calculation.

2.7.3 Relativistic corrections

Two types of relativistic corrections affect the calculations. The first correction involves the current operator, and the second relates to the wave function. In particular, the relativistic spin-orbit current plays an important role as was first demonstrated by Cambi et al. [Ca82a] with regard to the 0° cross section. Wilhelm et al. [Wi88] have shown that this effect is essentially a two-body exchange effect and that the Siegert operator constructed from the relativistically corrected spin-orbit one-body charge density $\rho^{so}_{(1),RC}$ describes the full spin-orbit $\vec{j}^{so}$current well. The charge density

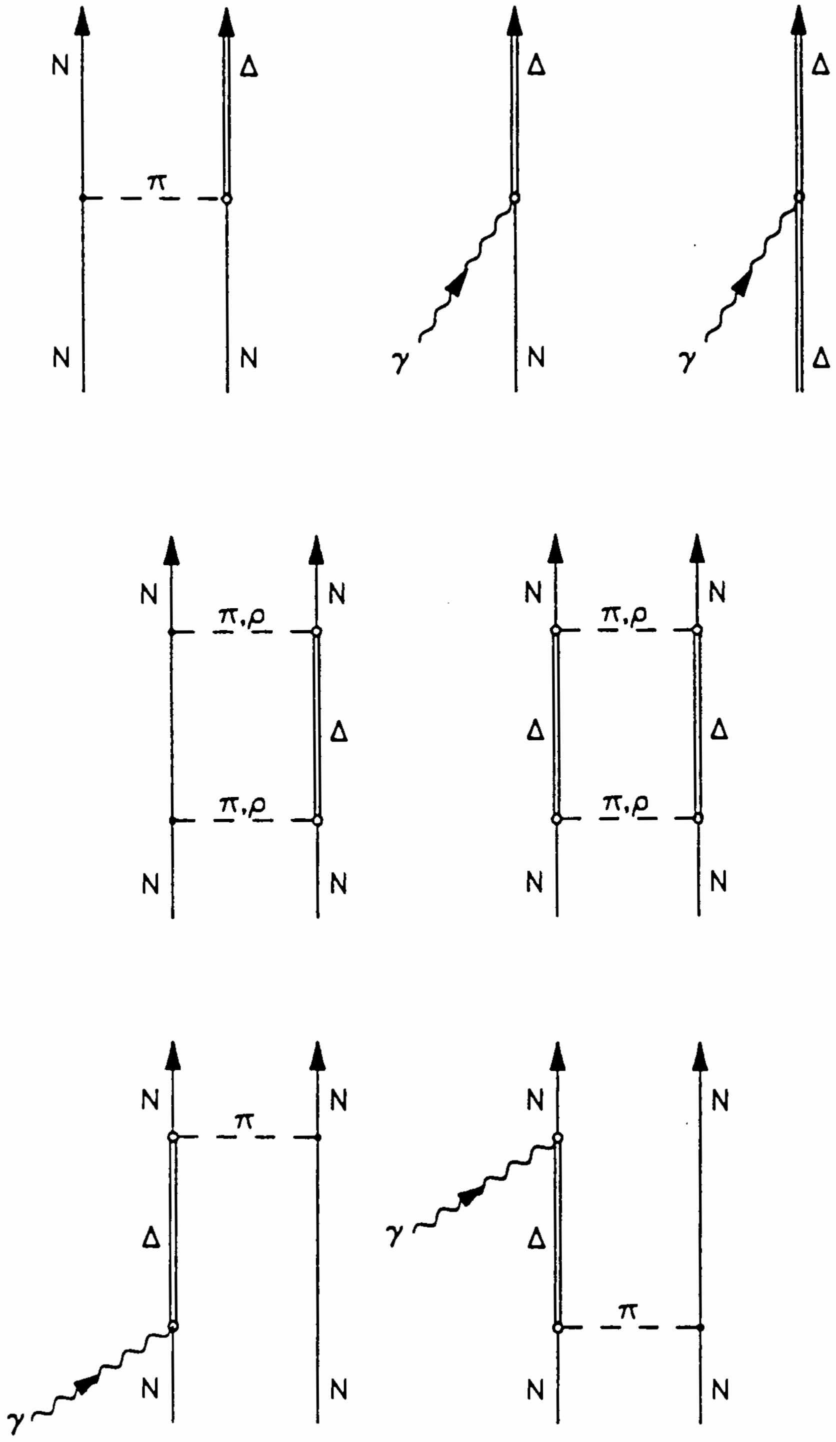

Figure 2-2: *Feynman diagrams showing the processes that contribute to the isobar current. Figure from [Ar91].*

is given by [Ca82a][Wi88]

$$\rho^{so}_{(1),RC}(\vec{x}) = \sum_i \frac{2\mu_i - e_1}{8M^2}\{\vec{\sigma}_i \times \vec{p}_i, \vec{\nabla}_x \delta(\vec{x} - \vec{r}_{i)}\} \tag{2.29}$$

where $\vec{r}_i$, $\vec{p}_i$ and $\vec{\sigma}_i$ are the position, momentum and spin of the i^{th} nucleon and e_i, μ_i and M are its charge, magnetic moment and mass, respectively. The full current $\vec{j}^{so}_{RC}$, which contains both one-body and two-body parts, can be written in the form [Wi88]

$$\vec{j}^{so}_{RC}(\vec{x}) = -i \sum_i \left[H, \frac{2\mu_i - e_1}{8M^2}\{\vec{\sigma}_i \times \vec{p}_i, \vec{\nabla}_x \delta(\vec{x} - \vec{r}_{i)}\}\right] \tag{2.30}$$

The second type of relativistic correction is generated from boosting the initial deuteron wave function from the rest frame to the centre-of-mass frame of the reaction. This can be treated as an additional current density between the initial and final states but is expected to be negligible at the energies in question [Yi88].

2.7.4 Relative contributions of the various effects

Figure 2-3, taken from [Sc91], shows the relative contributions of the various currents to the total cross section as a function of photon energy using the Bonn r-space potential. In this figure, "one-body" implies that the contributions from the one-body convection and spin currents were evaluated without using Siegert operators while the so-called "normal" contribution (N) implies that Siegert operators were used to evaluate the electric transitions and that only the one-body current was used to evaluate the amplitudes for the magnetic transitions. The effect of contributions beyond this non-relativistic impulse approximation (NRIA) are indicated as MEC($\pi + \rho$) for meson-exchange of $\pi's$ and $\rho's$ while IC shows the effect of adding the isobar configurations. The relativistic corrections are indicated by RC. The importance of the various multipole contributions to the differential cross section are discussed in more detail in chapter 5

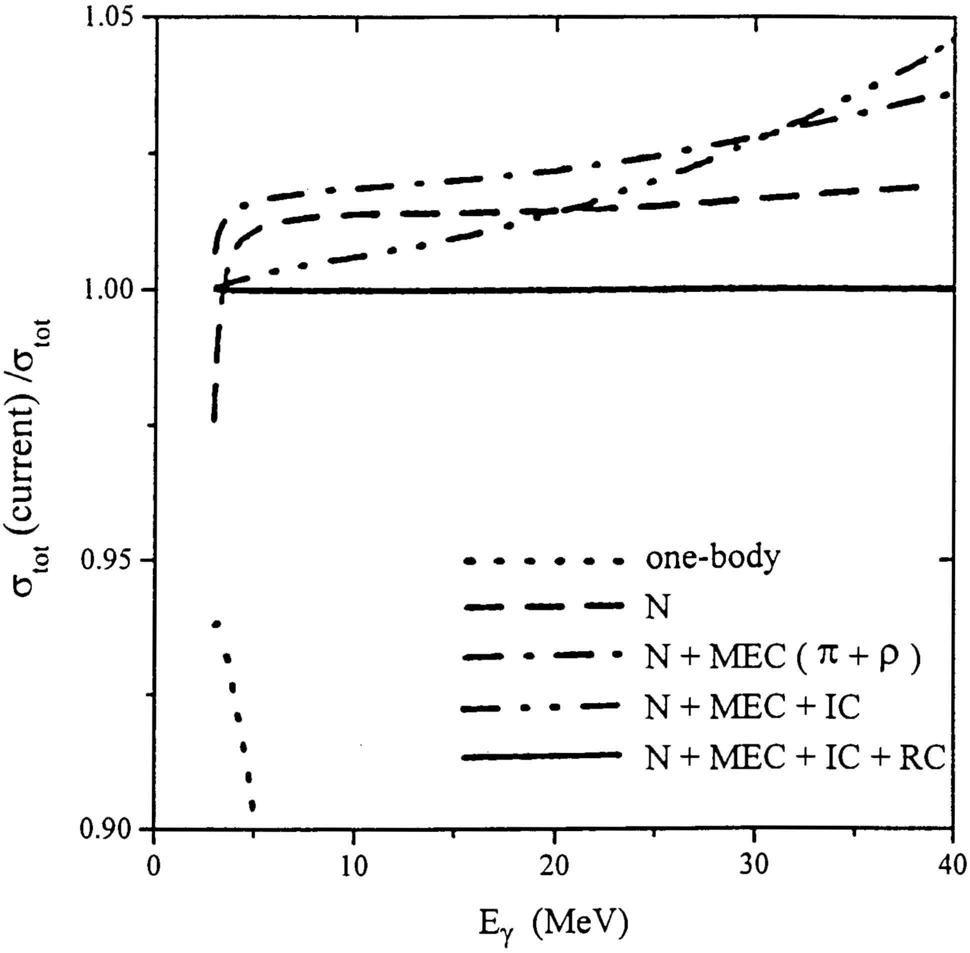

Figure 2-3: *Relative contributions to the total cross section for the Bonn r-space potential from the various electromagnetic curents. The nomenclature is described in the text. Figure from [Sc91].*

2.8 The principle of detailed balance

The cross-sections that are obtained from n-p capture measurements are related to photodisintegration cross sections by the principle of detailed balance [Ma69][Po95]. For the two inverse reactions shown below

$$\begin{aligned} n+p &\longrightarrow d+\gamma : \ [1 \rightarrow 2] \\ d+\gamma &\longrightarrow n+p : \ [2 \rightarrow 1] \end{aligned} \tag{2.31}$$

the transition probabilities W are given by Fermi's golden rule as

$$W_{1\rightarrow 2} = \frac{2\pi}{\hbar}\left|H'_{1,2}\right|^2 \left(\frac{dN}{dE}\right)_2 \tag{2.32}$$

$$W_{2\rightarrow 1} = \frac{2\pi}{\hbar}\left|H'_{2,1}\right|^2 \left(\frac{dN}{dE}\right)_1 \tag{2.33}$$

where $\frac{dN}{dE}$ is the density of states. However, since

$$H'_{1,2} = (H'_{2,1})^* \tag{2.34}$$

it follows that

$$\frac{W_{1\rightarrow 2}}{\left(\frac{dN}{dE}\right)_2} = \frac{W_{2\rightarrow 1}}{\left(\frac{dN}{dE}\right)_1} \tag{2.35}$$

Normalising the incident wave to unit density and evaluating the number of final states per unit energy the above relationship can be written in terms of the cross-sections σ and the statistical weights g for the reactions [Be56]

$$\frac{\sigma_{2\rightarrow 1}}{\sigma_{1\rightarrow 2}} = \frac{g_d g_\gamma p_\gamma^2}{g_n g_p p_{n,p}^2} \tag{2.36}$$

where $\vec{p}_{n,p} = \vec{k}$ is the relative momentum of the neutron and the proton and $\vec{p}_\gamma = \vec{\omega}$ is the momentum of the gamma in the centre-of-mass frame. For an unpolarised photon the statistical weight is 2 which corresponds to the two possible directions of polarisation since the photon cannot be polarised in the direction of propagation. For a particle of angular momentum I the statistical weight will be $2I+1$, therefore the statistical weight of the spin 1 deuteron is 3 while that of the two spin $\frac{1}{2}$ nucleons are 2 each. This leads to the relationship between the cross sections for photodisintegration and n-p capture, namely,

$$\left(\frac{d\sigma}{d\Omega}\right)_{photodis} = \frac{2}{3}\left(\frac{k^2}{\omega^2}\right)\left(\frac{d\sigma}{d\Omega}\right)_{capture} \tag{2.37}$$

where k is the magnitude of the neutron relative to the proton in the centre-of-mass frame and ω is the magnitude of the photon momentum in the centre-of-mass frame. The following expressions [Ar91][Pa64][Hw84], based on the kinematics of the reaction [Ar91][Pa64][Hw84], can be used to calculate k^2 and ω^2, respectively,

$$k^2 = \frac{1}{W^2}(W^2 - (m_p + m_n)^2(W^2 - (m_p - m_n)^2) \tag{2.38}$$

$$\omega = \omega^{lab}\left(1 + \frac{2\omega^{lab}}{m_d}\right)^{\frac{1}{2}} \tag{2.39}$$

$$W = m_d\left(1 + \frac{2\omega^{lab}}{m_d}\right)^{\frac{1}{2}} \tag{2.40}$$

where W is the invariant mass of the sytem, ω^{lab} is the magnitude of the photon momentum in the laboratory frame, and m_p, m_n, and m_d are the masses of the proton, neutron and deuteron, respectively. Appendix A contains more details about the kinematics of the reaction.

Equations 2.38, 2.39 and 2.40 can be used to calculate the detailed balance factor $\left[\frac{2}{3}\left(\frac{k^2}{\omega^2}\right)\right]$ at various neutron energies E_n as shown in figure 2-4. The present work was carried out at $E_n = 63.4$ MeV, for which the detailed balance factor was calculated to be 17.3, as indicated by the solid circle in figure 2-4.

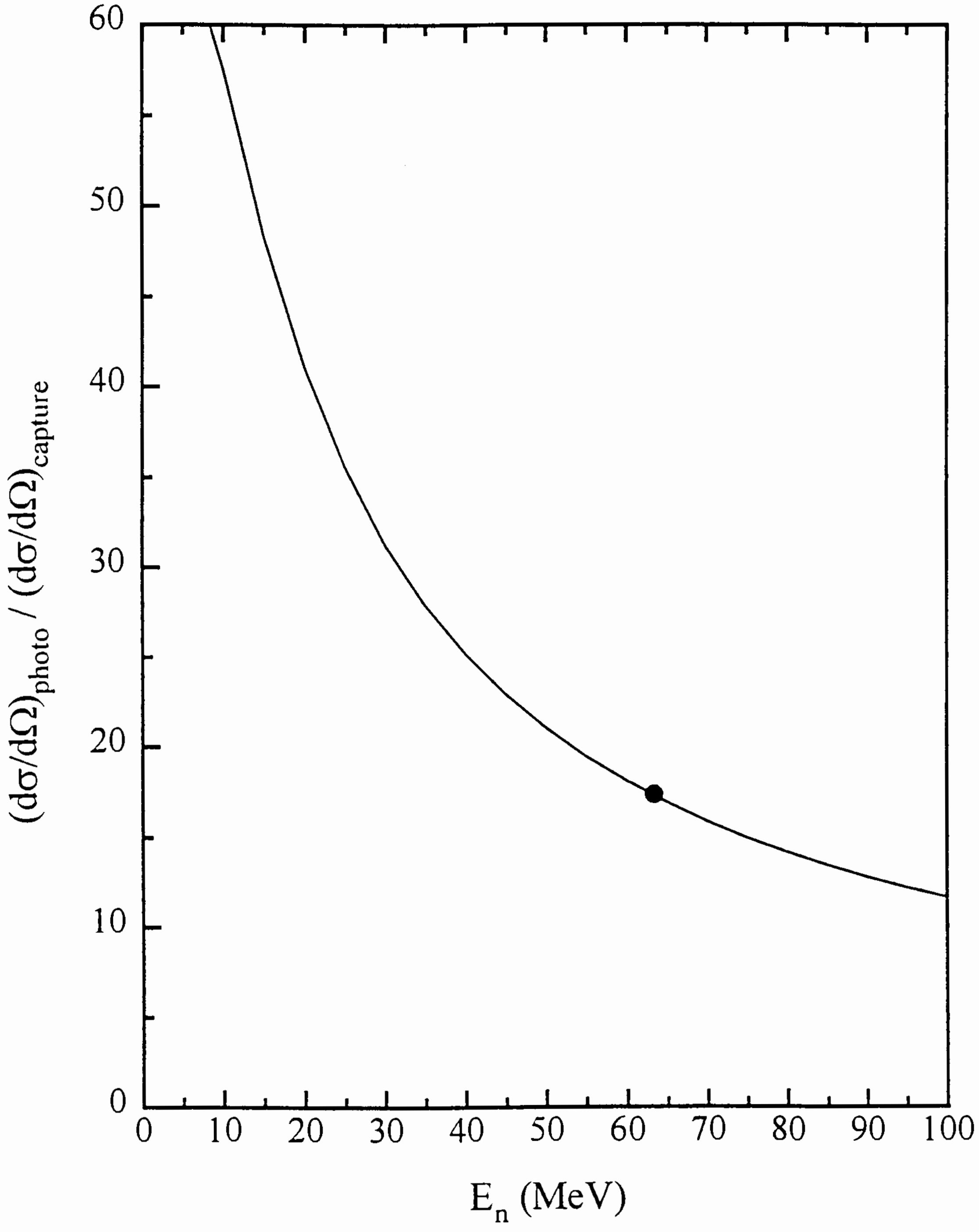

Figure 2-4: *Detailed balance factor as a function of neutron energy. The solid point indicates the neutron energy (63.4 MeV) at which the present work was carried out.*

Chapter 3

Measurements

3.1 Experimental arrangement

The main features of the experimental arrangement are shown in the schematic diagram in figure 3-1. The experiment consisted of directing a neutron beam onto a cyclindrical cell (50 mm diam. x 50 mm) of NE213 liquid scintillator placed at the vertex of the experiment (figure 3-1). NE213 has a density 0.874 g cm^{-1} and a hydrogen to carbon ratio of 1.212. A small fraction of the neutrons interact with the protons by the radiative capture reaction, $np \rightarrow d\gamma$. The resulting deuterons were detected in the scintillator with almost 100% efficiency and identified by pulse shape discrimination. Some of the associated gamma rays were detected in eight identical sodium iodide Na(Tl) crystals (75 mm diam. x 125 mm), which were placed in a ring around the NE213 vertex at angles relative to the neutron beam $\theta^{lab}_{n,\gamma}$ of 45°, 60°, 75°, 90°, 105°, 120°, 135° and 150° . The distance from the centre of the vertex to the front face of the crystals was 200 mm. Each crystal was placed inside a rectangularly shaped lead shield (132 mm x 132 mm x 142 mm long). Charged particles originating from the vertex were excluded from the NaI(Tl) crystals by a lead plate 5 mm thick mounted over the entrance of the detectors. The gamma flight time over the gap between the NE213 cell and the NaI(Tl) crystals (figure 3-1) was used to reject backgrounds due to non-relativistic particles that were detected in the crystals. Figure 3-2 shows a photograph of the experiment looking towards the vertex along the incoming neutron beam. The three detectors marked X were part of a separate experiment and do not form part of this work. The experiment was carried out at the National Accelerator Centre (NAC) in Faure, outside Cape Town, South Africa using the k=200 separated-sector cyclotron (SSC).

3.2 Neutron production

Pulsed neutrons of mean energy $E_n = 63.4$ MeV were produced from the ^{7}Li(p,n)^{7}Be reaction by directing a beam of 66.0 MeV protons onto a 4.5 mm thick target of natural lithium metal. The target was made by compressing solid lithium in a hydraulic press, placed between two foils of havar, each 2.5 μm thick, and mounted in an aluminium frame which was attached to a water-cooled holder.

A collimated neutron beam was formed by passing the neutrons through an aperture (50 mm x 50 mm) in a shielding wall 2.5 m thick between the lithium target and the NE213 cell (figure 3-1). The flight path of the neutrons (the distance from the lithium target to the vertex) was 5.940(5) m. Time-of-flight was used to select the strong forward peak in the neutron spectrum corresponding to the transitions ^{7}Li(p,n)^{7}Be (gs+0.43 MeV). About 10% of the neutrons in the peak are due to transitions to the 0.43 MeV state [Ra90]. The mean energy of the neutrons in the peak was calculated from the Q-value of the ground-state transition (-1.644 MeV [Aj84]) and the average energy loss of the protons in the lithium target which was calculated to be 1.0 MeV. The spread in the neutron energy was estimated to be of the order of the average energy loss of the protons in the target i.e. $E_n = 63.4 \pm 1$ MeV.

At 66 MeV the cyclotron facility provides bursts of protons every 61 ns. Every fifth proton beam pulse was selected giving a time of 305 ns between pulses. This reduced the energy at which neutrons from successive bursts overlapped at the detector to 1.4 MeV. Dead time and pile-up in the electronics were reduced by limiting the proton current to about 300 nA. Protons which were transmitted through the lithium target were deflected into a beam dump as indicated in figure 3-1.

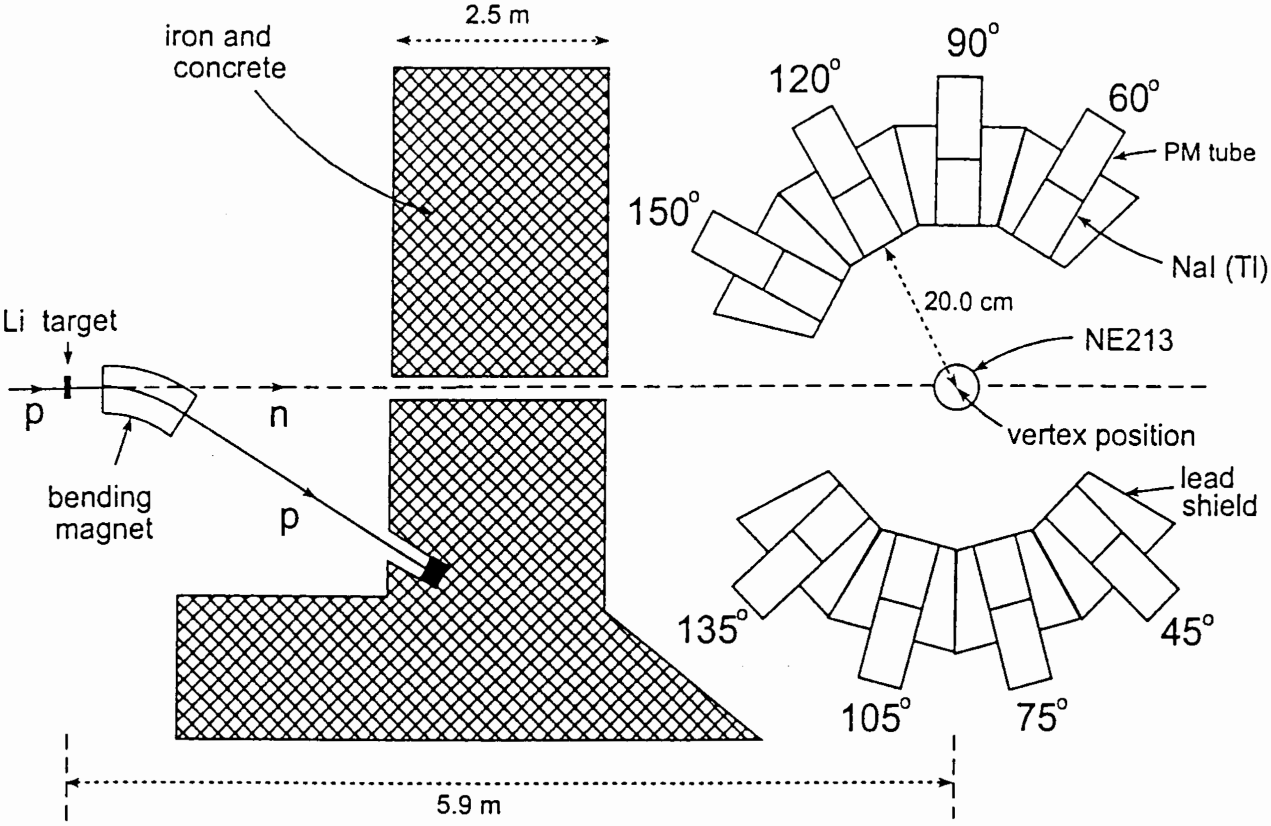

Figure 3-1: *Schematic diagram of the main features of the experiment showing the neutron time of flight facility at the NAC and the experimental configuration comprising an NE213 liquid scintillator cell (50 mm diam. x 50 mm) placed at the vertex and surrounded by eight Na(Tl) detectors (75 mm diam. x 125 mm). Figure adapted from [Al93].*

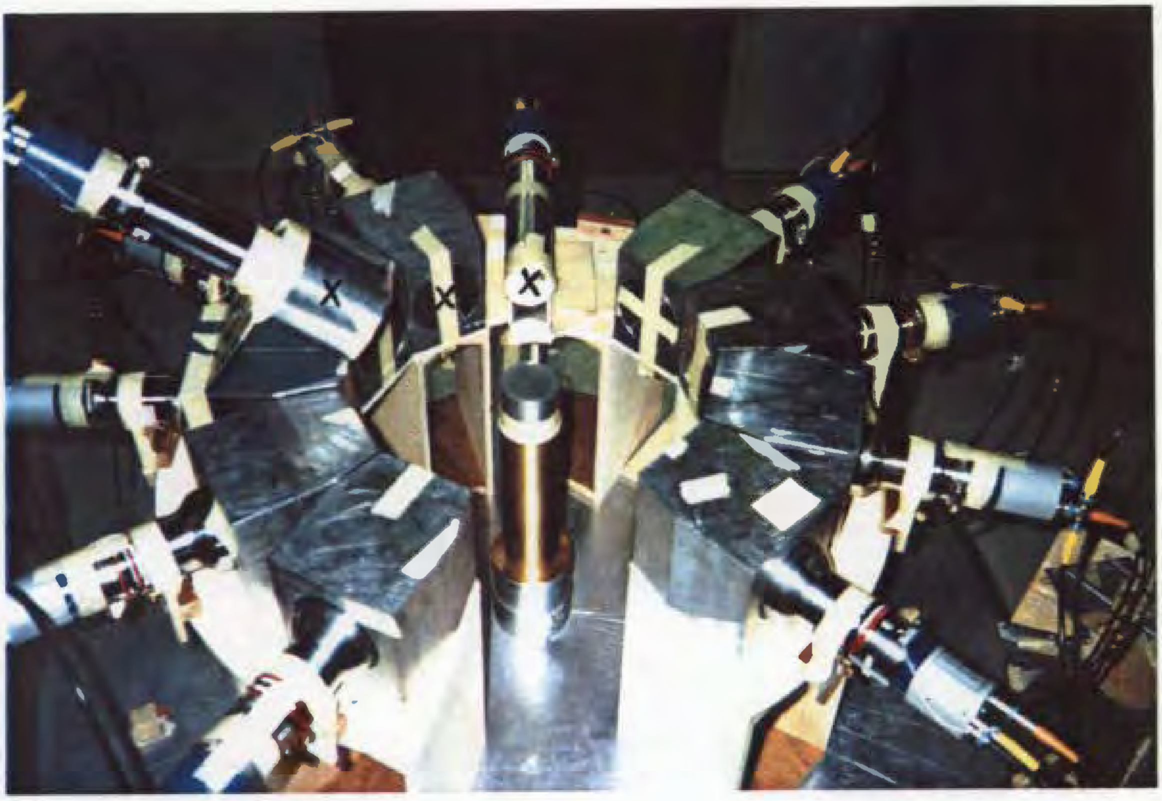

Figure 3-2: *Photograph of the experiment looking towards the vertex along the incoming neutron beam. The NE213 liquid scintillator cell is shown at the centre, placed on top of a brass tube used to adjust the height. The lead shields surrounding each of the Na(Tl) detectors are clearly seen. The protrusions from the back of each detector are part of the phototube assembly. The three detectors marked with an X are part of a separate experiment and are not part of this work.*

3.3 Electronics

A schematic diagram indicating the main features of the electronic configuration is shown in figure 3-3. Signals were produced from three sources, namely, the NE213 detector, the NaI(Tl) detectors and a reference signal from the cyclotron. Pulses from the NE213 were fed into a modified Link Systems Model 5010 Pulse Shape Discriminator (LINK) [Ad78] which provided two outputs, L and F [Sm86][Sm87]. The pulse height L was generated by integrating the scintillation pulse over a period of 500 ns while the F pulse was obtained by integrating over 30 ns [Sm87]. The scintillation pulse shape parameter S was derived from the L and the F pulses by combining them in the form

$$S = L - kF + C$$

where k and C are arbitrary constants which are set in the off-line analysis of the data. A logic signal P_n was provided by the LINK for events that were identified by PSD as due to neutrons. The LINK also provided a timing output which was used to start the time-to-amplitude converters (TAC) that measured the neutron time-of-flight T_n and the coincidence time delay between the NE213 and the Na(Tl) detectors T_G. A timing output, synchronised to the cyclotron radio-frequency, was used to stop the T_n TAC. A detailed schematic diagram of the electronic system is shown in figure 3-4.

Outputs were taken from both the 5th dynodes and the anodes of the photomultipliers viewing the eight Na(Tl) detectors. The dynode outputs were coupled together and fed to a common pre-amplifier and amplifier chain for the NaI(Tl) pulse height (energy) measurements G. The $G-$threshold for the experiment was set by a timing single channel analyser (TSCA) fed by an auxiliary amplifier connected in parallel with the G amplifier. This arrangement ensured that changes could be made to the $G-$gain without interfering with the threshold and vice-versa. A logic pulse P_G was produced for events in which G was above a threshold of about 10 MeV for runs with the neutron beam, or about 1 MeV for runs with radioactive sources.

The anode outputs from the NaI(Tl) detectors were fed to individual fast amplifiers and fast constant fraction discriminators (CFD) for fast timing and detector identification. Each discriminator provided a single bit input to the pattern register R (figure 3-4) for detector identification. A separate output from each discriminator was fed via a ns-delay (for matching) to a logic fan-in (FIFO) which generated a common fast output that was used as the "stop" pulse for the T_G TAC. This arrangement ensured that dead times were the same for all eight of the detectors during data acquisition.

A logic pulse P_{T_n} was generated by the T_n TAC for an event in which T_n satisfied the time window selecting 63.4 MeV neutrons. A logic pulse P_{T_G} was also generated by the T_G TAC for events in which T_G fell within the coincidence time peak. The logic pulses (P_n, P_G, P_{T_G}, and P_{T_n}) were fed into a universal coincidence (UCO) together with a logic level from the data acquisition computer which indicated when computer was "not busy" ($\overline{Busy}$). The UCO generated a logic pulse for an n-fold coincidence ($n \leq 5$), which depended on the coincidence requirements for a particular run. The logic pulse from the UCO was used to gate the linear gate and stretchers (LGS's) allowing the data to be passed the ADC's for analogue to digital conversion. All of the logic ouputs outlined above were used simultaneously for radiative capture measurements. Different subsets of these conditions were imposed for calibration measurements.

The data acquisition system was based around a VAX 730 running XSYS data acquisition software. Output from the ADC's were fed into a a CAMAC interface which was linked to the VAX via a Micro Branch Driver. Event by event data were recorded in memory and buffered in 4k blocks to nine-track magnetic tape for off-line analysis.

3.4 Calibrations

3.4.1 Source calibrations

Energy and time calibrations were performed using ^{60}Co and ^{241}Am/^{9}Be (AmBe) sources as well as the neutron beam. The cobalt source provided two gamma ray energies of 1.17 MeV and 1.33 MeV while the AmBe source provided a neutron spectrum predominantly below 10 MeV, as well as a photon of 4.43 MeV from the transition of

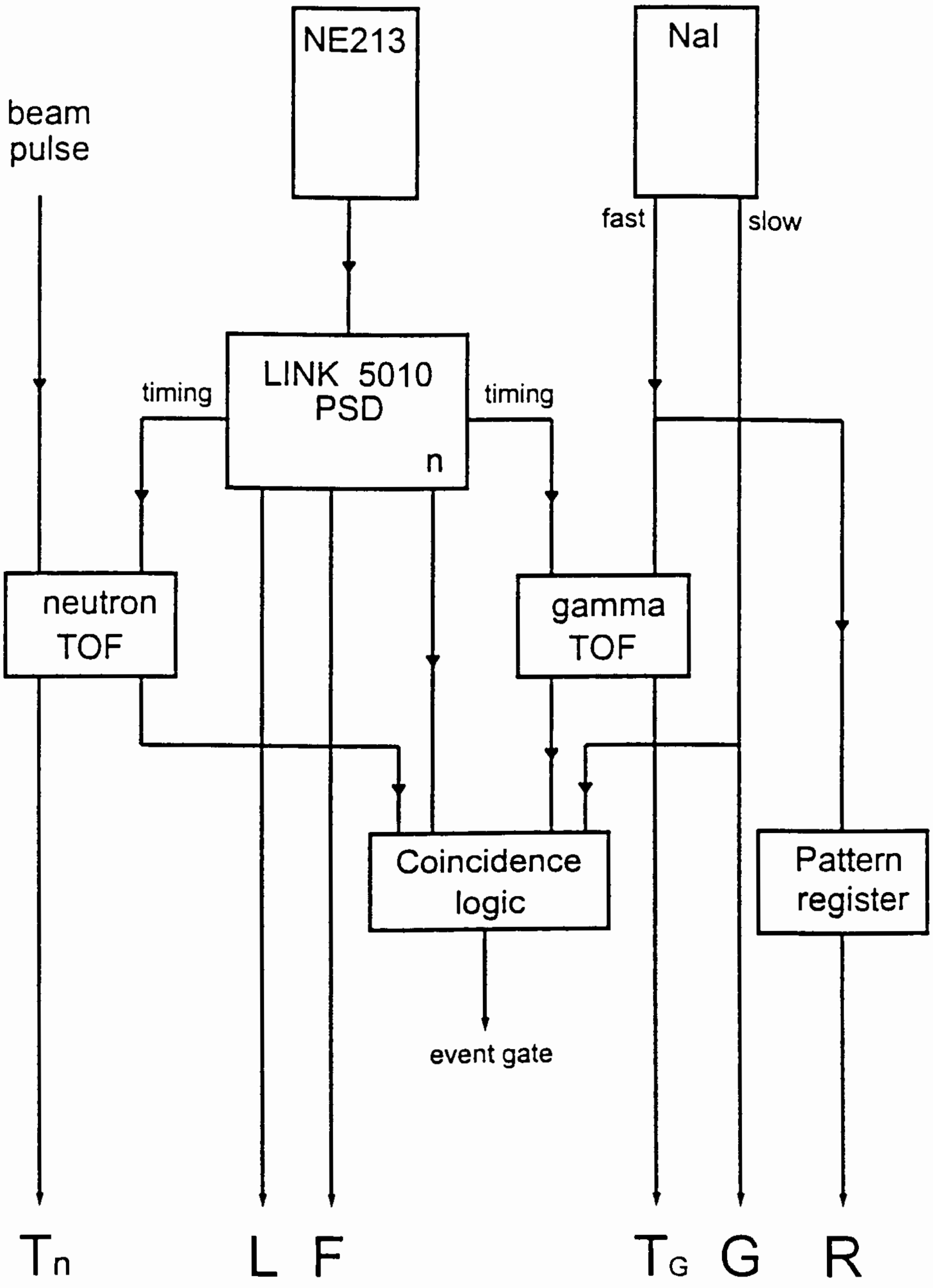

Figure 3-3: *Diagram of the main features of the electronic system used in the experiments. A six-parameter event was recorded on buffer tape for each accepted event.*

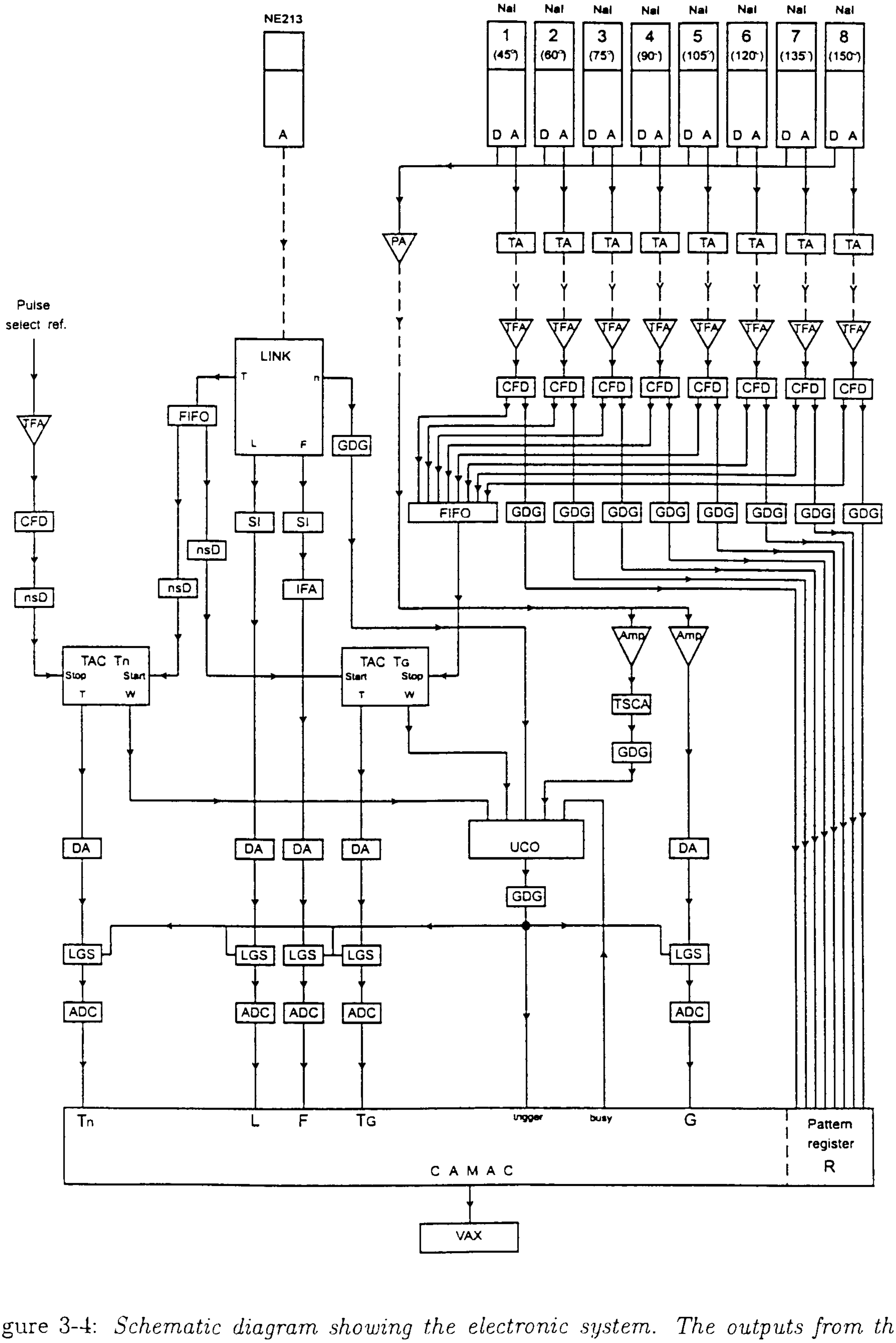

Figure 3-4: *Schematic diagram showing the electronic system. The outputs from the ADC's were routed via a CAMAC interface to a dedicated VAX 730 running XSYS software.*

$^{12}C^*$ to the ^{12}C ground state[1]. This photon also provided two other calibration points at 3.92 MeV and 3.41 MeV. These energies are associated with the escape of one or both of the annihilation photons from the Na(Tl) detectors.

Calibrated nanosecond delays were used to calibrate T_n and T_G. For T_n "time zero" T_0 was determined from the gamma peak in the time of flight spectrum (obtained with PSD off) due to photons produced by protons striking the lithium target. The time scale and T_0 were used to establish an energy scale for the T_n spectrum. The 4.43 MeV photons and the associated neutrons emitted by the AmBe source were used to set up the timing for the coincidence electronics by detecting the gammas in the sodium iodide in coincidence with the neutrons in the NE213 cell. The neutrons and gammas from the AmBe source were also used to set the preliminary pulse shape parameter settings on the LINK module before using the neutron beam for the final settings. Pulse shape discrimination was used on-line to suppress a fraction of the background events associated with gamma production in the vertex NE213 cell.

Thresholds and gains for the sodium iodide detectors were set up using the gamma rays from the sources mentioned. The ^{60}Co was used to set up the thresholds on the sodium iodide detectors while the 4.43 MeV gamma ray from the AmBe source was used for energy calibration. During these calibrations amplifier gains were set either five times or ten times higher than during beam runs, assuming that the thresholds would scale accordingly when the gains were reduced for beam running. It would have been preferable to calibrate the detectors using gamma energies closer to the energies produced in the experiment (20 - 40 MeV). However, this was not possible as no convenient sources were available in this energy range. A plot of the response of one of the NaI(Tl) detectors to the 4.43 MeV gamma rays from AmBe is shown in figure 3-5 for events in which the gammas are detected in the NaI(Tl) detector in coincidence with neutrons detected in the NE213 liquid scintillator. Three peaks are clearly identifiable at the upper end of the spectrum. The peaks correspond to the 4.43 MeV full energy

---

[1] One of the reaction chains from the bombardment of the beryllium by the α's from ^{214}Am is

$$\alpha +^9 Be \rightarrow^{13} C^* \rightarrow^{12} C^* + n$$

where photons populate the 4.43 MeV excited state of ^{12}C.

peak, and the first and second escape peaks, at 3.92 and 3.41 MeV, respectively.

3.4.2 Beam profile

A lateral scan of the beam, at the position of the vertex centre, was done with a small (10 mm diam. x 10 mm) organic scintillator to determine the profile of the neutron beam. The results of the scan are shown in figure 3-6 from which it can be seen that the intensity of the beam was uniform across the width of the NE213 cell.

3.4.3 Vertex calibrations

Singles NE213 runs, that is runs for which a coincidence was not required from an NaI(Tl) detector, were made using beam neutrons to set up and calibrate the NE213 detector. Figures 3-7, 3-8 and 3-9 show various spectra from such a run. The spectrum labelled "*All*" in figure 3-7 shows the neutron time-of-flight spectrum, without the T_n window, for the ^{7}Li(p,n)^{7}Be reaction for 66 MeV incident protons. All products from the reactions of neutrons on hydrogen and on carbon in the NE213 scintillator (figure 3-8) are included in this spectrum. The two main features are the strong peak corresponding to the neutron energy of 63.4 MeV from the ^{7}Li(p,n)^{7}Be (gs+0.43 MeV) transition, and the broad lower energy tail attributed to neutrons associated with higher excitations of ^{7}Be or from 3-body breakup reactions.

Figure 3-8 shows a perspective view of counts (vertical) against L and S for singles events from the same run with the T_n window imposed, and set to select the 63.4 MeV neutron peak in figure 3-7. Events in the NE213 due to n-p elastic scattering and the products of neutron reactions on carbon form ridges in the LS plane corresponding to protons (p), deuterons (d), and alpha (α) particles as indicated in the diagram [Bu90][Nc94]. The less prominent "escape" locus (ep) to the left of the proton ridge arises from the detection of charged particles, mainly protons, that escape at the edges of the scintillator. The pulse shape parameter S for these events is depressed to lower values because escape selectively removes the scintillation component arising from the excitation, for which the specific energy loss is a maximum i.e. the Bragg peak, which is responsible for the pulse shape discrimination effect [Br79]. There is no gamma locus

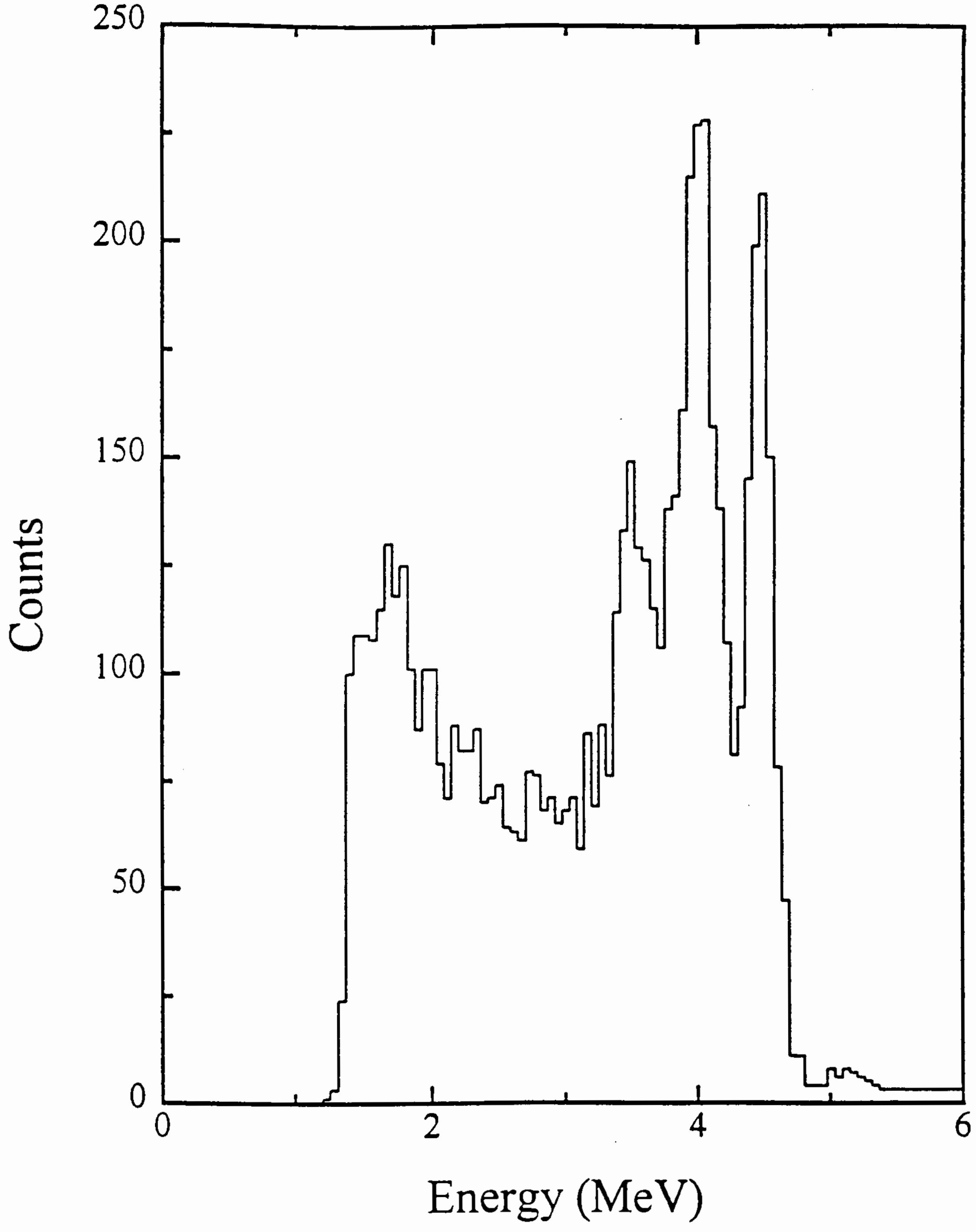

Figure 3-5: *Pulse height response of Na(Tl) to 4.43 MeV photons from an AmBe source. The spectrum shows events for which there is a coincidence with a neutron detected in the NE213 vertex detector. The three peaks correspond to 4.43 (full energy), 3.92 (first escape) and 3.41 MeV (double escape), respectively.*

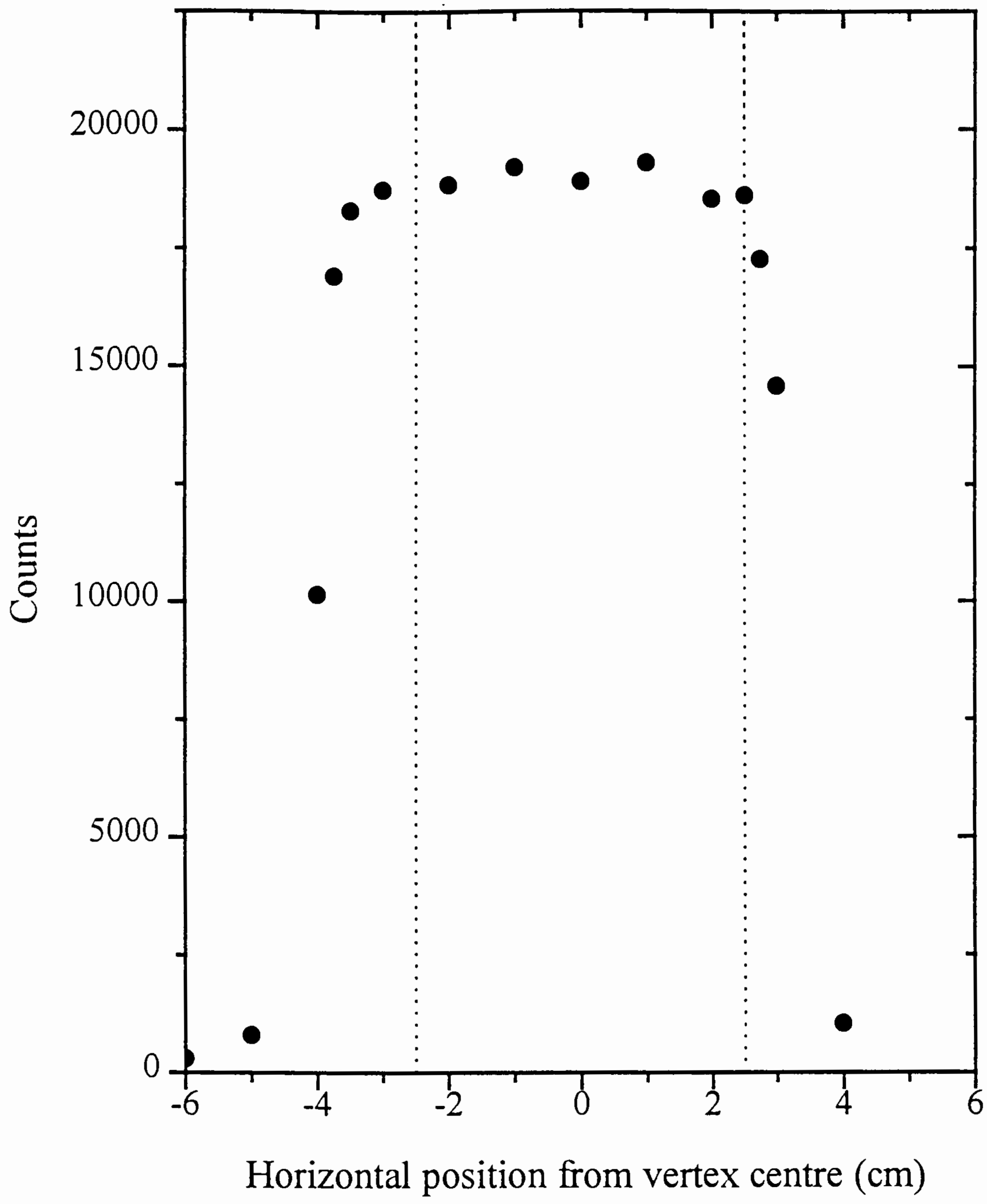

Figure 3-6: *Results of scanning a cylindrical organic crystal (10 mm diam. x 21 mm) horizontally across the neutron beam at the vertex position showing the counts measured for a fixed number of protons incident on the Li target as a function of position from the vertex. The dotted lines indicate the width and position of the NE213 cell relative to the neutron beam.*

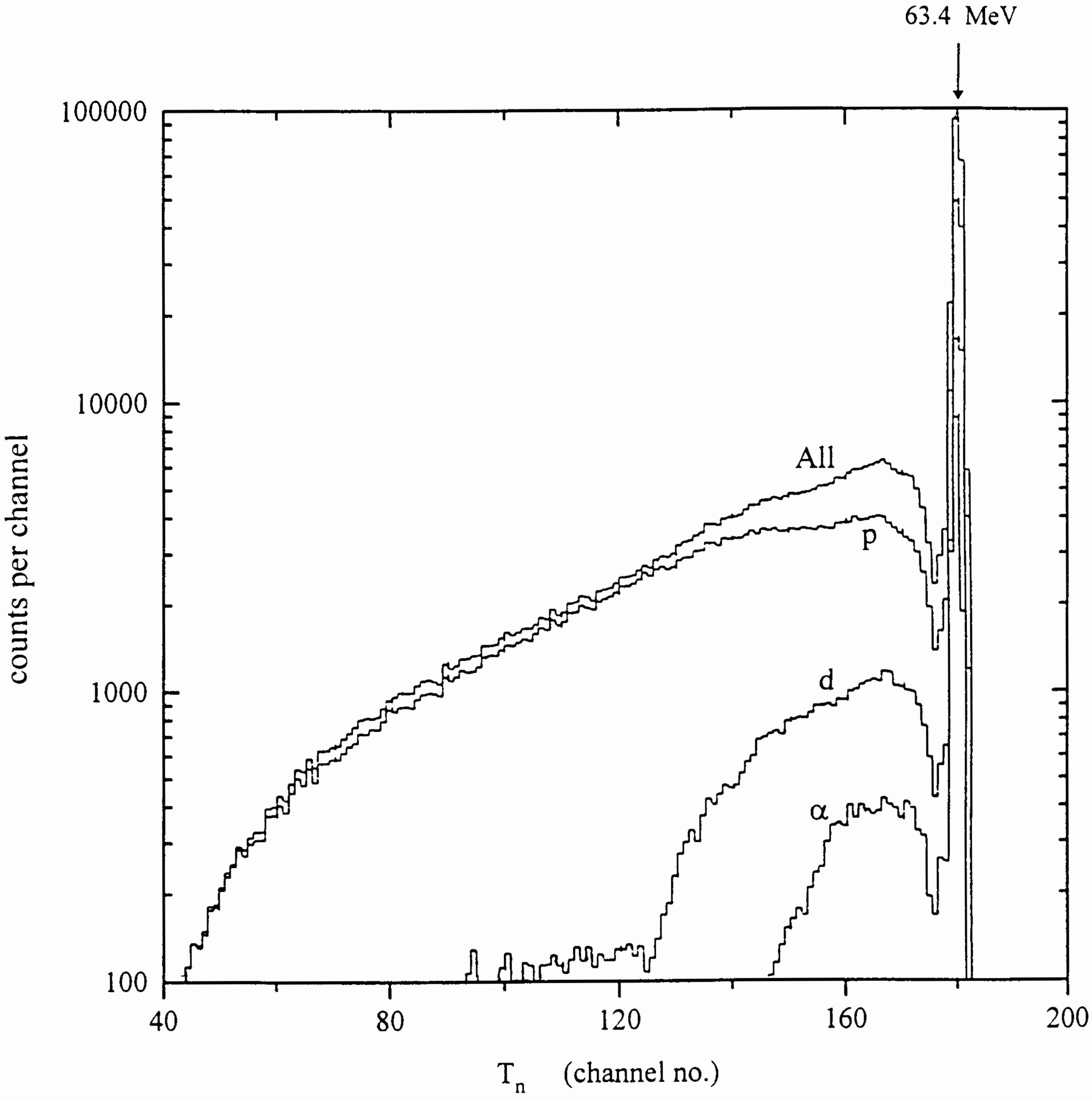

Figure 3-7: *Counts versus neutron time-of-flight for neutrons from 66 MeV protons incident on a thin lithium target. The curve labelled "All" is the spectrum for all events in the NE213 scintillator. The strong peak, centred around 63.4 MeV, corresponds to the (gs+0.43) MeV transitions in lithium. The spectra labelled p, d and α are the components identified by pulse shape discrimination as protons, deuterons and alphas .*

in figure 3-8 because the PSD facility of the LINK was used on-line to suppress the acquisition of Compton electrons from the gammas. The time-of-flight spectra labelled p, d and α in figure 3-7 were obtained by selecting events associated only with protons, deuterons and alphas, respectively. In each case the events were selected by placing an appropriate software window over the ridge of interest in the LS plane. The T_n window was "off" for these spectra, as for the "All" spectrum in figure 3-7.

Figure 3-9 shows counts (vertical) versus L and T_n for proton events selected by a software window bracketing the proton locus shown in figure 3-8. Prominent features in figure 3-9 are the strong ridge at the time-of-flight corresponding to 63.4 MeV neutrons and the recoil proton plateau associated with n-p elastic scattering from the continuous and weaker low energy distribution seen in the time-of-flight spectrum labelled p in figure 3-7. The bulge in the plateau at low L is attributed to ^{12}C(n,p)^{12}B and ^{12}C(n,px) reactions. The "cliff" at the edge of the plateau shows the locus of maximum proton recoil energy (i.e. forward recoils) as a function of incident neutron energy (time-of-flight). At low and mid-range values of L the intensity of the strong ridge (for 63.4 MeV neutrons) comprises contributions from both n-p elastic scattering and ^{12}C(n,p)^{12}B (gs). The drop in intensity at higher L indicates the edge corresponding to the maximum energy that is kinematically allowed for protons from the latter reaction.The further attentuation of the intensity at large L is attributed to protons from n-p elastic scattering that escape from the scintillator before depositing their full energy and therefore do not fall on the proton locus. A detailed study of the response of an NE213 cell, of the present dimensions, to neutrons from 14-63 MeV is contained in ref. [Bu90]

3.5 Radiative capture measurements

Radiative capture, $np \rightarrow d\gamma$, measurements were made by applying all the coincidence requirements in the electronic system (figure 3-4): that is the T_n and T_G windows, hardware PSD rejection of vertex gammas, the $G-$threshold and the $\overline{Busy}$ level from the data acquisition system. Three sets of coincidence measurements were made, each set comprising 60 to 80 hours beam time. Table 3.1 shows the six parameters recorded.

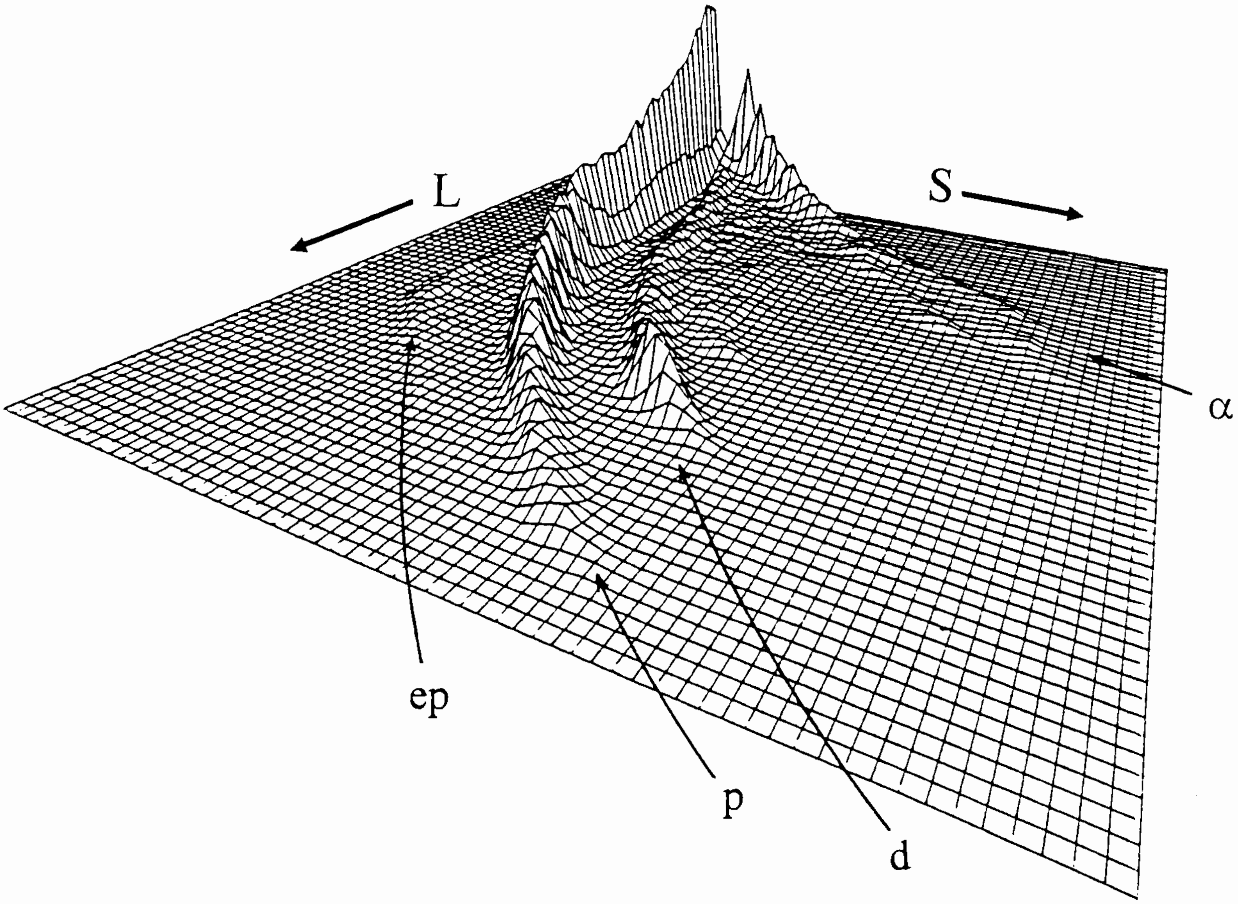

Figure 3-8: *Perspective view of number of events against pulse height L and pulse shape S for singles events from 63.4 MeV neutrons in the NE213 cell. The events in the NE213 form ridges which correspond to different particles as indicated: protons escaping from the scintillator (ep), protons (p), deuterons (d), and alphas (α)*

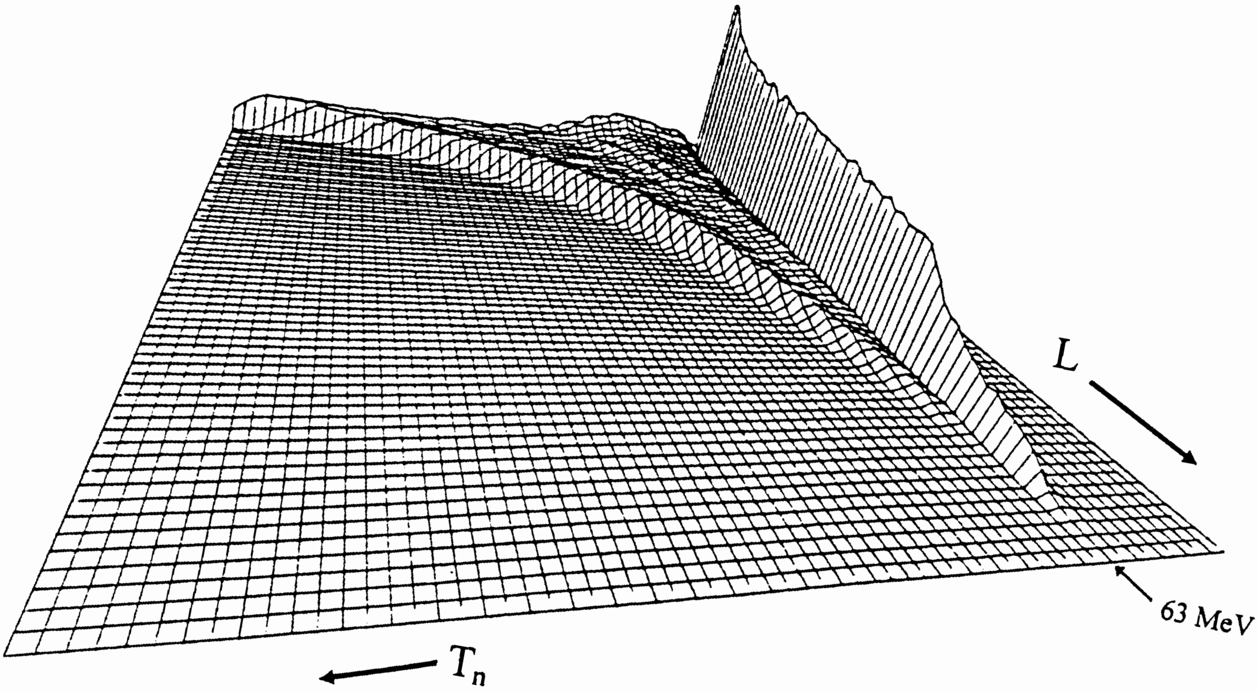

Figure 3-9: *Perspective view of counts (vertical) versus neutron time-of-flight* T_n *and NE213 pulse height L for events identified as protons by pulse shape discrimination. The ridge on the right corresponds to the strong forward peak of 63.4 MeV neutrons from the* $^7Li(p,n)$ *reaction at* $E_p = 66$ *MeV.*

Table 3.1: *Parameters recorded for radiative capture measurements.*

Parameter	Description
L	NE213 pulse height (long time integral)
F (S)	Pulse shape S derived from L and F (fast integral)
G	Na(Tl) pulse height
T_G	Coincidence time delay between NE213 and Na(Tl)
T_n	Neutron time-of-flight
R	Pattern register for identifying i^{th} Na(Tl)

Individual runs within each set of measurements were typically between 6 and 12 hours long. The peak neutron time-of-flight peak was monitored continuously on a multichannel analyser during the runs and adjustments were made to the timing of the "stop" pulse of the T_G TAC to compensate for any drifts that occurred. The singles event rate in the LINK was determined both by the beam current and the threshold set by the LINK discriminator. With the threshold set at about 0.5 MeV during these runs the singles rate in the LINK was about 3 kHz which was sufficiently low to avoid pile-up.

3.6 Off-line analysis

The data from the coincidence runs were replayed off-line and analysed event by event. The 2-parameter cut that was set up in the "singles LS" spectrum to select deuterons (figure 3-8) was used to filter the data, and only events falling within this window were accepted for further analysis. Using this subset of the data the information from the pattern register R was used to separate out events associated with each of the gamma detectors in turn. Events in which more than one gamma detector fired were rejected. A distribution of number of events against the coincidence time between the vertex and the i^{th} sodium iodide detector (T_G), and the pulse height in the i^{th} sodium iodide (G_i) was formed for each of the eight detectors. Figures 3-10 and 3-11 show some of these T_G versus G density plots obtained at each of the eight laboratory angles $\theta^{lab}_{n,\gamma}$.

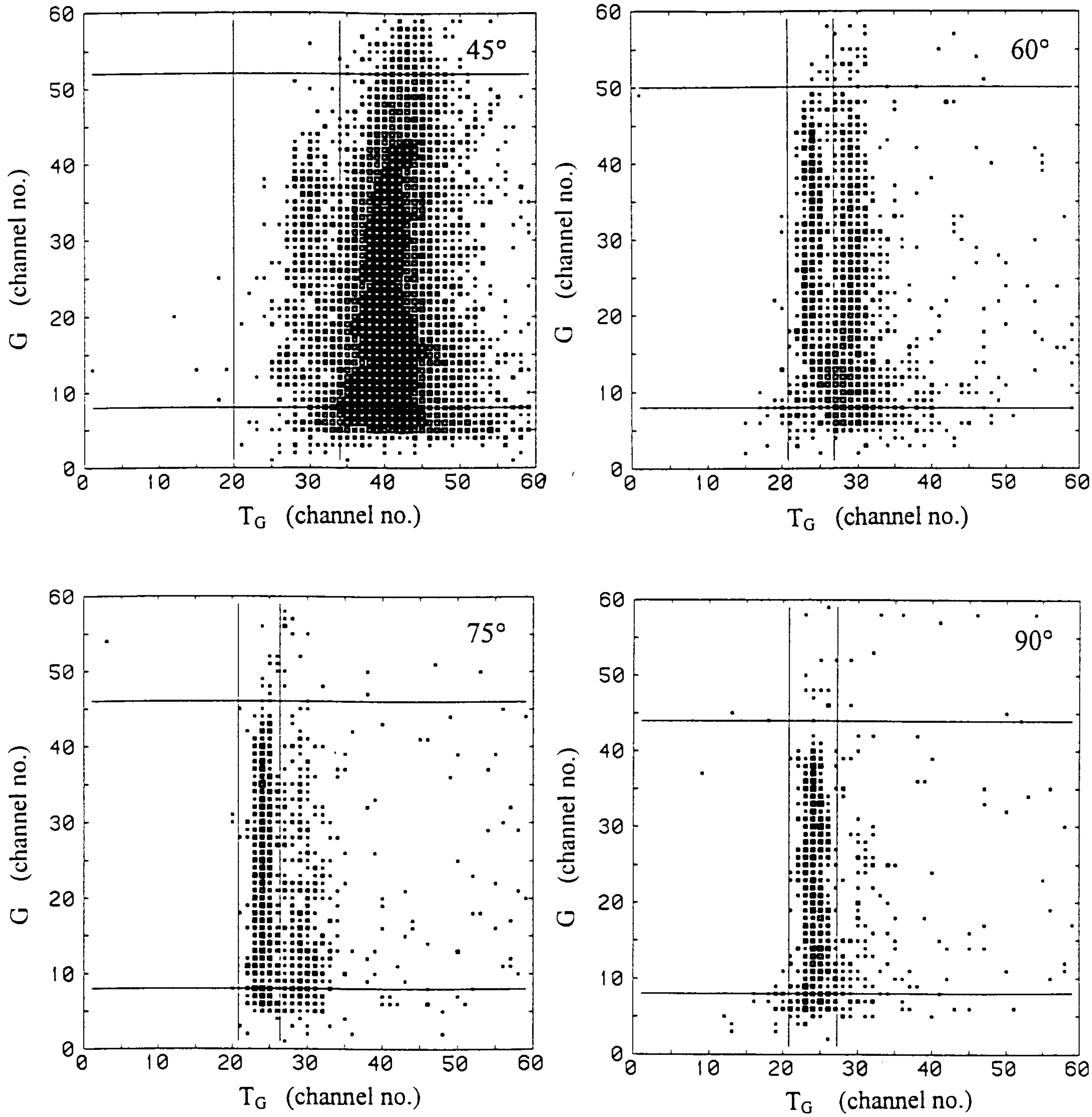

Figure 3-10: *Density plots of number of events against T_G, the time of flight between the vertex detector and the i^{th} Na(Tl) detector, and G the pulse height in the i^{th} Na(Tl) detector for* $= \theta^{lab}_{n,\gamma} = 45^\circ$, 60°, 75° *and* 90°. *Successively increasing block sizes correspond to event densities* $\geq$ *1,2 ,5, 10 and 20, respectively. The solid lines indicate the G and* T_G *cuts referred to in the text.*

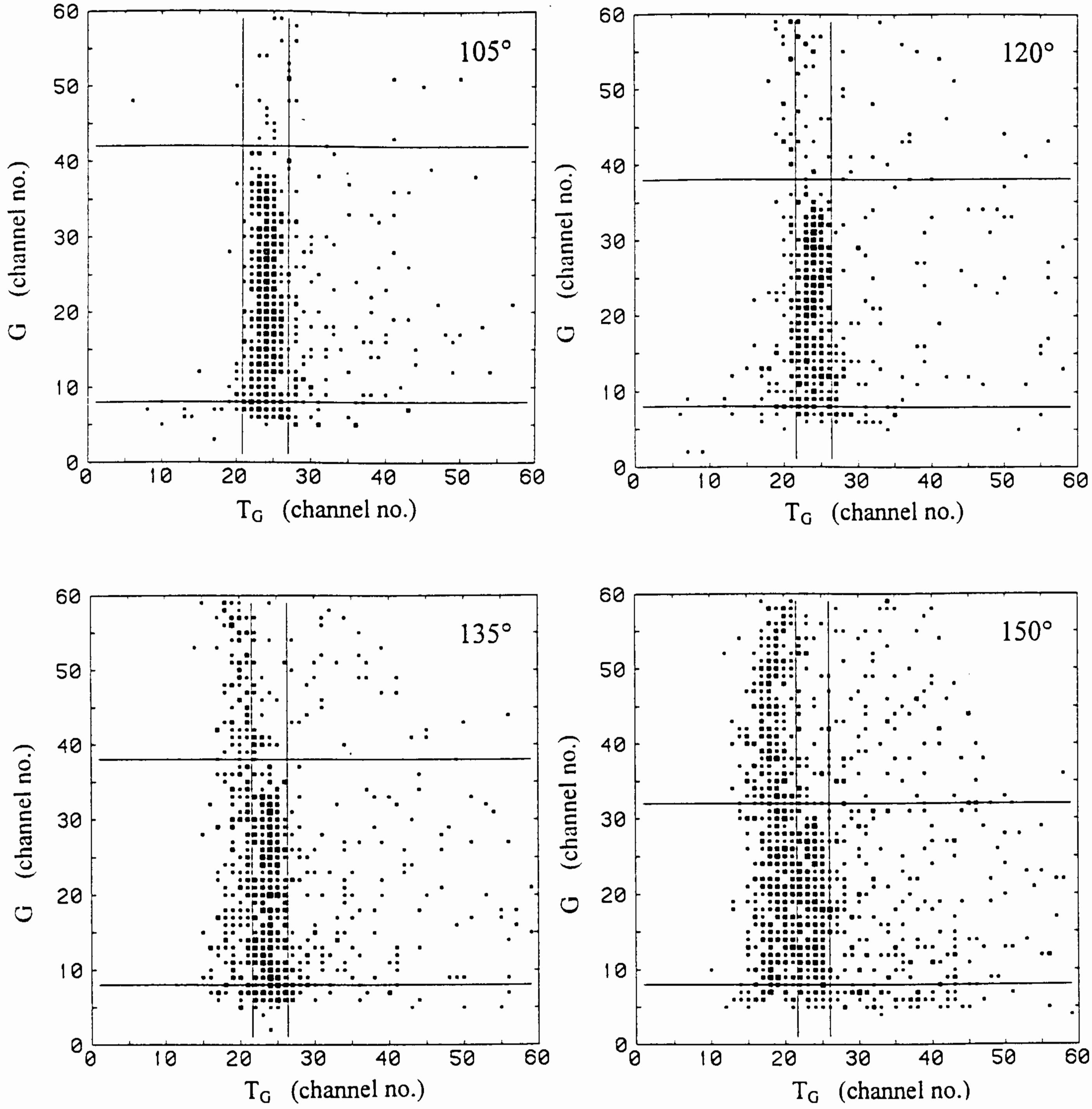

Figure 3-11: *Density plots of number of events against* T_G*, the time of flight between the vertex detector and the* i^{th} *Na(Tl) detector, and* G *the pulse height in the* i^{th} *Na(Tl) detector for =* $\theta^{lab}_{n,\gamma}$ *= 105°, 120°, 135° and 150° Successively increasing block sizes correspond to event densities* $\geq$ *1,2 ,5, 10 and 20, respectively. The solid lines indicate the* G *and* T_G *cuts referred to in the text.*

Events due to three possible processes may be identified on these plots. Firstly, the events that are associated with n-p capture are located within the rectangular window formed by the cuts indicated on the T_G and G axes. The capture events are most clearly seen at 90° (figure 3-10) where the background due to the other processes is minimal. The second process involves a coincidence caused by a neutron scattering from the vertex into the sodium iodide. Since the time of flight of the neutron between the detectors is longer than that of a gamma these events fall to the right of the corridor, along the T_G axis, corresponding to the $np \rightarrow d\gamma$ events. Because the neutron scattering is forward peaked this process becomes more likely as the angle between the sodium iodide and the neutron beam becomes smaller, as can be seen by comparing the plots in figure 3-10, and this imposes a limiting factor on measuring the capture cross section at the more forward angles. At $\theta^{lab}_{n,\gamma} = 45°$, for example, it can be seen that the background is substantially higher than at 60°. The third process is attributed to coincidences from neutrons which are detected in the vertex *after* inelastic scattering in a sodium iodide detector, the detection in the latter being via gammas excited by the inelastic scattering. Along the T_G axis these events fall to the left of the corridor of $np \rightarrow d\gamma$ events in figures 3-10 and 3-11, and they are more likely for sodium iodide detectors at angles greater than 90°. This can be seen in figure 3-11 for $\theta^{lab}_{n,\gamma} = 150°$ where such events are at a maximum.

The background associated with low G pulses was reduced by applying a threshold to the G parameter. A cut at a fixed pulse height was used, as indicated by the horizontal line just below channel 10, on the G axis in figures 3-10 and 3-11. The energy thresholds corresponding to this cut at each detector angle are listed in table 3.2.

Table 3.2: *Energy threshold applied off-line for each detector.*

$\theta^{lab}_{n,\gamma}$ (deg)	45.0	60.0	75.0	90.0	105.0	120.0	135.0	150.0
E_{thr} (MeV)	15.5	11.9	12.5	13.1	13.1	12.5	12.5	16.3

The data satisfying the G and T_G cuts shown in figures 3-10 and 3-11 were selected to form LS spectra at each $\theta^{lab}_{n,\gamma}$ angle. Figure 3-12 shows a perspective view of the number of events against L and S for $\theta^{lab}_{n,\gamma} = 90°$ while figures 3-13 and 3-14 show event density plots of L against S at each angle.

The deuterons resulting from n-p radiative capture are clearly identified by the sharp peaks on the deuteron locus at each angle. Events on the deuteron ridge in each of the eight spectra were selected by applying the cuts indicated by the solid, curved lines on the LS plots. The vertical lines on these plots indicate the L cuts applied to the data.

Figures 3-15, 3-16 and 3-17 show projected spectra for T_G, G, and L respectively, after the various cuts described have been applied to the data. Figure 3-15 shows the projected T_G spectra with the L, LS, and G cuts applied. At angles where the capture events are clearly separated from the backround, e.g. at 75° and 90°, the capture events form distinct peaks centred around channel 30. The backgrounds from the two processes discussed above are also apparent at the various angles. Figure 3-16 shows projected G spectra with L, LS, and T_G cuts applied. It can be seen that the edges of the spectra, corresponding to maximum energy, shift with angle as expected from the kinematics. Figure 3-17 shows the associated deuteron pulse height spectra obtained by projecting the data onto the L axis after applying the LS, T_G and G cuts. The peaks corresponding to n-p capture stand out clearly and display the expected kinematic shift with detection angle. It can also be seen that the peaks shift in the opposite direction to the maximum energy edges of the G spectra as the angle $\theta_{n,\gamma}^{lab}$ changes, which is consistent with the kinematics of the $np \rightarrow d\gamma$ reaction in which the deuteron and the capture gamma ray move away from each other at 180° in the centre of mass frame (see Appendix A).

The capture peaks were integrated to yield the number of events from radiative capture N_c at each angle of detection. Background levels were estimated by linear interpolation between the regions on either side of the peaks. Table 3.3 lists the integrals and the statistical accuracy of the measurements. In table 3.3, N_c is the integral under the deuteron peak after subtracting the background and $\Delta\mathrm{N}_c$ is the statistical uncertainty. The last column shows the fractional statistical accuracy of the measurement.

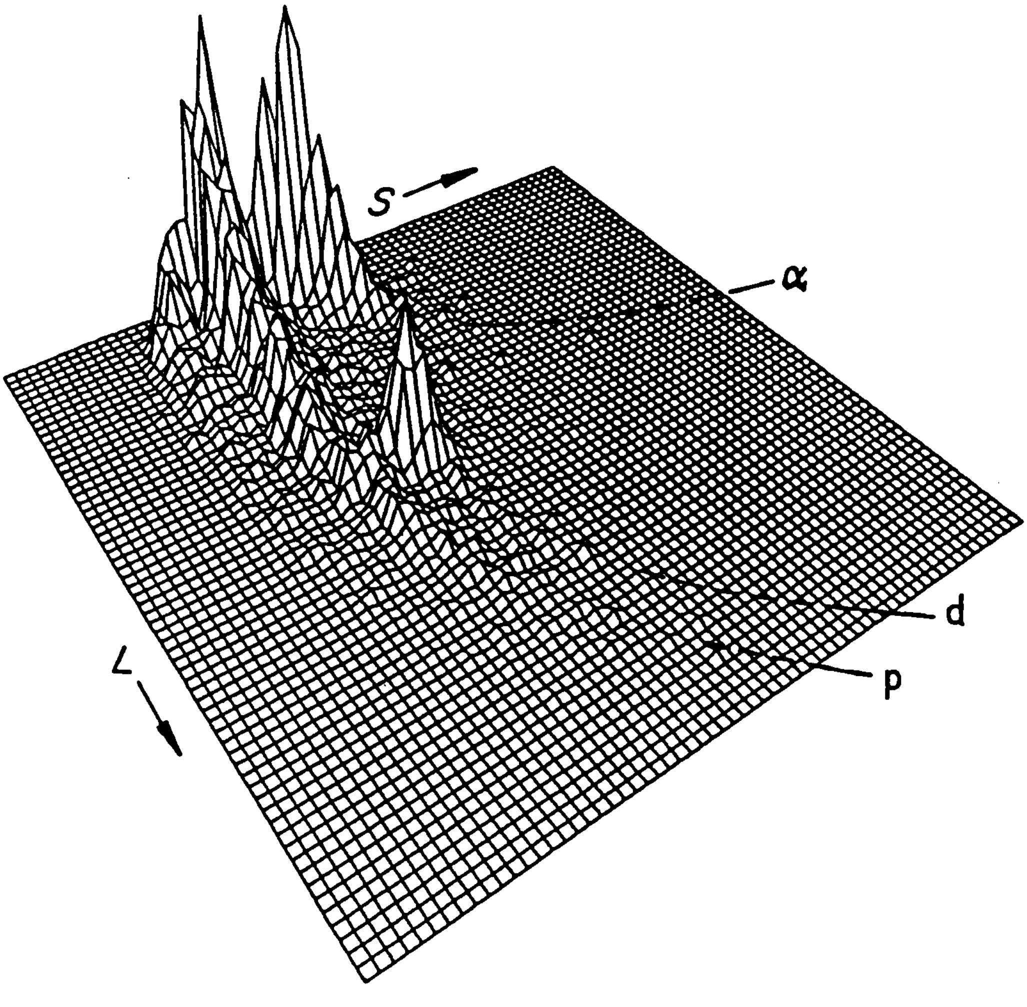

Figure 3-12: *Perspective view of counts (vertical) as a function of pulse height L and pulse shape S at* $\theta^{lab}_{n,\gamma} = 90^\circ$ *after applying the cuts to the* T_G *and the G parameters as described in the text. The deuteron peak associated with capture events stands out clearly on the deuteron locus.*

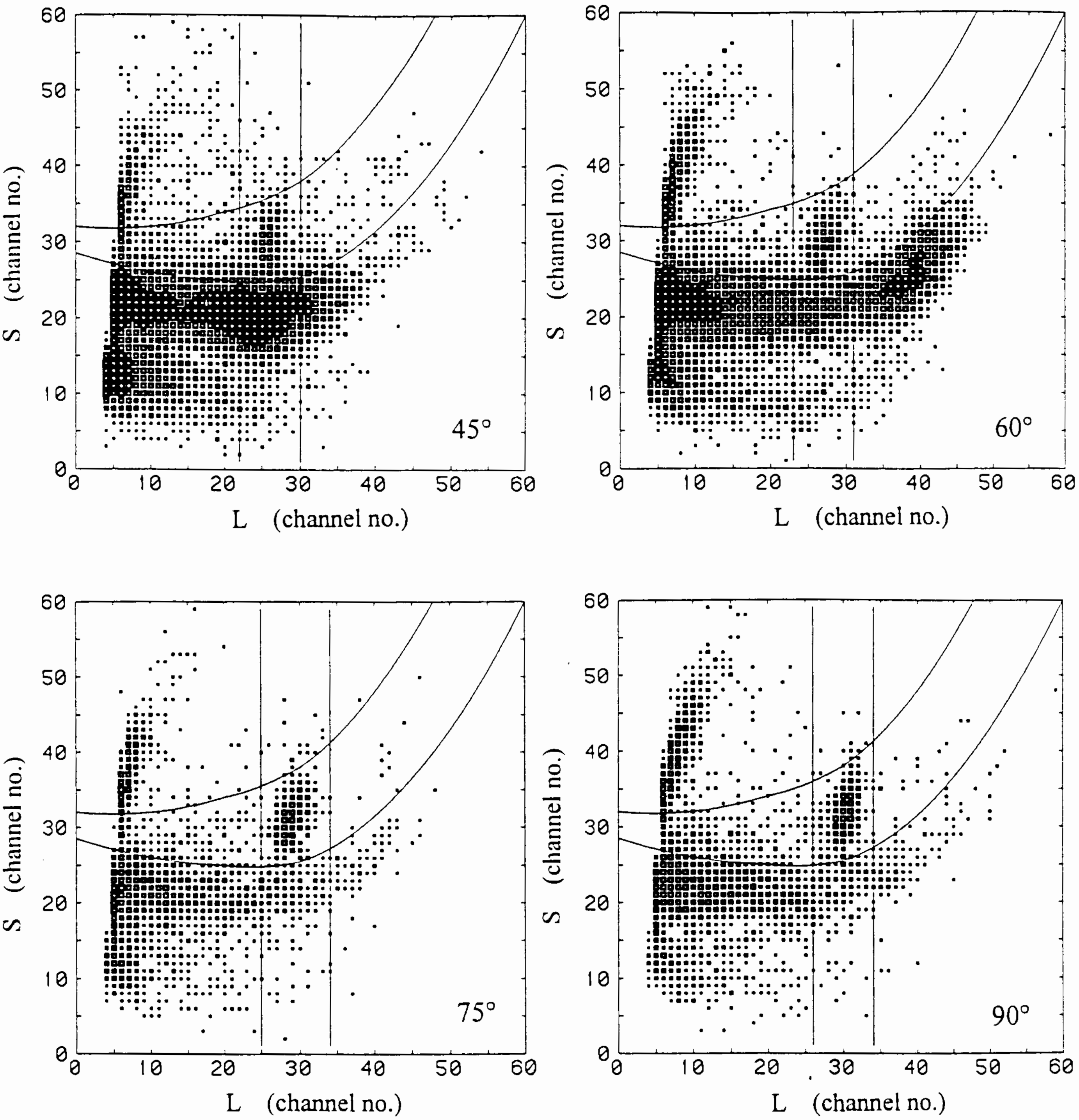

Figure 3-13: *Density plots of pulse height L against pulse shape S for* $\theta^{lab}_{n,\gamma} = 45°, 60°, 75°$ *and* $90°$, *with cuts applied to the* T_G *and the G parameters as described in the text. The peaks corresponding to n-p capture stand out clearly on the deuteron locus. The solid lines indicate the L and LS cuts referred to in the text. Successively increasing block sizes correspond to event densities* $\geq$ *2, 5, 10, 20 and 50, respectively.*

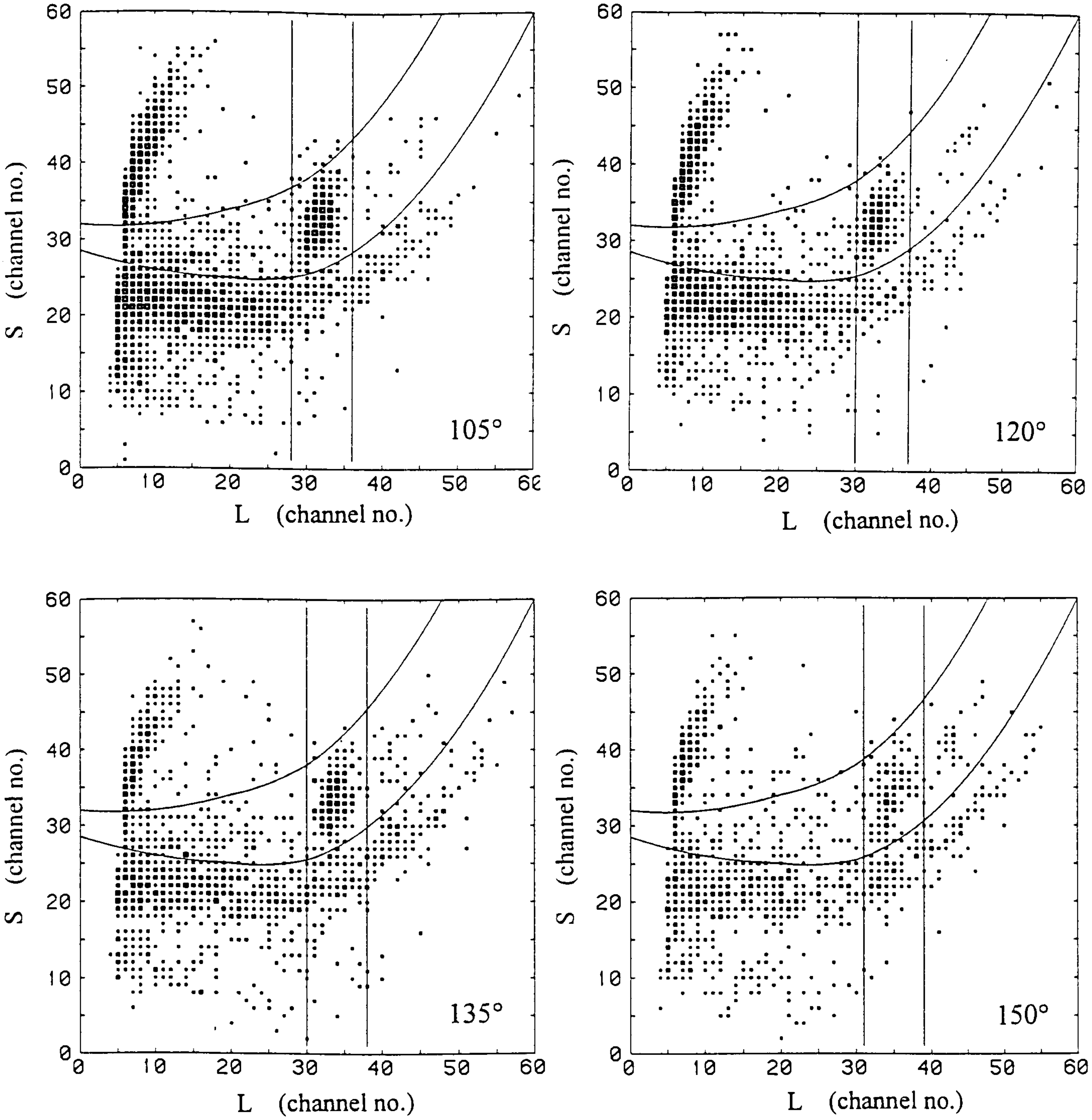

Figure 3-14: *Density plots of pulse height L against pulse shape S for* $\theta^{lab}_{n,\gamma}$ *= 105°, 120°, 135° and 150°, with cuts applied to the* T_G *and the G parameters as described in the text. The peaks corresponding to n-p capture stand out clearly on the deuteron locus. The solid lines indicate the L and LS cuts referred to in the text. Successively increasing block sizes correspond to event densities* ≥ 2*, 5, 10, 20 and 50, respectively.*

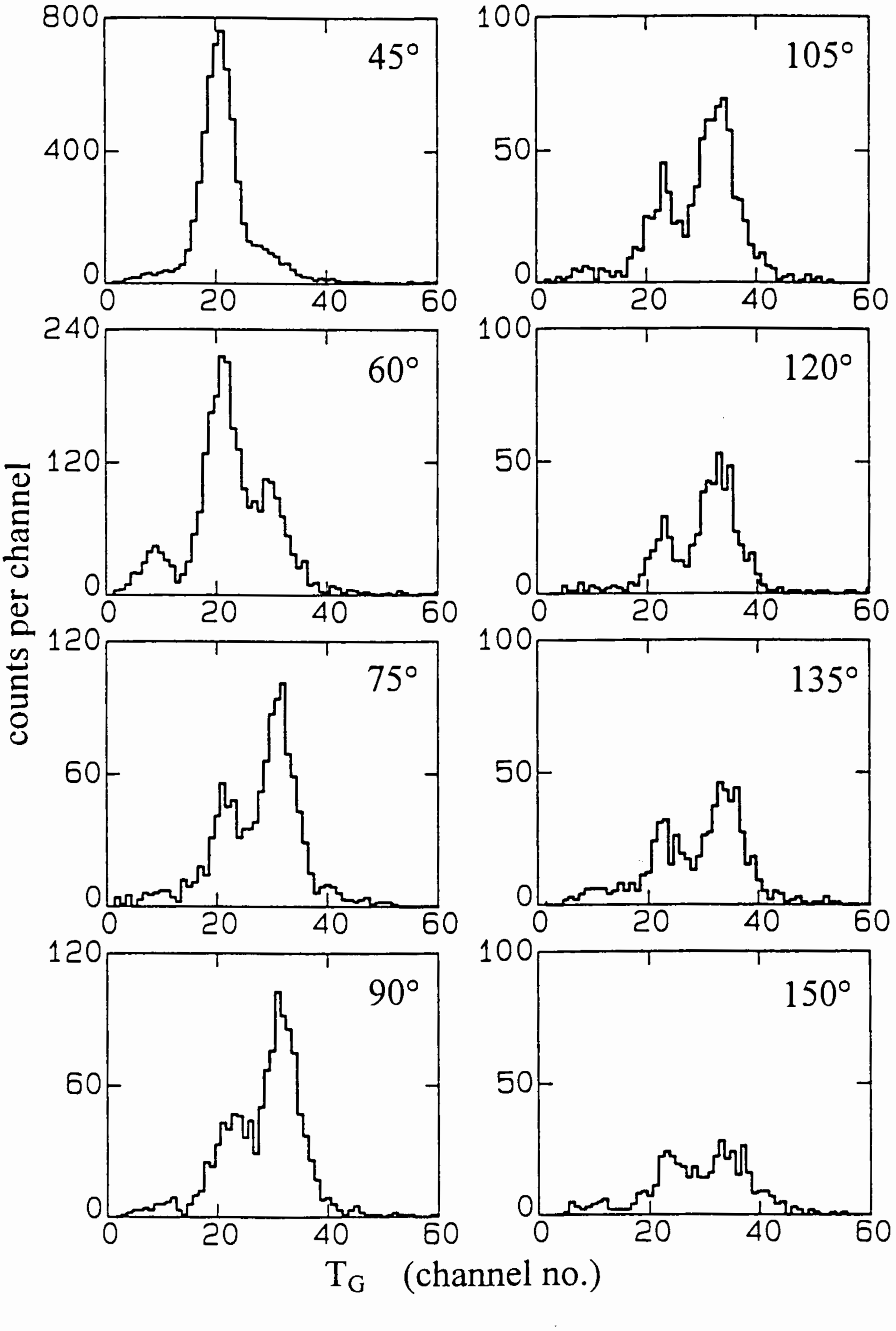

Figure 3-15: *Projected* T_G *spectra at each angle* $\theta^{lab}_{n,\gamma}$, *with L, LS, and G cuts applied.*

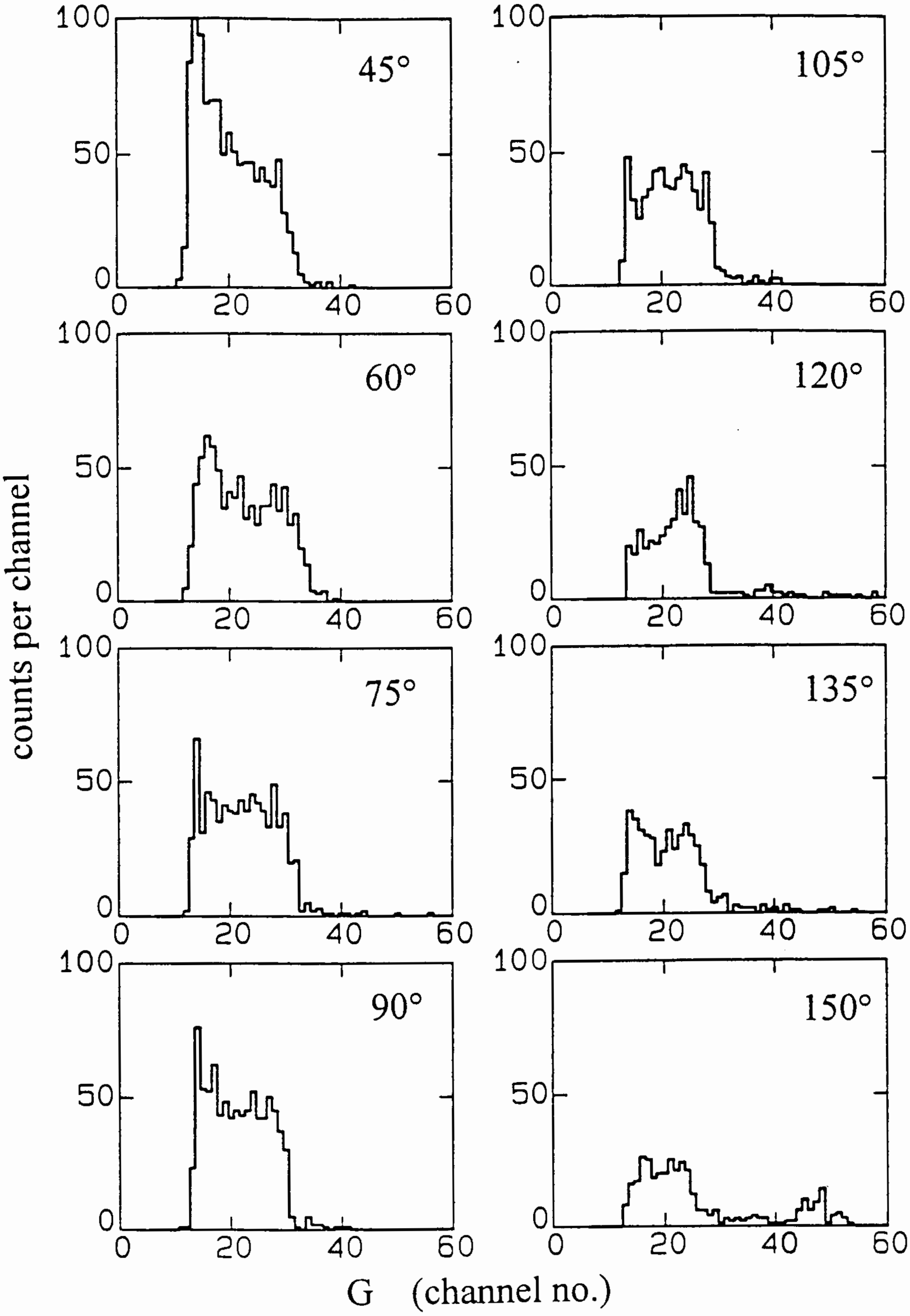

Figure 3-16: *Projected G spectra at each angle* $\theta_{n,\gamma}^{lab}$, *with L, LS, and* T_G *cuts applied.*

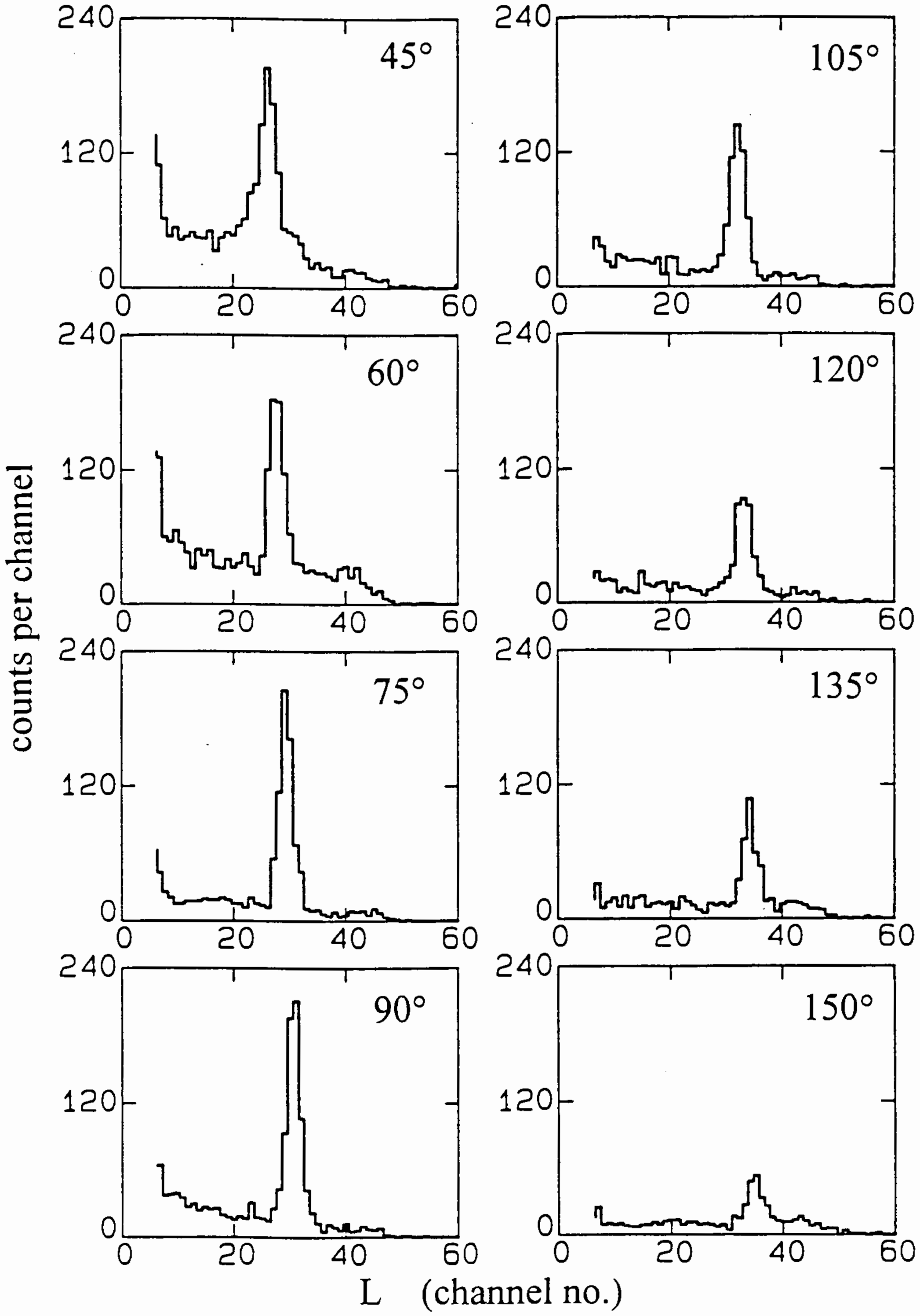

Figure 3-17: *Projected L spectra at each angle* $\theta^{lab}_{n,\gamma}$*, with LS,* T_G*, and G cuts applied.*

Table 3.3: *Integrals from n-p capture peaks. See the text for the nomenclature.*

$\theta^{lab}_{n,\gamma}$ (deg .)	N_c	ΔN_c	$\frac{\Delta N_c}{N_c}$
45.0	426	34	0.08
60.0	498	30	0.06
75.0	578	27	0.05
90.0	612	29	0.05
105.0	470	26	0.06
120.0	330	21	0.06
135.0	244	21	0.09
150.0	110	18	0.16

Chapter 4

The differential cross sections

The differential cross sections for n-p capture in the laboratory frame $\left(\frac{d\sigma(\theta^{lab}_{n,\gamma})}{d\Omega}\right)_{cap}$ can be calculated from the integrals N_c in table 3.3 after a number of corrections are applied to the integrals at each angle of detection. These corrections are related to the solid angle of detection, the efficiency of the NaI(Tl) detector, and the fraction of deuterons that are detected. The relationship between $\left(\frac{d\sigma(\theta^{lab}_{n,\gamma})}{d\Omega}\right)_{cap}$ and N_c is expressed as follows

$$\left(\frac{d\sigma(\theta^{lab}_{n,\gamma})}{d\Omega}\right)_{cap} \propto \frac{N_c}{f_d\ \Omega\ \varepsilon} \tag{4.1}$$

where $f_d(\theta^{lab}_{n,\gamma})$ is the fraction of deuterons that were detected in the NE213 liquid scintillator after correcting for multiple scattering, $\Omega(\theta^{lab}_{n,\gamma})$ is the *effective* solid angle subtended by the sodium iodide detector after taking in-scattering of conversion electrons into account, and $\varepsilon(E^{lab}_{\gamma})$ is the efficiency of the sodium iodide detector. The differential cross sections for n-p capture in the centre-of-mass frame are related to the cross sections in the centre-of-mass by a set of transformation factors $J(\theta)$ which are described in section 4.1.3 below.

4.1 Corrections and transformations

4.1.1 Multiple scattering and deuteron escapes

A fraction of the events in the deuteron peaks are due to captures which have occurred after the neutron has scattered on a C or H nucleus in the NE213 before it is captured. A Monte-Carlo calculation, using the program described in ref. [He91], was performed in which this effect was investigated. The contribution to the capture peaks from these multiple scattering events was shown to vary from 2% to 3% as $\theta_{n,\gamma}^{lab}$ varied from 150° to 45°.

Because of the finite size of the NE213 detector (50mm diam. x 50mm) a fraction of the recoiling deuterons will escape from the cell without depositing their full energy, and will therefore not appear on the deuteron locus. The fraction of capture events that go undetected in this way depends on the range of the deuteron relative to the dimensions of the NE213 cell. Since the deuterons are emitted in the NE213 cell with energies varying approximately between 25 and 40 MeV (figure A.2), they will have a corresponding range between 4.1 and 9.5 mm. The Monte-Carlo program was also used to calculate the fraction of capture events that were lost due to the finite size effect of the detector. Table 4.1 shows the fraction of deuterons f_d that *are* detected within the volume of the NE213 cell at each angle, $\theta_{n,\gamma}^{lab}$ after correcting for multiple scattering. The detected fraction f_d varies with angle as expected from the kinematics of the $np \rightarrow d\gamma$ reaction (Appendix A). From the values calculated for f_d at $\theta_{n,\gamma}^{lab}$ = 45° and 150°, it is seen that the variation in f_d is $\leq 10\%$ over the whole range of the measurements.

Table 4.1: *Fraction of deuterons that are detected within the volume of the NE213 cell at each $\theta_{n,\gamma}^{lab}$ angle.*

$\theta_{n,\gamma}^{lab}$ (deg)	45.0	60.0	75.0	90.0	105.0	120.0	135.0	150.0
f_d	.89	.88	.87	.86	.84	.83	.82	.81

4.1.2 Efficiency calculations for the Na(Tl) detectors

Introduction

Sodium iodide is widely used in gamma ray detection and there are a number of papers dealing with efficiency calculations as indicated, for example, in the review article by Heath et al. [He79]. However, a number of these calculations are for energies below 20 MeV e.g. refs. [Be72][Ja62][Gr76], and the analytical methods and approximations which are used are not valid at higher energies where radiation losses by electron and positron bremsstrahlung are important. In the case of the present work the photon energy that is detected varies between 28 and 38 MeV owing to kinematic effects. Table 4.2 shows the photon energy $E_\gamma^{lab}(\theta_{n,\gamma}^{lab})$ detected at each angle as a function of laboratory angle $\theta_{n,\gamma}^{lab}$. (See Appendix A.)

Table 4.2: *Photon laboratory energy as a function of laboratory angle.*

$\theta_{n,\gamma}^{lab}$ (deg)	150.0	135.0	120.0	105.0	90.0	75.0	60.0	45.0
$E_\gamma^{lab}(\theta_{n,\gamma}^{lab})$ MeV	28.4	29.0	30.0	31.3	32.8	34.4	36.0	37.6

There are also calculations in which it is assumed that that energy losses through the sides of the crystal may be ignored e.g. [Be72]. This assumption is, however, not valid in the present case since losses through the sides of the crystals are significant owing to the geometry. The Monte Carlo program ESTE [Co81][Ta83][Zu88], in which all the electromagnetic processes are taken into account and the finite size of the crystals is modelled, was chosen to calculate the efficiencies of the detectors. A brief description of the important interactions involved in detecting photons with Na(Tl) is given below. The discussion is based on refs. [Kn89][Le87][Da70].

Interaction of photons with Na(Tl)

Photons interact with matter via the photoelectric effect, Compton scattering or pair production, producing secondary electrons, or electrons and positrons, which then lose their energy by collisions or by bremsstrahlung. The cross section for each of these processes depends on the energy of the photon as well as on the material, in this case

Na(Tl), as indicated in figure 4-1.

An overall indication of how strongly photons interact is given by the attenuation coefficient μ. For example, at 30 MeV the attentuation coefficent μ is 0.05 cm^2 g^{-1} (or 0.18 cm^{-1}) which is equivalent to a 90% probability of interaction of a parallel beam in a 12.7 cm crystal, the length of the crystals used in this work. At energies above 20 MeV the photoelectric contribution is negligible while the ratio of pair production to Compton scattering increases rapidly as indicated in table 4.3 where four photon energies in the range of interest to this work are listed.

Table 4.3: *Ratio of pair production to Compton scattering for photons interacting with Na(Tl) for various photon energies.*

Photon energy (MeV)	10	20	30	40
Pair to Compton ratio	1.7	4.8	6.7	11.0

At 17.4 MeV, the so-called critical energy, both collision-ionisation and bremsstrahlung are equally important and $(\frac{dE}{dx})_{coll} = (\frac{dE}{dx})_{brem}$. Above this energy bremsstrahlung becomes the more important energy loss mechanism. The dominance of pair production which leads to electron-positron showers implies that, in calculating the efficiencies by computer modelling, electrons and positrons have to tracked until they either escape from the crystal or have fully radiated their energy within the crystal.

The way in which each of the processes mentioned is taken into account in the Monte Carlo programme ESTE is described in detail in refs. [Co81][Ta83][Zu88]. In particular, however, full tracking of electron and positron trajectories as well as energy loss through radiation in the form of bremsstrahlung were incorporated into the program. The program also allowed the effects of the lead shield surrounding each detector and the thin lead plate in front of each detector to be included in the calculations.

Lineshapes and solid angle and efficiency factors

The Monte Carlo program ESTE was used to compute the lineshapes for the Na(Tl) detectors including the effects of the lead shielding by simulating the response to monoenergetic photons at the energies indicated in table 4.2. Fig. 4-2 shows plots of these

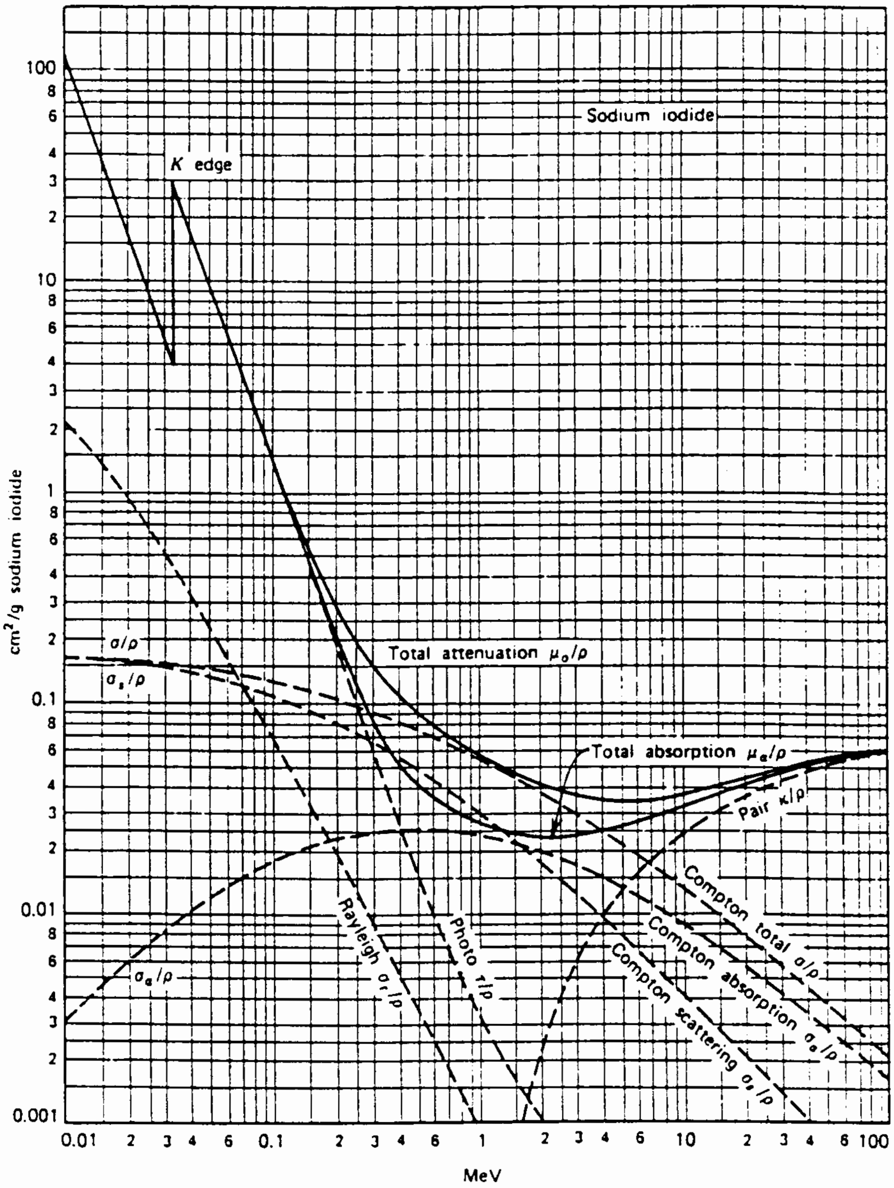

Figure 4-1: *Mass attenuation coefficients for Na(Tl) showing the energy dependence of the gamma ray interactions. Figure from [Kn89].*

lineshapes, all of which exhibit similar features. The largely flat shapes are attributed to the fact that the shape is largely determined by electrons from the high energy showers escaping though the sides of the detector. As the photon energy $E_\gamma^{lab}(\theta_{n,\gamma}^{lab})$ increases, the high energy edges of the spectra shift to the right as expected. The efficiency of each detector at a given threshold energy is proportional to the fraction of the area under the curve and between the limits of the energy set by the threshold and the photon energy.

Owing to the in-scattering of electrons from the lead shields, the effective solid angle of acceptance is larger than the geometrical angle subtended by the detector. ESTE was used to calculate both the effective solid angle and the efficiency as a function of threshold energy E_{thr}. The product of the effective solid angle Ω and the efficiency ε was combined into a single factor $(\Omega\varepsilon)$. Plots of $\Omega\varepsilon$ as a function of E_{thr} are shown in figure 4-3.

A number of checks were carried out in order to study the effect on the $\Omega\varepsilon$ factors of varying the source to detector distance, the thickness of the shield and the size of the source. The effect on the $\Omega\varepsilon$ factors for the energy thresholds used during the analysis i.e. the range 12-16 MeV, was also investigated. The size of the extended source was found to have no measurable effect on the $\Omega\varepsilon$ factors above a threshold energy of 10 MeV compared with using a point source, while the effect of reducing the thickness of the lead shield by a factor of up to four was also shown to be negligible between 12 and 16 MeV. Figure 4-4 shows the effect of changing the distance from the source to the detector from the value of 22.5 cm, measured in the experiment. It can be seen that a change of about 10% affects the $\Omega\varepsilon$ factor by about 25% at 10 MeV. The systematic error due to the measurement in the source to detector distance was estimated to be less than 2% which leads to an uncertainty in the $\Omega\varepsilon$ factors of within 5% between 12 and 16 MeV. Table 4.4 lists the $\Omega\varepsilon$ factors as a function of detection angle, $\theta_{n,\gamma}^{lab}$.

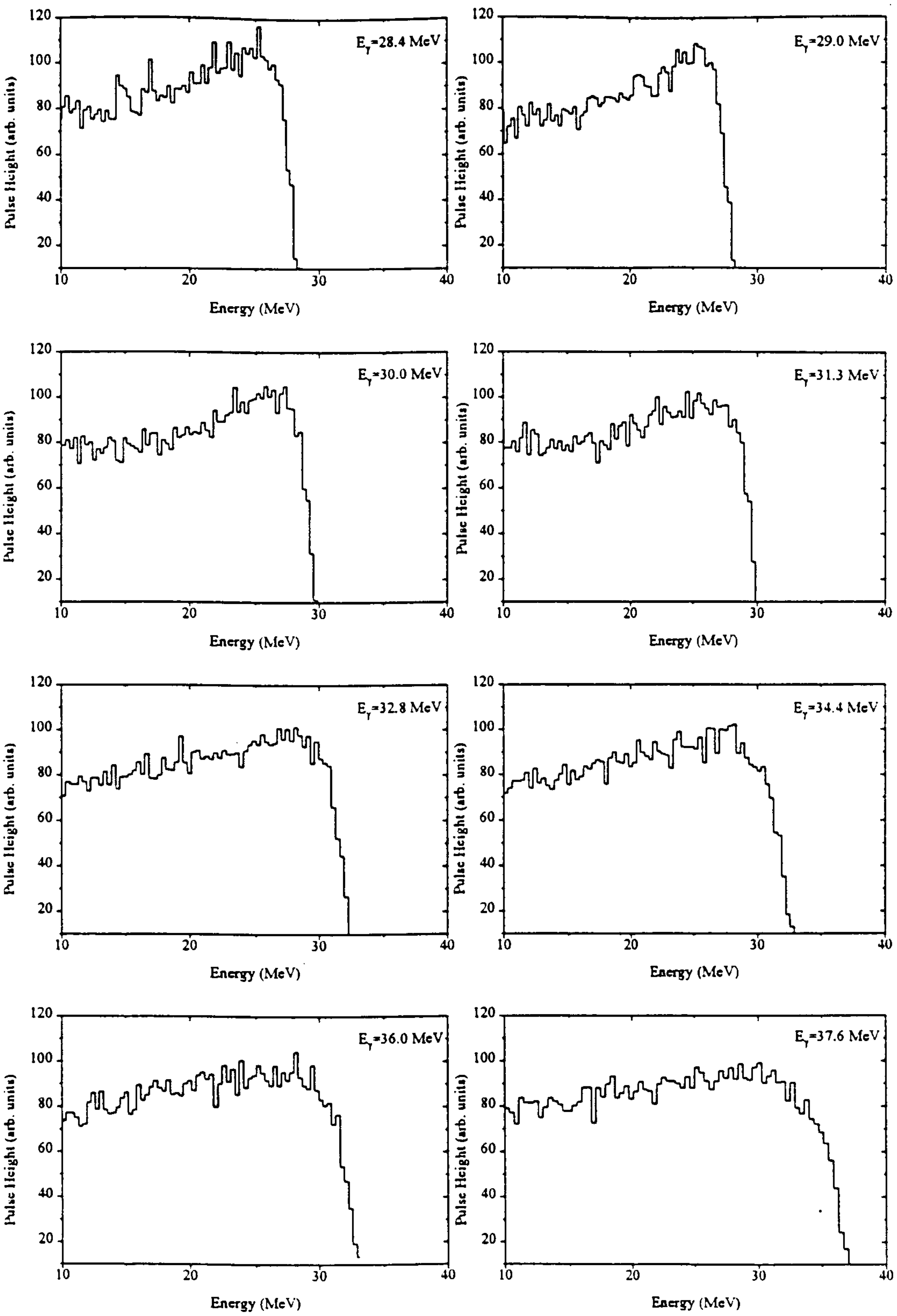

Figure 4-2: *Calculated lineshapes of the Na(Tl) detectors (75 mm diam. × 125 mm) to photons for the eight gamma energies of interest. The lineshapes were calculated for the configuration in which the NaI(Tl) crystals were surrounded by a lead shield 280 mm thick and the entrance face was covered by a thin (4.5 mm) lead plate.*

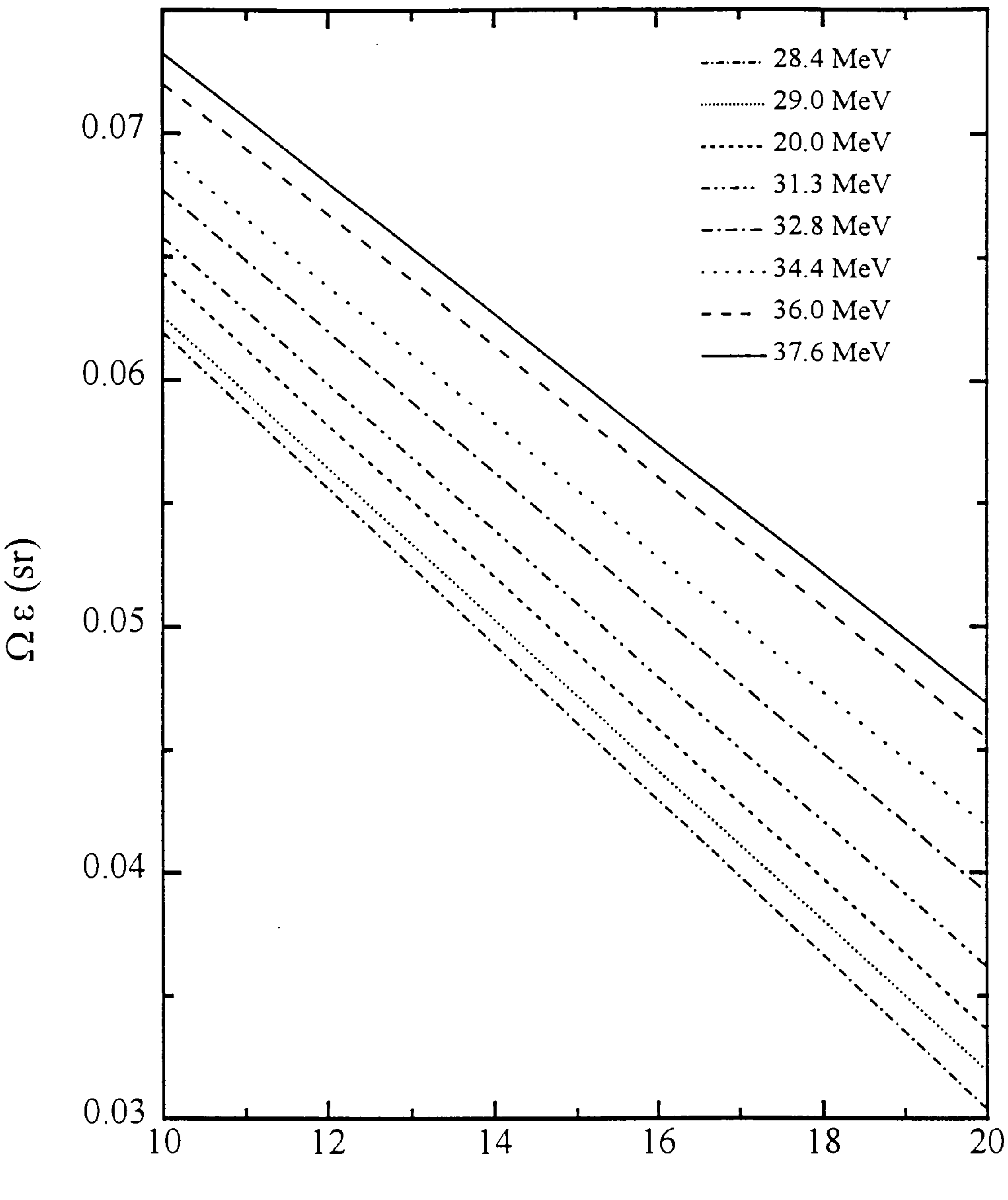

Figure 4-3: *The product of the solid angle and the efficiency (Ωε) as a function of the energy threshold from 12 to 16 MeV, at each angle of detection.*

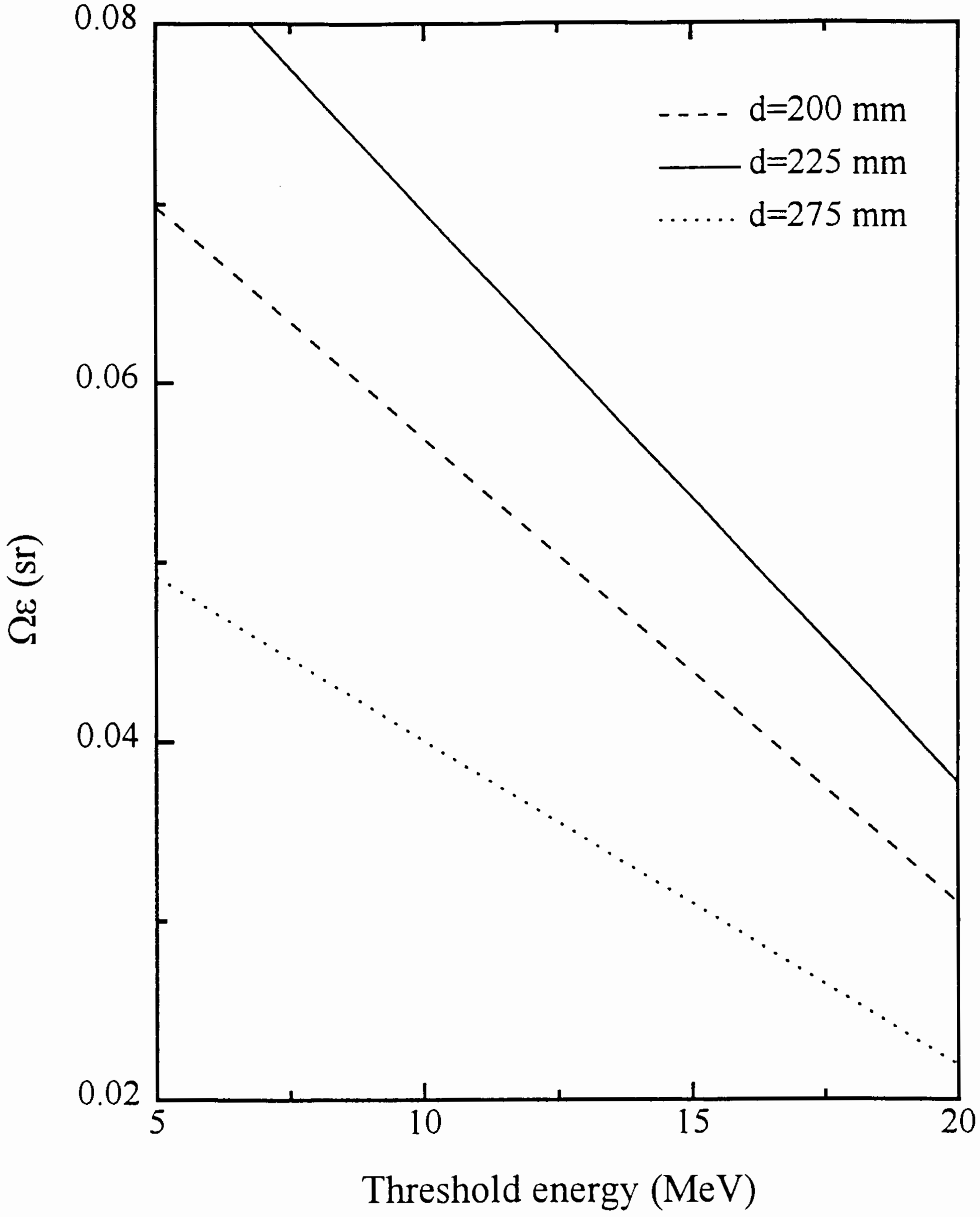

Figure 4-4: *Effect on calculated response function of Na(Tl) to 32.8 MeV photons when the distance from the centre of the source to the front face of the detector in the experiment was varied.*

Table 4.4: *Product of the effective solid angle and the efficiency $\Omega\varepsilon$ calculated at each angle.*

$\theta^{lab}_{n,\gamma}$ (deg)	45.0	60.0	75.0	90.0	105.0	120.0	135.0	150.0
$\Omega\varepsilon$ (sr)	0.0587	0.0670	0.0624	0.0586	0.0568	0.0568	0.0548	0.0423

4.1.3 Transformation from the laboratory to the centre-of-mass frames

The cross sections in the centre-of-mass frame $\frac{d\sigma(\theta^{cm}_{n,\gamma})}{d\Omega}$ are related to those in the laboratory frame $\frac{d\sigma(\theta^{lab}_{n,\gamma})}{d\Omega}$ by a factor $J(\theta)$ that is calculated from the kinematics of the reaction i.e.

$$\frac{d\sigma(\theta^{cm}_{n,\gamma})}{d\Omega} = \frac{d\sigma(\theta^{lab}_{n,\gamma})}{d\Omega} J(\theta^{lab}_{n,\gamma}) \tag{4.2}$$

where $\theta^{cm}_{n,\gamma}$ is the angle in the centre-of-mass frame between the photon and the neutron. Table 4.5 lists J as a function of the angle of detection $\theta^{lab}_{n,\gamma}$. Details of the calculations are contained in Appendix A.

Table 4.5: *J factors for transforming laboratory cross sections to the centre of mass, as a function of angle.*

$\theta^{lab}_{n,\gamma}$ (deg)	45.0	60.0	75.0	90.0	105.0	120.0	135.0	150.0
$J(\theta^{lab}_{n,\gamma})$	0.7866	0.8555	0.9393	1.0337	1.1326	1.2288	1.3146	1.3824

The angles in the laboratory frame $\theta^{lab}_{n,\gamma}$ are transformed to angles in the centre-of-mass frame as described in Appendix A. To facilitate comparison with photodisintegration experiments the angles are quoted as centre-of-mass angles formed between the proton and the gamma ($\theta^{cm}_{\gamma,p}$), where $\theta^{cm}_{\gamma,p} = (180° - \theta^{cm}_{n,\gamma})$. Because the differential cross section varies essentially as $\sin^2\theta$, the centroid of the angle does not correspond to the geometrical centre of the angle of detection. A Monte Carlo calculation was performed to calculate the centroid angle in the centre-of-mass taking into account the variation of the cross section. The angles $\theta^{cm}_{\gamma,p}$ that are listed in table 4.9 below are these centroid angles. The table also includes the angles of acceptance (FWHM) $\Delta\theta^{cm}_{\gamma,p}$, that were also calculated using the Monte Carlo program. Details of the Monte Carlo program are contained in ref. [He91].

4.2 Results

Combining the information from tables 3.3, 4.1, 4.4 and 4.5 the number of radiative captures at each angle are shown in table 4.6 together with the statistical uncertainty.

Table 4.6: *Final number of capture events as a function of angle after all corrections have been applied to the data.*

$\theta^{lab}_{n,\gamma}$	$\theta^{cm}_{\gamma,p}$ (deg.)	$\Delta\theta^{cm}_{\gamma,p}$ (deg.)	$N_c\frac{J}{f_d\Omega\varepsilon}$	$\Delta N_c\frac{J}{f_d\Omega\varepsilon}$
150.0	27.3	20	4438	726
135.0	39.8	19	7138	614
120.0	52.6	19	8601	547
105.0	66.1	18	11157	617
90.0	80.1	17	12553	595
75.0	94.7	17	10001	467
60.0	110.0	16	7226	435
45.0	126.0	15	6414	512

4.3 Normalisation and Fitting of Legendre Polynomials

Expressing the differential cross section in terms of Legendre polynomials allows for comparisons to be made with other measurements and with theory, as detailed in Chapter 1. However, for a significant Legendre polynomial fit to be made the data have to cover the range 0° to 180°. The present eight measurements span the range $\theta^{cm}_{\gamma p} = 27°$ to $126°$ and are not sufficient to constrain the fit at the extreme angles i.e. at 0° and 180° of the distribution [Sh70][Fi91]. Groups at Mainz [Zi92a][Zi92b] and at Louvain [Ni87] have recently measured the differential cross section at 0° and 180° for photon energies close to 34 MeV and these measurements were therefore used to constrain the fit to the present data. Table 4.7 shows the cross section data at 0° and 180° as measured by the Mainz and Louvain groups, respectively.

Table 4.7: *Differential cross section data for* $\theta_{\gamma p}^{cm}$ *= 27° to 126° measured by groups from Mainz [Zi92a][Zi92b] and Louvain [Ni87] at photon energies close to 34 MeV.*

Group [ref.]	E_γ (MeV)	$\frac{d\sigma}{d\Omega}(0^\circ)$ $\mu b\ sr^{-1}$	$\frac{d\sigma}{d\Omega}(180^\circ)$ $\mu b\ sr^{-1}$
Mainz [Zi92a]	31.7(26)	5.83(6)	–
Mainz [Zi92b]	33.9(29)	–	4.28(9)
Louvain[Ni87]	32.8	4.72(26)	3.93(40)

A weighted least-squares Legendre polynomial fit was made to the combined data set and a scaling factor was introduced for the present data only. The scaling factor was adjusted in the fitting procedure so as to normalise the total photodisintegration cross section to 287 μb. This value is based on calculations made using the Bonn-r space potential [Sc89][Ar93]. It is also consistent to within 2% of the value calculated using the Paris potential [Wi88][Ar93] as well as with that obtained from the global fits of refs. [Ro89] and [Je94]. Since the A_0 coefficient of the Legendre polynomial expansion is related to the total cross-section σ_T by a factor of 4π i.e. $\sigma_T = 4\pi A_0$, the scaling factor was adjusted during the fitting procedure to equate A_0 to a value of 22.9 μb sr^{-1}. Varying the values that were assumed for the 0° and 180° differential cross sections by 10% had a negligible effect (<1%) on the procedure that was used. This is attributed to the effect of the $\sin\theta$ factor in the integration of the differential cross section in order to obtain the total cross section.

The fitting was carried out using the matrix inversion technique described by Bevington [Be69]. Each datum was weighted in proportion to the inverse square of its statistical uncertainty. Legendre polynomial expansions to order 3 and 4 were investigated using the χ^2/dof and the F-test to monitor the quality of the fits. The column labeled F_r in table 4.8 shows the probability of rejecting the n^{th} coefficient in the expansion up to order n. The results of the fit, in terms of χ^2/dof and F_r, are summarised in table 4.8,

The F-test clearly indicates that the data are incompatible with a 4th order fit of

Table 4.8: *Results of third and fourth order Legendre polynomial fits to the present differential cross section data combined with the data at* 0° *and* 180° *from Mainz [Zi92a][Zi92b] and Louvain [Ni87], respectively.*

Fit to	With Mainz data		With Louvain data	
order n	χ^2/dof	F_r (%)	χ^2/dof	F_r (%)
3	2.2	0	2.3	0
4	2.7	87	2.7	96

the Legendre polynomial expansion, since in the case where the Mainz data were used the probability that A_4 should be rejected is 87% while in the case of the Louvain data the probability is 96%. The fit to fourth order was therefore rejected. Because of the orthogonal nature of the polynomial the values for A_1 and A_2 did not change significantly from those resulting from a fit to second order only. The effect on the fit due to an estimated systematic uncertainty of 5% was checked by adding this uncertainty in quadrature [Mu79][Mu84] to the statistical uncertainties. The results of this fit were found to be identical to those in which only the statistical uncertainties were used to weight the data.

4.4 The differential cross sections

The differential cross sections $\frac{d\sigma}{d\Omega}$ for ^{2}H(γ,p)n at $E_\gamma = 33.9$ MeV are shown in Table 4.9. The uncertainties indicated are purely statistical. The angles $\theta^{cm}_{\gamma,p}$ in the table are the centroid angles referred to above. Table 4.9 also lists the corresponding differential cross sections for the inverse n-p capture reaction $\left(\frac{d\sigma}{d\Omega}\right)_{cap}$, which are related to $\frac{d\sigma}{d\Omega}$ by detailed balance as described in Chapter 2. For 63.4 MeV neutrons corresponding to $E_\gamma = 33.9$ MeV the relationship is given by (see figure 2-4)

$$\left(\frac{d\sigma}{d\Omega}\right)_{cap} = \frac{1}{17.3}\frac{d\sigma}{d\Omega} \tag{4.3}$$

The differential cross sections for ^{2}H(γ,p)n at $E_\gamma = 33.9$ MeV are plotted in figure 4-5, together with the results of the least-squares Legendre polynomial fit to third order.

Table 4.9: *Differential cross sections for* $^2H(\gamma,p)n$ *at* E_γ = *33.9 MeV and* $^1H(n,d)\gamma$ *at* E_n *=63.4 MeV.*

$\theta^{cm}_{\gamma,p}$ (deg)	$\frac{d\sigma}{d\Omega}\left(\frac{\mu b}{sr}\right)$	$\left(\frac{d\sigma}{d\Omega}\right)_{cap}\left(\frac{\mu b}{sr}\right)$
27.3	13.2(22)	0.76(13)
39.8	21.4(18)	1.23(10)
52.6	25.7(16)	1.49(9)
66.1	33.3(18)	1.92(10)
80.1	37.5(18)	2.17(10)
94.7	29.9(14)	1.73(8)
110.0	21.6(13)	1.25(7)
126.0	19.1(15)	1.10(9)

Figure 4-5 also shows the 0° and 180° Mainz data [Zi92a] and the theoretical predictions of potential model calculations based on the Bonn r-space potential [Sc89][Ar93].

The Legendre polynomial coefficients A_1 to A_3, resulting from the fit are shown in table 4.10 indicating (a) the results from the present data combined with the Mainz data and (b) the present data combined with the Louvain data, for 0° and 180° in each case.

Table 4.10: *Legendre polynomial coefficients* A_1, A_2 *and* A_3 *obtained from a fit to the present data combined with (a) the Mainz data; and (b) the Louvain data for* $^2H(\gamma,p)n$ *at* E_γ = *33.9 MeV.*

Data set	A_0	A_1	A_2	A_3
(a) present data + Mainz data	22.9(5)	6.5(8)	-17.9(5)	-5.7(8)
(b) present data + Louvain data	22.9(5)	6.5(8)	-18.5(5)	-6.1(8)

The two sets of coefficients, A_1 to A_3, are consistent with each other showing that the analysis is insensitive to the values used for the 0° and the 180° cross sections, within the ranges defined by the Mainz and Louvain data.

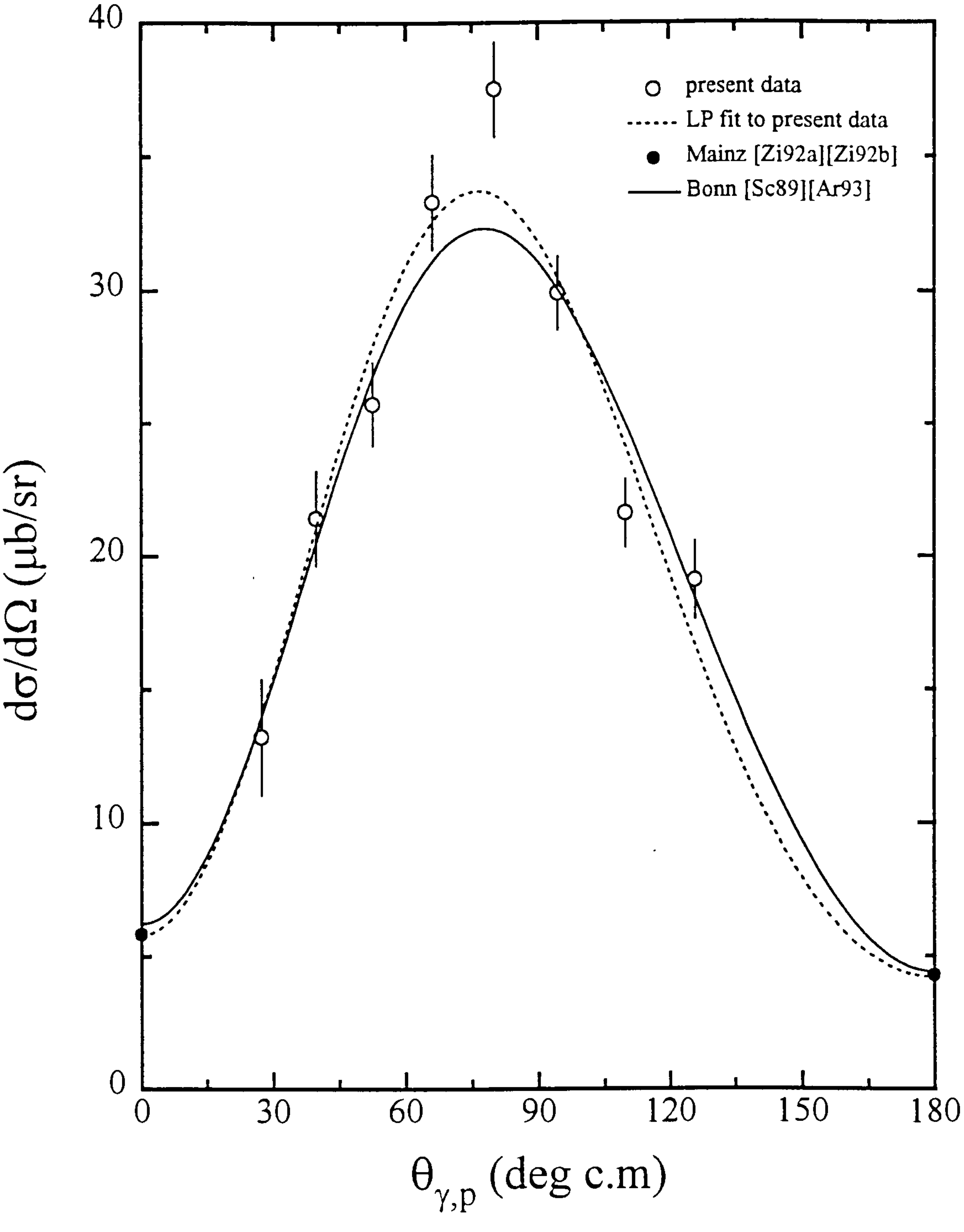

Figure 4-5: *Differential cross section for* $^2H(\gamma,p)n$ *at* $E_\gamma = 33.9$ *MeV showing present data (open circles), Mainz data [Zi92a][Zi92b] (solid circles), least-squares fit (dashed curve) and predictions based on the Bonn r-space potential [Sc89] (solid curve).*

Chapter 5

Discussion

5.1 Comparison of the Legendre polynomial coefficients with experiment and theory

The Legendre polynomial (LP) coefficients provide an accurate and convenient way of characterising the shape of the differential cross section [We71][Ca82b] allowing for detailed comparisons between different experiments, and between experiment and theory. The present measurements of the differential cross section may, therefore, be compared directly with other experimental data taken at the same or nearby photon energy, although there are few data in this energy range. Table 5.1 below, is a comparison of the LP coefficients A_1, A_2 and A_3 obtained from the present measurements at $E_\gamma =$ 33.9 MeV with the results of Weissman and Schultz [We71] obtained at $E_\gamma = 30$ and 35 MeV. Set (a) is the present work combined with the Mainz data [Zi92a][Zi92b] and set (b) is the present work combined with the Louvain data [Ni87]. The table, adapted from Firk [Fi79], also lists F_r the probability of rejecting the A_4 coefficient as part of the LP fit. Figure 5-1 is a graphical representation of the data in table 5.1 excluding set (b). It is clear that the coefficients A_1, A_2 and A_3 obtained in the present measurement are consistent with those of Weissman and Schultz. Shin et al. [Sh70] obtained LP coefficients from photoneutron angular distribution measurements and compared the ratios $\frac{A_1}{A_0}$, $\frac{A_2}{A_0}$, and $\frac{A_3}{A_0}$ from their work with those from Weissman and Schultz. For the energies in the range $E_\gamma =$ 30 -35 MeV, the two sets of ratios were found to agree to within one standard deviation.

Table 5.1: *Legendre polynomial coefficients from the present work compared with results from Weissman and Schultz [We71]*

Photon energy (MeV)	A_1	A_2	A_3	F_r(%) for A_4
30 [We71]	6.07(84)	-21.2(15)	-5.9(16)	100
35 [We71]	5.53(57)	-17.3(12)	-4.5(13)	60
33.9 [set (a)]	6.5(8)	-17.9(5)	-5.7(8)	87
33.9 [set (b)]	6.5(8)	-18.5(5)	-6.1(8)	96

The present data may also be compared with LP coefficients derived from global fits and from theory. Table 5.2 shows the LP coefficients calculated from various global fits [Ro89][De82][Th86][Je94] together with predictions based on potential model calculations for both the Bonn r-space potential [Sc89][Ar93] and the Paris potential [Wi88][Ar93]. In both cases meson exchange currents, isobar configurations and relativistic corrections are included. To facilitate comparison between the various sets of coefficients the data in table 5.2 are also displayed in figure 5-2 below.

The present values (sets (c) and (d)) for A_2 deviate from both the theoretical values (sets (a) and (b)) and the global fits (sets (e) and (f)). The deviation is larger in the case of set (d) which was obtained by analysis in combination with the Louvain data than in the case of set (c) which was obtained in combination with the Mainz data. The values of A_1 and A_3 from the present work are, however, consistent with those obtained from the global fits (sets (e),(f) and (g)) but deviate from the values predicted by theory. It should be noted that the results of the experiments mentioned in the section above are included in the data used in the global fits.

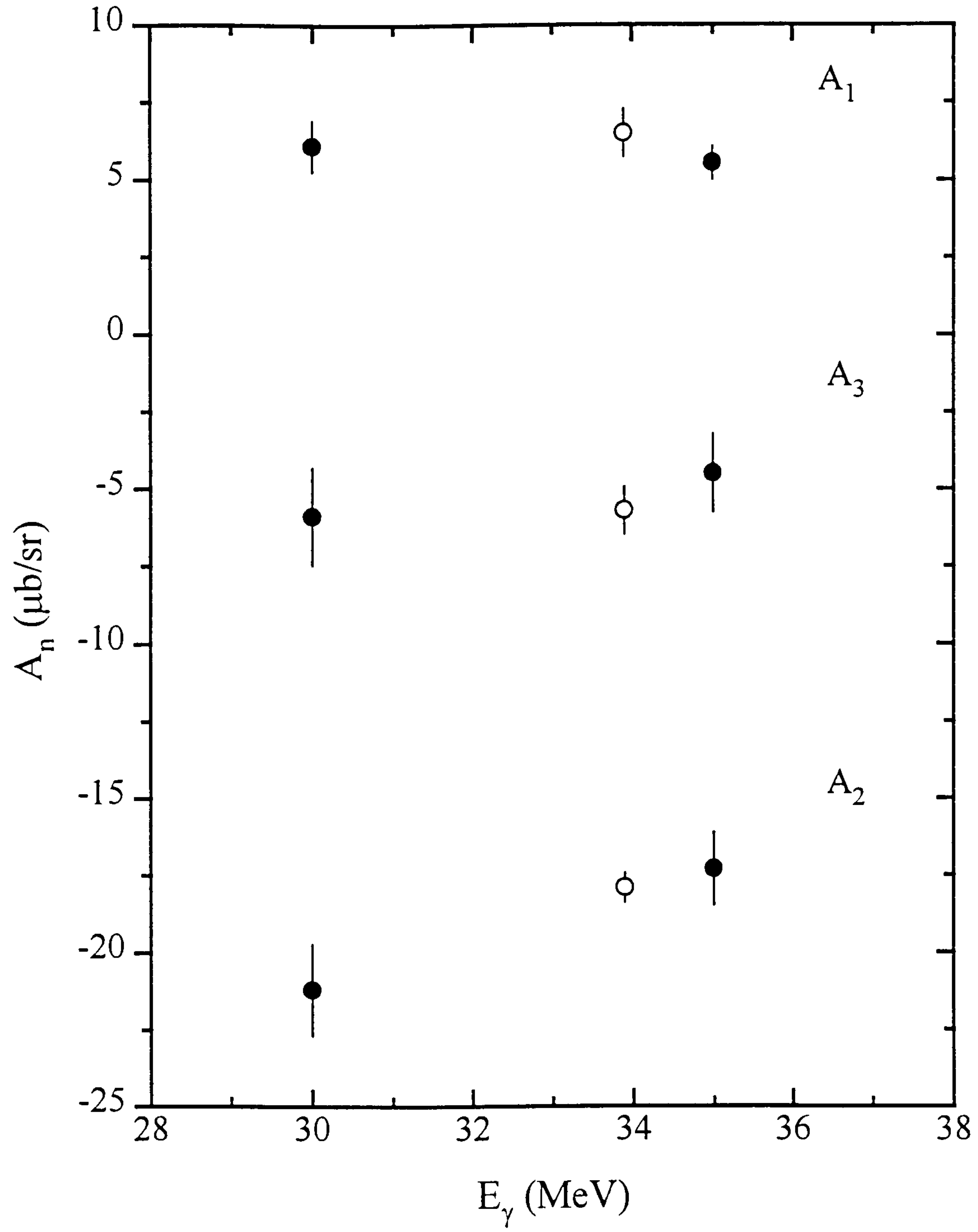

Figure 5-1: *Legendre polynomial coefficients A_1, A_2 and A_3 as a function of photon energy showing the results of Weissman and Schultz [We71] (closed circles). The open circles are the results from the present work combined with the Mainz data [Zi92a][Zi92b].*

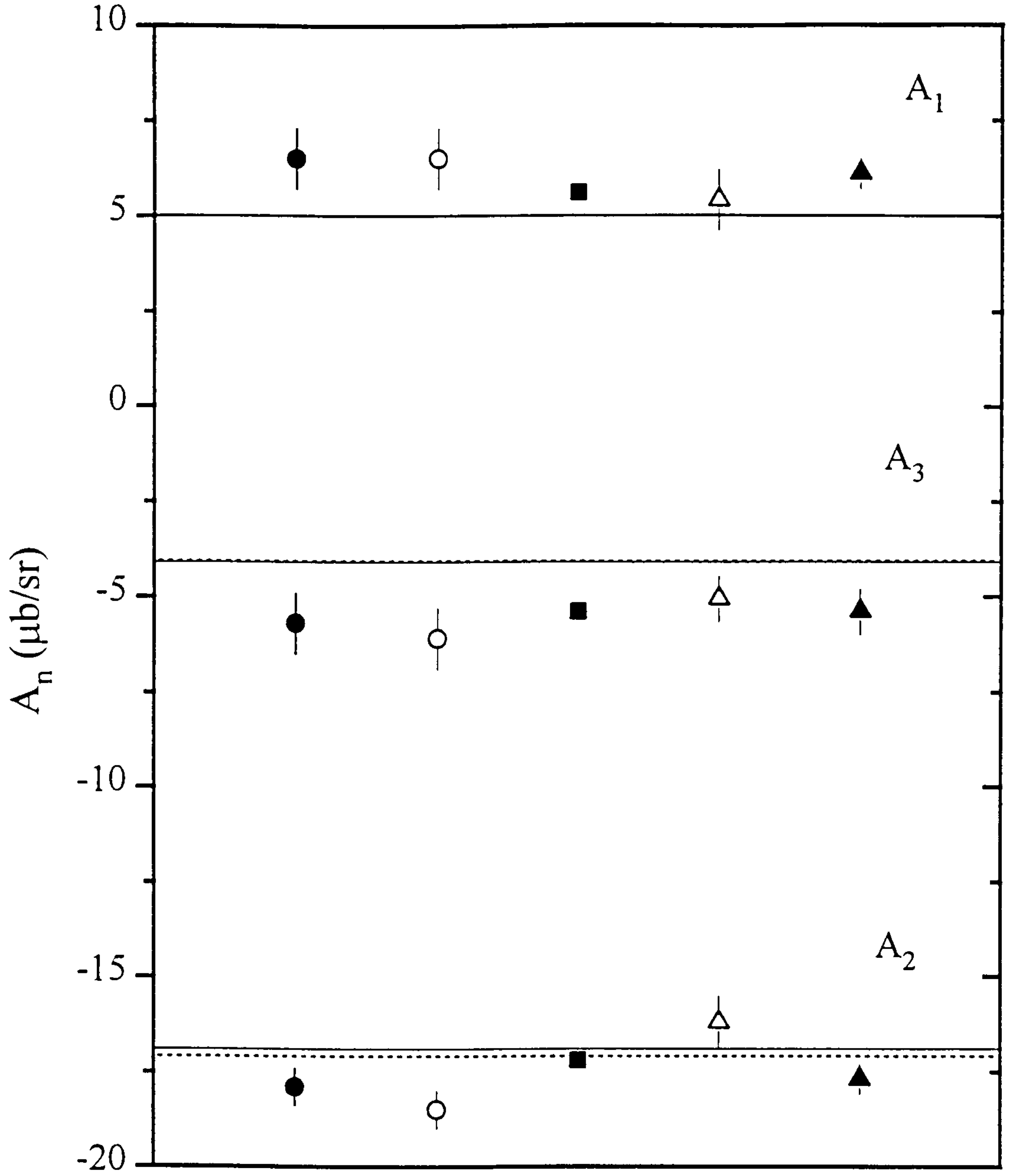

Figure 5-2: *Comparison of Legendre polynomial coefficients from table 5.2: (a) Bonn prediction (solid lines); (b) Paris prediction (dashed lines); (c) fit to present and Mainz data (solid circles); (d) fit to present and Louvain data (open circles); and global fits (e) Rossi et al. (squares); (f) De Pascale et al. (solid triangles) and (g) Jenkins et al. (open triangles). The uncertainties for set (e) are smaller than the point size.*

Table 5.2: *Legendre polynomial coefficients characterising the differential cross section from* $^2H(\gamma,p)n$ *at* E_γ = *33.9 MeV for the present measurements compared with those derived from global fits and potential model calculations.*

Set	A_1	A_2	A_3	A_4
(a) Bonn r-space potential [Sc89][Ar93]	5.00	-16.9	-4.09	-0.7
(b) Paris potential [Wi88][Ar93]	5.02	-17.1	-4.07	-0.6
(c) present data and Mainz data [Zi92a][Zi92b]	6.5(8)	-17.9(5)	-5.7(8)	-
(d) present data and Louvain data [Ni87]	6.5(8)	-18.5(5)	-6.1(8)	-
(e) global fit of Rossi et al. [Ro89]	5.6(1)	-17.2(1)	-5.4(1)	-0.83(3)
(f) global fit of De Pascale et al. [De82]	5.4(8)	-16.2(7)	-5.0(6)	-0.7
(g) global fit of Jenkins et al. [Je94]	6.1(4)	-17.7(4)	-5.4(6)	

5.2 Discussion

5.2.1 Multipole contributions

The angular distributions depend on both the amplitudes and the phases of the partial waves that arise from the most important multipole transitions viz. M1, E1, M2, E2 and E3. Table 5.3 shows the leading order multipole contributions which affect the LP coefficients. By way of example, E1-M1 (term *a*) would be calculated by adding the partial waves due to E1 transitions to the partial waves due to M1 transitions. The A_1 LP would be calculated by adding terms *a, b, c* and *d*. The table is based on a similar table in ref. [Sc91] as well as on refs. [Ca82b][Ar91] which provide expressions for the LP coefficients in terms of the multipole contributions.

Figure 5-3 taken from ref. [Sc91] shows the multipole contributions to the LP coefficients for the Bonn-r space potential as a function of photon energy relative to the total value of the coefficient. It should be noted that the results of adding terms are shown as each of the terms is added to the previous term in the order specified. For example, in the case of A_3, the contribution from term j to the total is indicated

Table 5.3: *Leading order multipole contributions to the Legendre polynomial coeffcients.*

LP coefficient	Multipole contribution	Term
A_1	E1-M1	a
	E1-E2	b
	M1-M2	c
	E2-E3	d
A_2	E1-E1	e
	M1-M1	f
	E2-M1	g
	E1-M2	h
	E1-E3	i
A_3	E1-E2	j
	M1-M2	k
	E3-M1	l

as the dashed line, while the result of adding term k to this is shown as the dashed-dot line. The final result, the dashed-dot-dot line, is obtained by adding term l.

The main contribution to A_1 is seen to come from the (E1-E2) term while the (E1-M1) and (M1-M2) terms contribute less than 2% at 35 MeV, for example. Similarly for A_3 the (E1-E2) contribution dominates, with (M1-M2) and (E3-M1) contributing less than 2% to the total strength. The effect of adding higher multipoles by way of an (E1-E4) term is not shown on the graph. However, it adds destructively and reduces the total relative strength to unity which is essentially the (E1-E2) part [Sc91]. The A_2 term is dominated by the electric dipole (E1-E1) with the magnetic dipole term (M1-M1) having about a 5% effect. The E3 multipole which enters via the (E3-E1) term also has an effect of similar magnitude. However, the overall result is that the electric dipole term describes most of the strength since the magnetic dipole term and the (E3-E1) term cancel out each other.

A common factor between the A_1 and the A_3 coefficients is the dominant contribution of the E2 multipole via the E1-E2 interference term. It has, therefore, been suggested that the problem with the odd-A coefficients may lie with the incorporation of the E2 multipole transitions into the theoretical calculations. Further evidence for this contention has been provided by Hadjimichael et al. [Ha87, Ha87] who have shown that the ratios of the differential cross section at $\theta_{\gamma,p} = 45^\circ$, 135° and 155° to that at $\theta_{\gamma,p} = 90^\circ$ provide a way of studying the E2 transitions in close detail. Using the data of Stephenson et al. [St87] they concluded that the strength of the E2 transition needed adjusting in order to yield agreement with the measured ratios. Schmitt et al. [Sc91] have indicated that by artificially increasing the E2 strength by between 25% and 50% it is possible to model the experimental measurements of Stephenson et al. [St87] successfully.

Since the E2 multipole contributes to the cross section predominantly via the (E1-E2) term [Ha87][Sc91],it has been suggested that the phases of the E1 and E2 multipole matrix elements could be incorrect. However, Schmitt et al. [Sc91] have reported that changing the phases artificially, within the limits of the uncertainties of the experimental data obtained from NN scattering, does not have any significant effect on the results. A mechanism that could lead to an increase in the E2 strength would be an

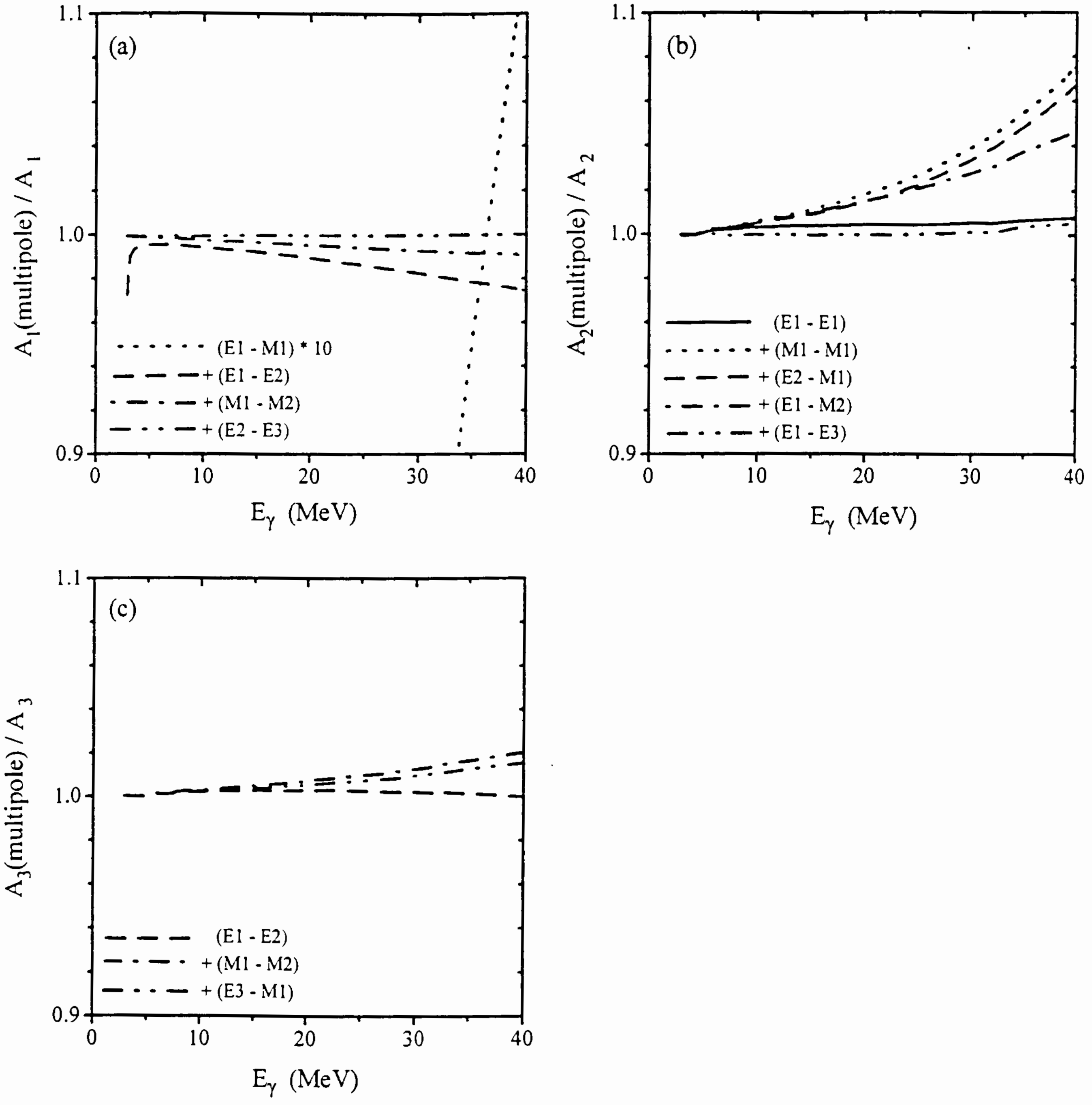

Figure 5-3: *Cumulative multipole contributions to the Legendre polynomial coefficients A_1, A_2 and A_3 divided by the total multipole contribution, as a function of photon energy. The total contribution includes all multipoles up to $L = 4$. Note that for A_1 the E1-M1 term is shown multiplied by a factor of 10.*

increased E2 contribution from the one-body current. However, Schmitt et al. [Sc91] have indicated that for the results to be affected in the way required, the increase would have to be of an order of magnitude which cannot be justified on theoretical grounds. Another possibility would be to increase the E2 strength by increasing the exchange current contribution beyond those of the Siegert operator. This is discussed in the section below.

5.2.2 Electromagnetic currents and relativistic corrections

The multipole transitions discussed above arise from the interaction of the various electromagnetic current contributions with the photon field. The relative contributions of these currents to the LP coefficients are shown in figure 5-4 which is taken from ref. [Sc91].

With regard to A_1 and A_3 it can be seen that the effect of adding any one of the currents has a small effect, less than 2%, over the photon energy range that is shown. The A_2 coefficient behaves similarly except above 30 MeV where these contributions start to increase in importance. Table 5.4 provides more detail for E_γ = 30 and 40 MeV, respectively, from calculations based on the Paris potential [Wi88][Ar93]. It is clear that the inclusion of the effects in question increases the A_2 coefficient by less than 6% in this energy range and the values of A_1 and A_3 by less than 1% as indicated.

Table 5.4: *Potential model calculations based on the Paris potential showing the effect on the LP coefficients when MEC, IC and RC effects are included explictly beyond that contained in the Normal part.*

Calculations based on	E_γ=30 MeV			E_γ=40 MeV		
	A_1	A_2	A_3	A_1	A_2	A_3
(a) Paris Potential Normal Part N only	5.65	-20.2	4.65	4.30	-11.1	3.24
(b) Paris Potential N+MEC+IC+RC	5.66	-21.3	4.69	4.34	-12.5	3.32

A similar conclusion was reached by Kassaee et al. [Ka89] who reported that corrections to the meson exchange currents and the spin-orbit term could not account for

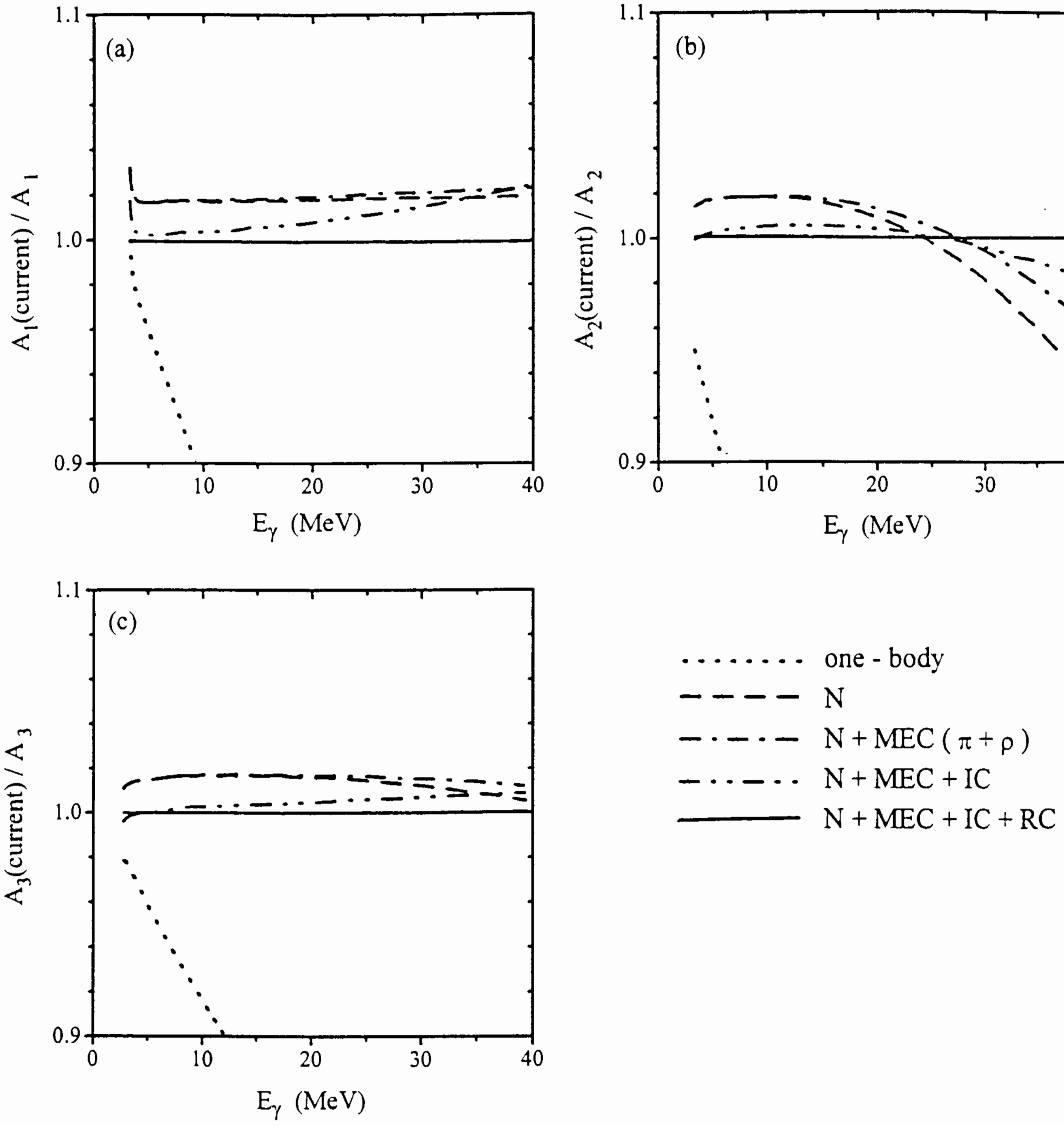

Figure 5-4: *Contributions of the various electromagnetic currents to the Legendre polynomial coefficients A_1, A_2 and A_3 calculated for the Bonn r -space potential.*

the enhancement of the E2 multipole transition that had been proposed on phenomenological grounds, in order to obtain the good agreement [Ha87] with the experiment of Stephenson et al. [St87].

5.2.3 NN potentials and quark currents

Since the theoretical predictions are very insensitive to the MEC/IC/RC corrections, especially for the coefficients A_1 and A_3, it appears very unlikely that the deviations in the Legendre coefficients that have been measured may be explained by meson exchange currents, isobar configurations or relativistic corrections. The table shows, therefore, that in this energy range the predictions of potential model calculations, for a given potential, are well described by the procedure outlined by Partovi [Pa64] in which MEC and IC corrections are included only via the Siegert operators. One possibility is that the data are possibly pointing to deficiencies in the meson-exchange potentials that have been used up to now [Ja93a][Ja93b]. Recently, Stoks et al. [St94] have presented a new version of the Nijmegen potential [Na78], Nijm93, which provides a more accurate description of the available NN scattering data [Be90][St93] than either the Paris or Bonn r-space potentials. The Nijm93 potential is currently being used to calculate various observables from photodisintegration [Wo96]. However, at the time of writing, a set of Legendre polynomial coefficients was not available to enable a direct comparison with the present work.

It is also possible that quark exchange currents may be playing a role. For example, Buchmann [Bu95], using the non-relativistic quark model, has found that the gluon and pion quark exchange currents (figure 5-5) substantially modify the meson exchange contribution in the deuteron since at small internucleon distances quark exchanges between the quark clusters become dominant.

Buchman has concluded that "...the interpretation of ... experimental data in terms of conventional exchange currents thus possibly misses these aspects related to the 6-quark structure of the deuteron." However, as yet the detailed calculations still remain to be done.

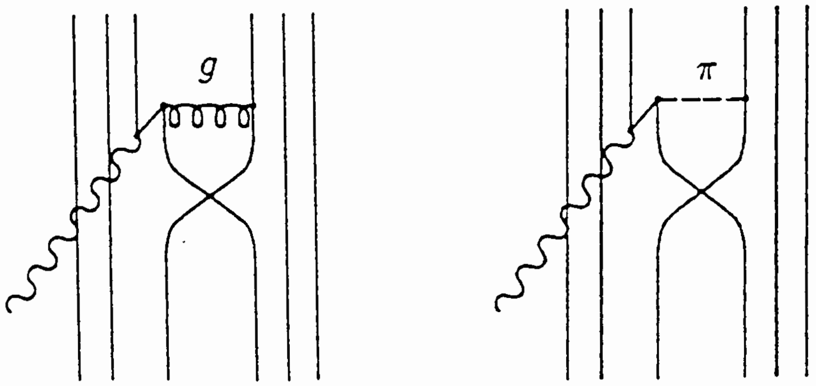

Figure 5-5: *Gluon and pion quark exchange currents in the deuteron. Figure from [Bu95].*

5.3 Conclusions

The angular distribution of photons from n-p radiative capture at $E_n = 63.4$ MeV has been measured using an experimental technique in which both the photons and the deuterons were clearly identified and selected. The data were transformed to photodisintegration cross sections at the equivalent laboratory energy, $E_\gamma = 33.9$ MeV. The Legendre polynomial coefficients A_1, A_2 and A_3 obtained from the analysis are in agreement with other data at nearby energies and the results from global fits [Ro89][De82][Je94]. The fits from both Rossi et al. [Ro89] and Jenkins et al. [Je94], which are based on data over a wide energy range and include recent accurate data from experiments using techniques such as tagged photon beams, indicate significant deviations from theory with regard to A_1, and A_3 in the energy range $E_\gamma = 20$ to 40 MeV. The present measurements therefore, provide further evidence of such a systematic deviation between experiment and the predictions based on potential model calculations for photodisintegration. Within the framework of conventional potential model theory, a number of plausible suggestions have been made concerning the sources of the discrepancies. However, none of them is convincing.

For A_1 and A_3 the differences between the values obtained from the global fits and from theory are seen to increase towards lower energies (see figure 1-12). For example, at 20 MeV the differences are between 25% [Ro89] and 50% [Je94]. These differences are of the order of a few standard deviations. Fink et al. [Fi91] have performed n-p capture measurements at a number of energies in the range $E_\gamma = 10$ to 25 MeV ($E_n = 20$ to 50 MeV) using a different technique to that of the present work. However, since the deuteron was not identified in coincidence with the associated photon, there was a large gamma background arising from neutron reactions on carbon in the target. This appears to have led to large systematic uncertainties in the measurements [Sc91]. In the present technique the deuteron is clearly identified in coincidence with the gamma ray from the $np \rightarrow d\gamma$ process which should adequately suppress this background.

In summary, the present technique provides a highly selective tool for carrying out a systematic study of n-p capture below 40 MeV. The technique appears capable of providing data that would be sufficiently accurate to provide firm evidence for the deviations between potential model calculations and the global fits.

Appendix A

Kinematics

A.1 Introduction.

This appendix deals with the kinematics that govern the $n + p \rightleftharpoons d + \gamma$ reactions, the results of which are used to calculate various factors required in the analysis. The discussion is based largely on refs. [Ba61] and [Mi67]. In the discussion both $\hbar$ and c are set equal to 1and masses are in units of MeV/c^2.

A.2 Photon energy measured in the laboratory as a function of the angle of detection

For the $np \rightarrow d\gamma$ reaction in the laboratory frame, momentum conservation can be expressed as

$$\vec{p}_n + \vec{p}_p \rightarrow \vec{p}_d + \vec{p}_\gamma \tag{A.1}$$

where $\vec{p}_i$ is the momentum of particle i. Since the proton is stationary in the laboratory frame the momentum of the proton $\vec{p}_p$ is zero. The momenta in equation A.1 can be resolved into components parallel and perpendicular to the momentum of the incident neutron which leads to the following two equations

$$p_n = p_d \cos\theta^{lab}_{n,d} + p_\gamma \cos\theta^{lab}_{n,\gamma} \tag{A.2}$$

$$0 = p_\gamma \sin \theta_{n,\gamma}^{lab} - p_d \sin \theta_{n,d}^{lab} \tag{A.3}$$

If W is the sum of the rest energy (mc^2) and the kinetic energy T of a particle then energy conservation leads to equations A.4 and A.5

$$W_n^{lab} + W_p^{lab} \rightarrow W_d^{lab} + W_\gamma^{lab} = W_{total}^{lab} \tag{A.4}$$

$$m_n + T_n + m = m_d + T_d + p_\gamma \tag{A.5}$$

The three equations A.2, A.3 and A.5 can be used together to provide a relationship between $\theta_{n,\gamma}^{lab}$ the angle at which the photon is emitted in the laboratory frame and E_γ^{lab} the energy measured in the laboratory frame. From the same set of equations a relationship between E_d^{lab} and either $\theta_{n,\gamma}^{lab}$ or $\theta_{n,d}^{lab}$ can be obtained. A plot of E_γ^{lab} as a function of $\theta_{n,\gamma}^{lab}$ for 63.4 MeV incident neutrons is shown in figure A-1. Figure A-2 shows plots of (a) E_d^{lab} as a function $\theta_{n,\gamma}^{lab}$ and (b) E_d^{lab} as a function of $\theta_{n,d}^{lab}$ the deuteron recoil angle in the laboratory frame.

A.3 Transformation of angles from the laboratory frame to the centre-of-mass frame

Using the Lorentz transformations for relating positions x and times t between coordinate systems moving relative to each other, the following relationships can be written

$$x_{cm} = \frac{x^{lab} - Vt^{lab}}{\sqrt{1-\beta_c^2}} \text{ , } t_{cm} = \frac{t^{lab} - Vx/c^2}{\sqrt{1-\beta_c^2}} \text{ and } y^{cm} = y^{lab} \tag{A.6}$$

where $\beta_c = \frac{V}{c}$and V is the velocity of the centre-of-mass in the laboratory system and

$$x_{lab} = v_{lab} t_{lab} \cos \theta_{lab} \text{ and } y_{lab} = v_{lab} t_{lab} \sin \theta_{lab} \tag{A.7}$$

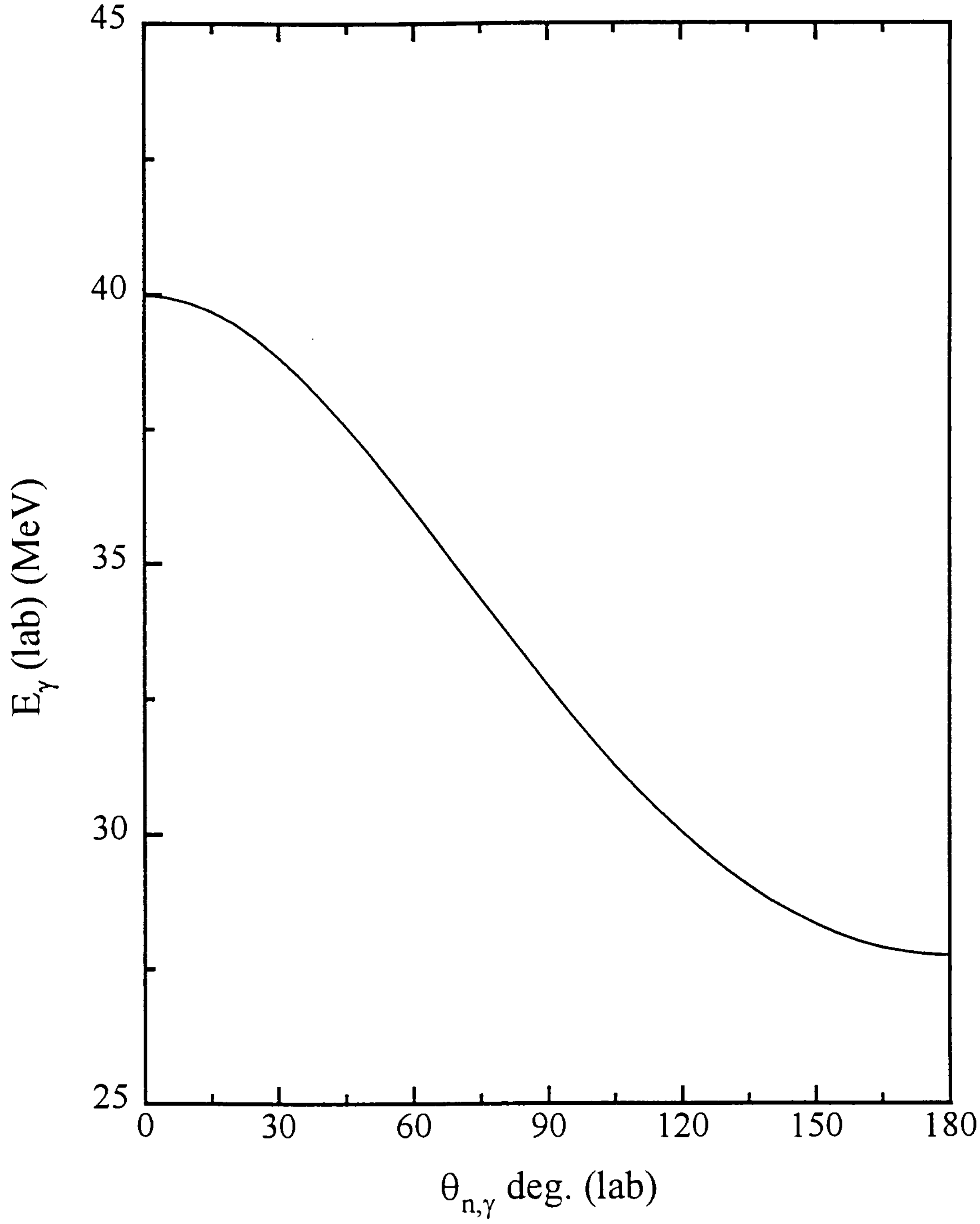

Figure A-1: *Photon energy in the laboratory frame* $E_\gamma^{lab}(\theta_{n,\gamma})$ *as a function of* $\theta_{n,\gamma}$ *the angle at which the photon is emitted in the laboratory frame relative to the direction of the incident neutron.*

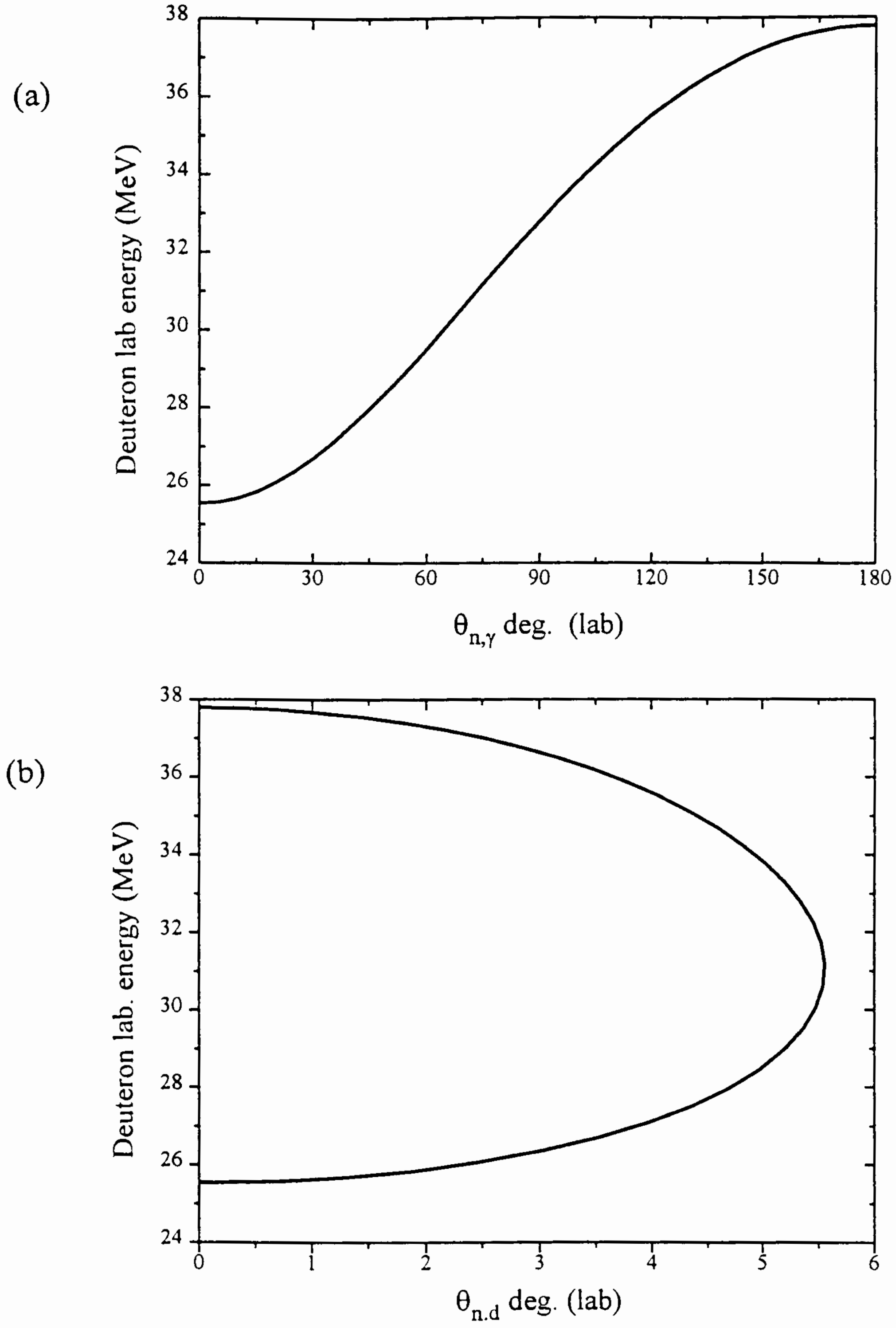

Figure A-2: *Deuteron recoil energy in the laboratory frame* E_d^{lab} *as a function of (a)* $\theta_{n,\gamma}^{lab}$ *the angle at which the photon is emitted and; (b)* $\theta_{n.d}^{lab}$ *the deuteron recoil angle in the laboratory frame. Both angles are defined with respect to the direction of the incident neutrons.*

$$x_{cm} = v_{cm}t_{cm}\cos\theta_{cm} \text{ and } y_{cm} = v_{cm}t_{cm}\sin\theta_{cm} \tag{A.8}$$

From the three equations above a relationship between the laboratory angle and the angle in the centre-of-mass can be obtained viz.,

$$\tan\theta^{cm} = \frac{\sin\theta^{lab}}{\Gamma(\cos\theta^{lab} - \frac{\beta_c}{\beta})} \tag{A.9}$$

where $\Gamma = \frac{1}{\sqrt{1-\beta_c^2}}$ and $\beta = \frac{v^{lab}}{c}$

In the case of the outgoing photon $v^{lab} = c$, so that $\beta = 1$ in equation A.9. From this equation the centre-of-mass angles $\theta^{cm}_{n,\gamma}$ corresponding to the laboratory angles $\theta^{lab}_{n,\gamma}$ can be obtained. However, it is usual to quote differential cross sections for photodisintegration as a function of $\theta^{cm}_{p,\gamma}$ the angle between the directions of the proton and photon momenta in the centre-of-mass frame. The two centre-of-mass angles are related as follows: $\theta^{cm}_{p,\gamma} = 180° - \theta^{cm}_{n,\gamma}$. Figure A-3 shows a plot of $\theta^{cm}_{p,\gamma}$ as a function of $\theta^{lab}_{n,\gamma}$.

A.4 Transformation of differential cross sections from the laboratory frame to the centre-of-mass frame

The relationship between the differential cross section in the laboratory frame $(\frac{d\sigma}{d\Omega})_{lab}$ and that in the centre-of-mass $(\frac{d\sigma}{d\Omega})_{cm}$,which is usually written simply as $\frac{d\sigma}{d\Omega}$, can be obtained by noting that

$$\frac{d\sigma}{d\Omega} = (\frac{d\sigma}{d\Omega})_{lab}\frac{\sin\theta_{lab}}{\sin\theta_{cm}}\frac{d\theta_{lab}}{d\theta_{cm}} \tag{A.10}$$

Performing the required differentiation on equation A.10 yields

$$\frac{d\sigma(\theta)}{d\Omega} = \frac{\sin^3\theta_{lab}}{\Gamma\sin^3\theta_{cm}(1-\beta\cos\theta_{lab})}(\frac{d\sigma}{d\Omega})_{lab} = J(\theta) \times \left(\frac{d\sigma(\theta)}{d\Omega}\right)^{lab} \tag{A.11}$$

Figure A-4 is a plot showing the transformation factor $J(\theta)$ as a function of laboratory angle $\theta^{lab}_{n,\gamma}$ i.e. the angle at which the photon is emitted relative to the neutron momentum in the laboratory frame.

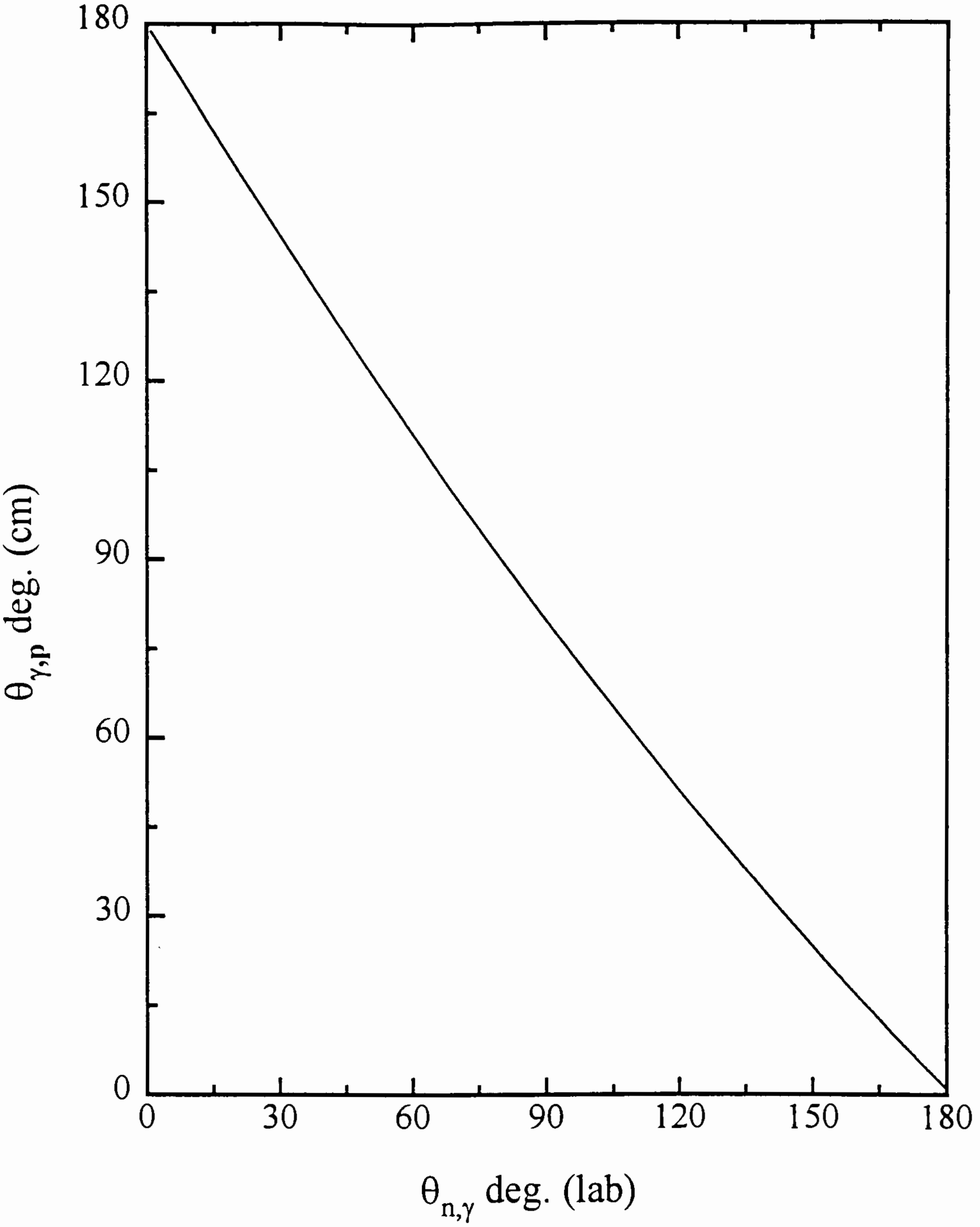

Figure A-3: *Plot of the centre-of-mass angle* $\theta^{cm}_{p,\gamma}$ *versus the laboratory angle* $\theta^{lab}_{n,\gamma}$

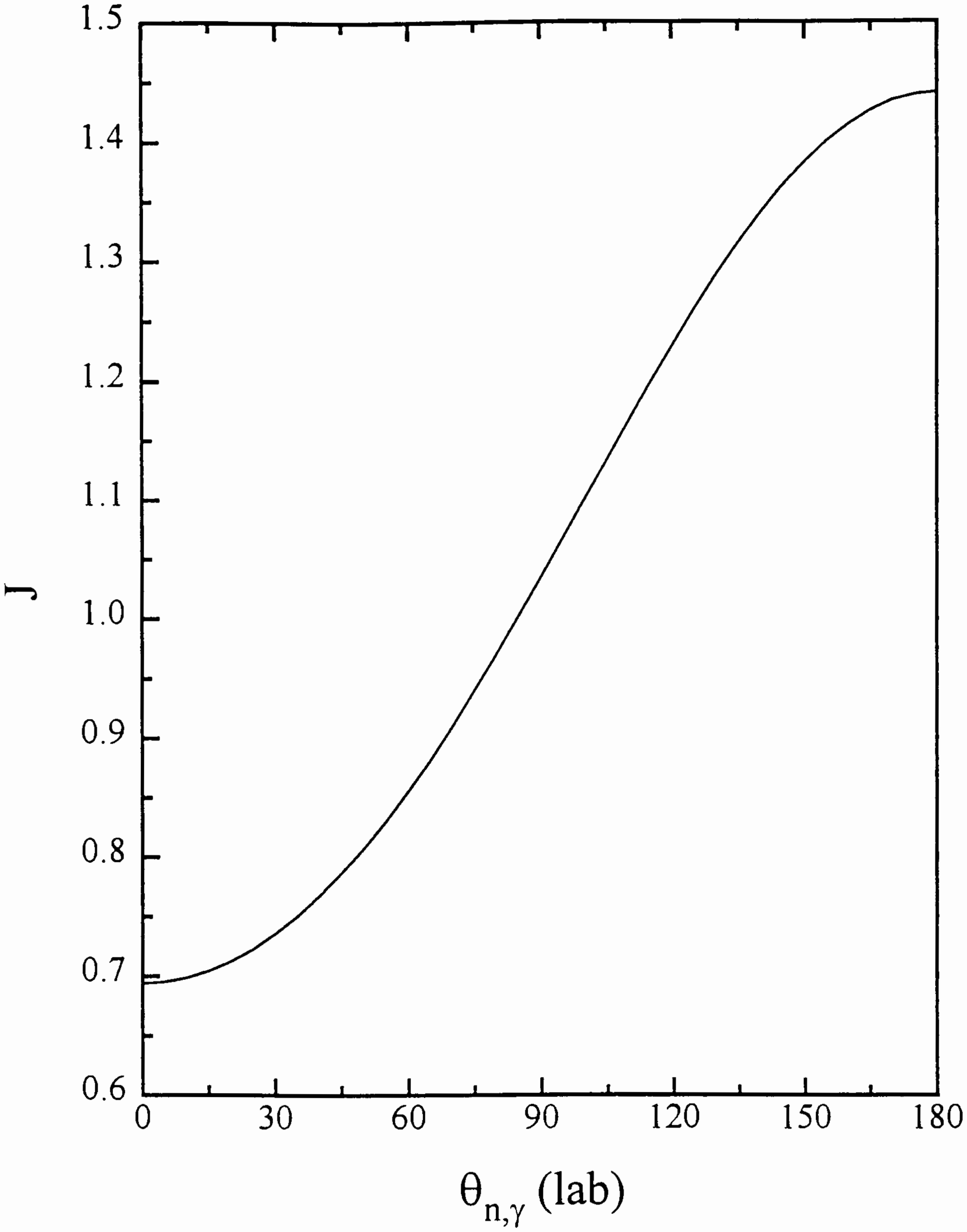

Figure A-4: *Plot showing the factor $J(\theta)$ for transforming differential cross sections in the laboratory frame to differential cross sections in the centre-of-mass frame as a function of the laboratory angle $\theta_{n,\gamma}$.*

A.5 Energy of the photon in the centre-of-mass frame

The total energy in the centre-of-mass is given by

$$W_n^{cm} + W_p^{cm} = W_{total}^{cm} = W_d^{cm} + W_\gamma^{cm} \tag{A.12}$$

From the condition of invariance of the modulus of the energy-momentum four vector it follows that

$$(W_{total}^{cm})^2 = (W_{total}^{lab})^2 - (p_{total}^{lab})^2 \tag{A.13}$$

since $\vec{p}_{total}^{cm}$ is zero by definition. Using these relationships and the expressions for the momenta it can be shown that the energy of the gamma ray in the centre-of-mass system E_γ^{cm} is given by

$$E_\gamma^{cm} = \frac{(m+m)^2 + 2mT_n - m_d^2}{2\sqrt{(W_{total}^{lab})^2 - (p_n^{lab})^2}} \tag{A.14}$$

The photon energy in the centre-of-mass calculated for 63.4 MeV neutrons as provided in the experiments reported in this work is calculated to be

$$E_\gamma^{cm} = 33.4\ MeV$$

A.6 The energy of the photon in the inverse photodisintegration process

In order to compare results with theory the measurements are transformed to values for the inverse photodisintegration reaction viz., $d + \gamma \rightarrow n + p$. The value of the photon energy in a photodisintegration experiment is usually quoted as an energy in the laboratory frame E_γ^{lab} rather than in the centre-of-mass E_γ^{cm}. The relationship between E_γ^{cm} and E_γ^{lab} is given by

$$E_\gamma^{cm} = \frac{m_d E_\gamma^{lab}}{\sqrt{2E_\gamma^{lab} m_d + m_d^2}} \tag{A.15}$$

A direct relationship between the laboratory neutron kinetic energy $T_n^{lab}$and $E_\gamma^{lab}$is given by [Ar91].

$$E_\gamma^{lab} = \frac{m_p}{m_d} T_n^{lab} + \frac{1}{2m_d}((m_n + m_p)^2 - m_d^2) \tag{A.16}$$

From either of the last two equations it can be shown that for 63.4 MeV neutrons, the incident neutron energy in the present n- p capture experiment, the equivalent laboratory photon energy for photodisintegration $E_\gamma^{lab} \equiv E_\gamma$ is 33.9 MeV.

c:/thesis/new;thesis

Bibliography

[Ad78] J.M. Adams and G. White, Nucl. Instr. Meth. **156** (1978) 459

[Ah74] J. Ahrens, H.B. Eppler, H. Gimm, M. Kröning, P. Riehn, H. Wäffler, A. Zeiger and B. Ziegler, Phys. Lett. B **52** (1974) 49

[Aj84] F. Ajzenberg-Selove, Nucl. Phys. A **413** (1984) 1

[Aj88] F. Ajzenberg-Selove, Nucl. Phys. A **490** (1988) 1

[Al58] I.U. Aleksandrov, N.B. Delone, L.I. Slovokhotov, G.A Sokol and L.N. Shtarkov, Sov. Phys. JETP **6** (1958) 472

[Al55] L.J. Allen, Phys. Rev. **98** (1955) 705

[Al93] M.S. Allie, F.D. Brooks, D.G. Aschman, A. Buffler, W.A. Cilliers, R.W. Fearick, C.G.L. Henderson, M.J. Oliver, M.R. Nchodu, S.M. Perez, D. Steyn, W.R. McMurray, B.R.S. Simpson, F.D.S. Smit, H.G. Miller, K. Bharuth-Ram and I.J. van Heerden, Phys. Lett. B **314** (1993) 173

[Am36] E. Amaldi and E. Fermi, Phys. Rev. **50** (1936) 899

[Ar93] H. Arenhövel (1993): Private Communication.

[Ar91] H. Arenhövel and M. Sanzone, Photodisintegration of the Deuteron: A Review of Theory and Experiment (Springer-Verlag, 1991)

[Ba61] A.M. Baldin, V.I. Gol'Danskii and I.L. Rozenthal, Kinematics of Nuclear Reactions (Pergamon Press, 1961)

[Be72] M.J. Berger and S.M. Seltzer, Nucl. Instr. Meth. **104** (1972) 317

[Be90] J.R. Bergervoet, P.C. van Campen, R.A.M. Klomp, J.-L. de Kok, T.A. Rijken, V.G.J. Stoks and J.J. de Swart, Phys. Rev. C **41** (1990) 1435

[Be86] R. Bernabei, A. Incicchitti, M. Mattioli, P. Picozza, D. Prosperi, L. Casano, S. d'Angelo, M.P. De Pascale, C. Schaerf, G. Giordano, G. Matone, S. Frullani and B. Girolami, Phys. Rev. Lett. **57** (1986) 1542

[Be35] A. Bethe and R.E. Peierls, Proc. Royal Soc. **A148** (1935) 146

[Be56] H.A. Bethe and P. Morrison, Elementary Nuclear Theory, 2nd ed. (Wiley, 1956)

[Be69] P.R. Bevington, Data reduction and error analysis for the physical sciences (McGraw-Hill, 1969)

[Bi88] Y. Birenbaum, Z. Berant, A. Wolf, S. Kahane and R. Moreh, Phys. Rev. Lett. **61** (1988) 810

[Bi85] Y. Birenbaum, S. Kahane and R. Moreh, Phys. Rev. C **32** (1985) 1825

[Bo79] M. Bosman, A. Bol, J.F. Gilot, P. Leleux, P. Lipnik and P. Macq, Phys. Lett. B **82** (1979) 212

[Br79] F.D. Brooks, Nucl. Instr. Meth. **162** (1979) 477

[Bu95] A.J. Buchmann, Prog. Part. Nucl. Phys. **34** (1995) 159

[Bu90] A. Buffler, M.Sc Thesis, University of Cape Town 1990 (unpublished)

[Bu68] J. Buon, V. Gracco, J. Lefrancois, P. Lehmann, B. Merkel and P. Roy, Phys. Lett. B **26** (1968) 595

[Ca82b] A. Cambi, B. Mosconi and P. Ricci, Phys. Rev. C **26** (1982) 2358

[Ca82a] A. Cambi, B. Mosconi and P. Ricci, Phys. Rev. Lett. **48** (1982) 462

[Ca87] J.M. Cameron, S. Afr. J. Phys. **10** (1987) 94

[Ca86] J.M. Cameron, C.A. Davis, H. Fielding, P. Kitching, J. Pasos, J. Soukop, J. Uegaki, J. Wesick, H.S. Wilson, R. Abegg, D.A. Hutcheon, C.A. Miller, A.W. Stetz and I.J. van Heerden, Nucl. Phys. A **458** (1986) 637

[Ch34] J. Chadwick and M. Goldhaber, Nature **134** (1934) 237

[Co81] P. Corvisiero, M. Taiuti, A. Zucchiati and M. Anghinolfi, Nucl. Instr. Meth. **185** (1981) 291

[Co73] W.N. Cottingham, M. Lacombe, B. Loiseau, J.M. Richard and R. Vinh Mau, Phys. Rev. D **8** (1973) 800

[Da70] E.A Dams and R. Adams, Applied Gamma Ray Spectroscopy (Pergamon, 1970)

[De92] P.T. Debevec, P.D. Harty, J.E. Knott, D.A. Jenkins and R.T. Jones, Phys. Rev. C **45** (1992) 904

[De91a] A. De Graeve, A. Zieger, R. Van De Vyver, C. Van Den Abeele, H. Ferdinande, L. Van Hoorebeke, D. Ryckbosch, F. De Smet and B. Ziegler, Nucl. Phys. A **530** (1991) 420

[De91b] A. De Graeve, A. Zieger, R. Van de Vyver, C. Van den Abeele, H. Ferdinande, L. Van Hoorebeke, R. Ryckbosch, F. De Smet and B. Ziegler, Few Body Sys. **10** (1991) 37

[De85] M.P. De Pascale, G. Giordano, G. Matone, D. Babusci, R.C. Bernabei L, O.M. Bilaniuk, S. d'Angelo, M. Mattioli, P. Picozza, D. Prosperi, C. Schaerf, S. Frullani and B. Girolami, Phys. Rev. C **32** (1985) 1830

[De82] M.P. De Pascale, G. Giordano, G. Matone, P. Piccoza, L. Azario, R. Caloi, L. Casano, L. Ingrosso, M. Mattioli, E. Poldi, D. Prosperi and S. Schaerf, Phys. Lett. B **119** (1982) 30

[De90] D. De Sanctis, A.B. Kaidalov and L.A. Kondratyuk, Phys. Rev. C **42** (1990) 1764

[De86] E. De Sanctis, M. Anghinolfi, G.P. Capitani, P. Corvisiero, P. Di Giacomo, C. Guaraldo, V. Lucherini, E. Polli, A.R. Reolon, G. Ricco, M. Sanzone and A. Zucchiatti, Phys. Rev. C **54** (1986) 413

[De58] J.J. de Swart and R.E. Marshak, Phys. Rev. **111** (1958) 272

[De59a] J.J. de Swart, Physica (1959) 233

[De59b] J.J. de Swart and R.E. Marshak, Physica (1959) 1001

[Du85] C. Dupont, P. Leleux, P. Lipnik, P. Macq and A. Ninane, Nucl. Phys. A **445** (1985) 13

[Ei76] J.M. Eisenberg and W. Greiner, Excitation mechanisms of the nucleus, 2nd ed. (North-Holland, 1976)

[Fe35] E. Fermi, Phys. Rev. Lett. **48** (1935) 570

[Fi91] G. Fink, P. Doll, S. Hauber, M. Haupenthal, H.O. Klages, H. Schieler, F. Smend and G.D. Wicke, Nucl. Phys. A **530** (1991) 331

[Fi79] F.W.K. Firk, In: Neutron Capture Gamma-Ray Spectroscopy, eds: R.E. Chrien and W.R. Kane (Plenum, 1979) 245-263.

[Fr84] J.L. Friar, B.F. Gibson and G.L. Payne, Phys. Rev. C **30** (1984) 441

[Fr89] B. Frois and J.F. Mathiot, Comm. Nucl. Part. Phys. **XVIII** (1989) 307

[Ga60] J.A. Galey, Phys. Rev. **117** (1960) 763

[Gi81] J.F. Gilot, A. Bol, P. Leleux, P. Lipnik and P. Macq, Phys. Rev. Lett. **47** (1981) 304

[Gr76] B. Grosswendt and E. Waibel, Nucl. Instr. Meth. **133** (1976) 25

[Ha73] Hadjimichael, Phys. Lett. B **46** (1973) 147

[Ha87] E. Hadjimichael, M.L. Rustgi and L.N. Pandey, Phys. Rev. C **36** (1987) 44

[Ha53] J. Halpern and E.V. Weinstock, Phys. Rev. **91** (1953) 934

[Ha62] T. Hamada and I.D. Johnston, Nucl. Phys. A **34** (1962) 382

[He79] R.L. Heath, R. Hofstadter and E.B. Hughes, Nucl. Instr. Meth. **162** (1979) 431

[He91] C.G.L. Henderson, M.Sc Thesis, University of Cape Town 1991 (unpublished)

[Ho81] K. Holinde, Phys. Lett. **68** (1981) 121

[Hu76] R.J. Hughes, A. Zieger, H. Wäffler and B. Ziegler, Nucl. Phys. A **276** (1976) 329

[Hw84] W.-Y.P. Hwang, Can. J. Phys. **62** (1984) 1072

[Ja62] L. Jarczyk, H. Knoepfel, J. Lang, R. Müller and W. Wölfli, Nucl. Instr. Meth. **17** (1962) 310

[Ja93a] W. Jaus, D. Bofinger and W.S. Woolcock, Nucl. Phys. A **562** (1993) 477

[Ja93b] W. Jaus, D. Bofinger and W.S. Woolcock, Nucl. Phys. A **562** (1993) 500

[Ja84] W. Jaus and W.S. Woolcock, Nucl. Phys. A **431** (1984) 669

[Ja87a] W. Jaus and W.S. Woolcock, Nucl. Phys. A **473** (1987) 667

[Ja87b] W. Jaus and W.S. Woolcock, Nucl. Phys. A **473** (1987) 685

[Je94] D.A. Jenkins, P.T. Debevec and P.D. Harty, Phys. Rev. C **50** (1994) 74

[Ka89] A. Kassaee, L.N. Pandey and M.L. Rustgi, Phys. Rev. C **39** (1989) 1147

[Kn89] G.F. Knoll, Radiation Detection and Measurement, 2nd ed.(Wiley, 1989)

[Ko67] R. Kose, W. Paul, K. Stockhurst and K.H. Kissler, Z. Phys. **202** (1967) 364

[Kr92] K.-H. Krause, J. Sobolewski, J. Ahrens, J.M. Henneberg and B. Ziegler, Nucl. Phys. A **532** (1992) 617

[La80] M. Lacombe, B. Loiseau, J.M. Richard, R. Vinh Mau, J. Cote, P. Pires and R. de Tourreil, Phys. Rev. C **21** (1980) 861

[La90] R.H. Landau, Quantum Mechanics II, (Wiley, 1990)

[La84] J.M. Laget, Can. J. Phys. **62** (1984) 1046

[Le87] W.R. Leo, Techniques for Nuclear and Particle Physics Experiments. (Springer-Verlag, 1987)

[Le89] P. Levi Sandri, M. Anghinolfi, N. Bianchi, G.P. Capitani, P. Corvisiero, E. De Sanctis, C. Guaraldo, V. Lucherini, V. Muccifora, E. Polli, A.R. Reolon, G. Ricco, P. Rossi, M. Sanzone and M. Taiuti, Phys. Rev. C **39** (1989) 1701

[Ma87] R. Machleidt, K. Holinde and C. Elster, Phys. Rep. **149** (1987) 1

[Ma69] P. Marmier and E. Sheldon, Physics of Nuclei and Particles (Academic Press, 1969)

[Ma88] J.F. Mathiot, J. Phys. G **14 Suppl.** (1988) S357

[Me61] E. Merzbacher, Quantum Mechanics. (Wiley, 1961)

[Me85] H.O. Meyer, J.R. Hall, M. Hugi, H.J. Karwowski, R.E. Pollock and P. Schwandt, Phys. Rev. C **31** (1985) 309

[Me67] W.E. Meyerhof, Elements of nuclear physics. (McGraw Hill, 1967)

[Mi67] A. Michalowicz, Kinematics of Nuclear Reactions. (Lliffe Books, 1967)

[Mi89] P. Michel, K. Moeller, J. Moesner and G. Schmidt, J. Phys. G **15** (1989) 1025

[Mi73] H.G. Miller and H. Arenhövel, Phys. Rev. C **7** (1973) 1003

[Mo89] R. Moreh, T.J. Kennett and W.V. Prestwich, Phys. Rev. C **39** (1989) 1247

[Mu79] J.W. Müller, Nucl. Instr. Meth. **163** (1979) 241

[Mu84] J.W. Müller, Natl. Bur. Stand. **617** (1984) 375

[Na78] M.M. Nagels, T.A. Rijken and J.J. de Swart, Phys. Rev. C **17** (1978) 768

[Nc94] M.R. Nchodu, M.Sc Thesis, University of Cape Town 1994 (unpublished)

[Ni87] A. Ninane, C. Dupont, P. Leleux, P. Lipnik and P. Macq, Phys. Rev. C **35** (1987) 402

[Pa64] F. Partovi, Ann. Phys. **27** (1964) 79

[Pa87] F. Partovi, Phys. Rev. C **36** (1987) 491

[Po95] B. Povh, K.Rith, C. Scholz and F. Ztesche, Particles and nuclei (Springer, 1995)

[Ra90] J. Rapaport, C.C. Foster, C.D. Goodman, C.A. Goulding, T.N. Taddeucci, D.J. Horen, E.R. Sugarbaker, C. Gaarde, J. Larsen, J.A. Carr, F. Petrovich and M.J. Threapleton, Phys. Rev. C **51** (1990) 1920

[Ri72] D.O. Riska and G.E. Brown, Phys. Lett. B **38** (1972) 193

[Ro89] P. Rossi, E. De Sanctis, P. Levi Sandri, N. Bianchi, C. Guaraldo, V. Lucherini, V. Muccifora, E. Polli, A.R. Reolon and G.M. Urciuoli, Phys. Rev. C **40** (1989) 2412

[Ru60] M.L. Rustgi, W. Zernkik, G. Breit and D.J. Andrews, Phys. Rev. C **120** (1960) 1881

[Sa93] S.M. Sadeghi, S.S.M. Wong and S. Bayegan, Nucl. Phys. A **554** (1993) 620

[Sc89] K.-M. Schmitt and H. Arenhövel, Few Body Sys. **7** (1989) 95

[Sc91] K.-M. Schmitt, P. Wilhelm and H. Arenhövel, Few Body Sys. **10** (1991) 105

[Sc90] K.-M. Schmitt, P. Wilhelm, H. Arenhövel, A. Cambi, B. Mosconi and P. Ricci, Phys. Rev. C **41** (1990) 841

[Sh70] Y.M. Shin, J.A. Rawlins, W. Buss and A.O. Evwaraye, Nucl. Phys. A **154** (1970) 482

[Si37] A.J.F. Siegert, Phys. Rev. **52** (1937) 787

[Sk74] D.M. Skopik, Y.M. Shin, M.C. Phenneger and J.J. Murphy, Phys. Rev. C **9** (1974) 531

[Sm86] F.D. Smit, Ph.D. Thesis, University of Cape Town 1986 (unpublished)

[Sm87] F.D. Smit and F.D. Brooks, Nucl. Phys. A **465** (1987) 429

[Sq52] G.L. Squires, In: Progress In Nuclear Physics, Vol. 2, ed: O.R. Frisch (Pergamon 1952) 89-119.

[St87] K.E. Stephenson, R.J. Holt, R.D. McKeown and J.R. Specht, Phys. Rev. C **35** (1987) 2023

[St85] T. Stiehler, B. Kühn, K. Müller, J. Mösner, W. Neubert, W. Pilz and G. Schmidt, Phys. Lett. B **151** (1985) 185

[St93] V. Stoks and J.J. de Swart, Phys. Rev. C **47** (1993) 761

[St94] V. Stoks, R.A.M. Klomp, C.P.F. Terheggen and J.J. de Swart, Phys. Rev. C **49** (1994) 2950

[Ta83] M. Taiuti, M. Anghinolfi, P. Corvisiero, G. Ricco and A. Zucchiatti, Nucl. Instr. Meth. **211** (1983)

[Th86] A.E. Thorlacius and H.W. Fearing, Phys. Rev. C **33** (1986) 1830

[Ur32] H.C. Urey, F.G. Brickweddle and G.M. Murphy, Phys. Rev. **40** (1932) 1

[Vi47] F. Villars, Helv. Phys. Acta **20** (1947) 476

[Vi91] R. Vinh Mau, C. Semay, B. Loiseau and M. Lacombe, Phys. Rev. C **67** (1991) 1392

[Wa90] P. Wauters, C. Dupont, P. Leleux, P. Lipnik, P. Macq, A. Ninane and S.W. Kitwanga, Few Body Sys. **8** (1990) 1

[We71] B. Weissman and H.L. Schultz, Nucl. Phys. A **174** (1971) 129

[Wh56] E.A. Whalin, B.D. Schriever and A.O. Hanson, Phys. Rev. **101** (1956) 377

[Wi88] P. Wilhelm, W. Leidemann and H. Arenhövel, Few Body Sys. **3** (1988) 111

[Wo90] S.M. Wong, Introductory nuclear physics. (Prentice-Hall, 1990)

[Wo96] W.S. Woolcock (1996): Private Communication.

[Yi88] S. Ying, E.M. Henley and A.G. Miller, Phys. Rev. C **38** (1988) 1584

[Zi92b] A. Zieger, A. De Graeve, D. Christmann, R. Van de Vyver, C. Van den Abeele and B. Ziegler, Phys. Lett. B **287** (1992) 51

[Zi92a] A. Zieger, A. De Graeve, D. Christmann, R. Van de Vyver and B. Ziegler, Phys. Lett. B **285** (1992) 1

[Zi86] A. Zieger, P. Grewer and B. Ziegler, Few Body Sys. **1** (1986) 135

[Zu88] A. Zucchiatti, Ph.D. Thesis, University of the Witwatersrand 1988 (unpublished)